

# The *Spitzer* Local Volume Legacy Survey: Infrared Imaging and Photometry for 258 Nearby Galaxies

D.A. Dale<sup>1</sup>, S.A. Cohen<sup>1</sup>, L.C. Johnson<sup>1</sup>, M.D. Schuster<sup>1</sup>, M. Block<sup>2</sup>, C.W. Engelbracht<sup>2</sup>,  
A. Begum<sup>3</sup>, D. Calzetti<sup>4</sup>, J.J. Dalcanton<sup>5</sup>, J.G. Funes<sup>6</sup>, A. Gil de Paz<sup>7</sup>, K.D. Gordon<sup>8</sup>,  
B.D. Johnson<sup>9</sup>, R.C. Kennicutt<sup>3,2</sup>, J.C. Lee<sup>10</sup>, S. Sakai<sup>11</sup>, E.D. Skillman<sup>12</sup>, L. van Zee<sup>13</sup>,  
F. Walter<sup>14</sup>, D.R. Weisz<sup>12</sup>, B. Williams<sup>5</sup>, S.-Y. Wu<sup>4</sup>, Y. Wu<sup>15</sup>

## ABSTRACT

Near-, mid-, and far-infrared flux properties are presented for the Local Volume Legacy survey, a *Spitzer Space Telescope* legacy program built upon a foundation of *GALEX* ultraviolet and ground-based H $\alpha$  imaging of 258 galaxies within 11 Mpc. The Local Volume Legacy survey covers an unbiased, representative, and statistically robust sample of nearby star-forming galaxies, exploiting the highest extragalactic spatial resolution achievable with *Spitzer*. As a result of its approximately volume-limited nature, LVL augments previous *Spitzer* observations of present-day galaxies (such as from SINGS, the *Spitzer* Infrared Nearby Galaxies Survey) with improved sampling of the low-luminosity dwarf galaxy population. The collection of LVL galaxies shows a large spread in mid-infrared colors, likely due to the conspicuous deficiency of PAH emission from low-metallicity galaxies. Conversely, the far-infrared tightly tracks the total infrared, with a dispersion in their flux ratio of order 0.1 dex. In terms of the relation

---

<sup>1</sup>Department of Physics and Astronomy, University of Wyoming, Laramie, WY 82071; ddale@uwyo.edu

<sup>2</sup>Steward Observatory, University of Arizona, Tucson, AZ 85721

<sup>3</sup>Institute of Astronomy, University of Cambridge, Cambridge CB3 0HA, United Kingdom

<sup>4</sup>Astronomy Department, University of Massachusetts, Amherst, MA 01003

<sup>5</sup>Department of Astronomy, University of Washington, Seattle, WA 98195

<sup>6</sup>Vatican Observatory Research Group, Steward Observatory, University of Arizona, Tucson, AZ 85721

<sup>7</sup>Departamento de Astrofísica, Universidad Complutense, Madrid, E-28040, Spain

<sup>8</sup>Space Telescope Science Institute, 3700 San Martin Drive, Baltimore, MD 21218

<sup>9</sup>Department of Astronomy, Columbia University, New York, NY 10027

<sup>10</sup>Carnegie Observatories, 813 Santa Barbara Street, Pasadena, CA 91101

<sup>11</sup>Division of Astronomy and Astrophysics, University of California, Los Angeles, CA 90095

<sup>12</sup>Astronomy Department, University of Minnesota, Minneapolis, MN 55455

<sup>13</sup>Department of Astronomy, Indiana University, Bloomington, IN 47405

<sup>14</sup>Max Planck Institut für Astronomie, Königstuhl 17, 69117 Heidelberg, Germany

<sup>15</sup>Astronomy Department, Cornell University, Ithaca, NY 14853

between infrared-to-ultraviolet ratio and ultraviolet spectral slope, the LVL sample is shifted to redder colors than the standard correlation for starburst galaxies. Theoretical models suggest that the amplitude of deviations from the starburst relation corresponds to the age of the stellar populations that dominate the ultraviolet/optical luminosities.

*Subject headings:* surveys — galaxies: photometry — infrared: galaxies

## 1. Introduction

The goal of the *Spitzer* Local Volume Legacy (LVL) survey<sup>1</sup> is to fill a vital niche in existing multi-wavelength surveys of present-day galaxies with a statistically robust, approximately volume-complete study of our nearest star-forming neighbors. Although star formation rates based on *GALEX*, *Spitzer*, and ground-based data are being collected for thousands of galaxies (and hundreds of thousands via the Sloan Digital Sky Survey), most of these datasets are derived from flux-limited samples, and thus suffer from the well-known biases against low-mass, low surface brightness systems. Multi-wavelength datasets that include such systems (e.g., SINGS (Kennicutt et al. 2003) and LITTLE THINGS (Hunter et al. 2009)) only provide representative samplings of the overall galaxy population, and are thus not suitable for studies that demand datasets which are true to the statistics rendered by volume-limited sampling.

We have chosen to directly address this problem by completing *Spitzer* infrared imaging for a tiered sample of 258 galaxies which consolidates the strengths of two existing volume-limited surveys. ANGST, the ACS Nearby Galaxies Survey Treasury (Dalcanton et al. 2009), includes all 69 known galaxies outside the Local Group within 3.5 Mpc and with  $|b| > 20^\circ$ , plus an extension to the M 81 group. ANGST augments existing deep HST imaging with new observations to provide complete stellar photometry with homogeneous depth. 11HUGS, the 11 Mpc H $\alpha$  and Ultraviolet Galaxy Survey, provides *GALEX* ultraviolet (Lee et al. 2009) and ground-based H $\alpha$  imaging (Kennicutt et al. 2008) of all known star-forming galaxies within 11 Mpc,  $m_B < 15.5$  mag and  $|b| > 30^\circ$ . These limits were selected to include a large enough volume to probe a diverse cross-section of morphologies and star formation properties (e.g., Lee et al. 2007), but still ensure completeness in the parent galaxy catalogs from which the sample was drawn. Statistical tests and comparison with blind all-sky H I surveys show that the catalog completeness is excellent ( $>95\%$ ) within these limits (Lee et al. 2009). The conjoined surveys are highly complementary. ANGST provides complete coverage within its volume, including all galaxy morphologies and the lowest mass galaxies. Conversely, 11HUGS covers a 30 times larger volume, and therefore offers a broader coverage of the star-forming galaxy population as a whole, including a 10 magnitude range in optical luminosity, a  $10^5$  range in star formation rates, and a 2 dex span in metallicity.

Thus, LVL provides the most complete census to date of dust and recent star formation in

---

<sup>1</sup><http://www.ast.cam.ac.uk/IoA/research/lvls>

the Local Volume. The data include (i)  $H\alpha$  emission, which traces massive O star formation, (ii) ultraviolet emission, which traces O as well as longer-lived B stars, and (iii) infrared emission, which constrains how much of the energy produced by stars is absorbed and re-radiated by dust. This redundancy of star formation rate tracers provides not only robust, extinction-corrected star formation rates for an approximately volume-limited sample, it also constrains the temporal behavior of bursty star formation since the ultraviolet and  $H\alpha$  emission probe activity over timescales (of  $\sim 100$  Myr and  $< 5 - 10$  Myr, respectively) which flank the expected duration of starburst episodes. Crucial constraints on the old stellar population content of the galaxies can also be provided by mid-infrared luminosities. Public data releases of our multi-wavelength imaging have begun through the NASA/IPAC Infrared Science Archive<sup>2</sup> (IRSA), with expected completion of data product deliveries by the end of 2009.

Principal science issues to be addressed by the LVL team include: constraining the physical mechanisms underlying dust heating and understanding correlations between infrared emission, dust content and global galaxy properties; establishing the primary factors which influence polycyclic aromatic hydrocarbon (PAH) emission and evaluating the robustness of PAH emission as a star formation rate indicator, particularly at low metallicities and high specific star formation rates; and probing the temporal variation of star formation as a function of global properties, with special focus on the dwarf galaxy population that dominates the sample. In this paper, we present 2MASS near-infrared and *Spitzer* mid- and far-infrared flux densities for the LVL sample, which will form the basis for many of the analyses presented in subsequent papers. Section 2 describes the sample, Section 3 reviews the observational and data processing programs, Section 4 covers details of the integrated aperture photometry, Section 5 presents initial results based on the photometry, and Section 6 summarizes our work.

## 2. The Sample

As described above, the Local Volume Legacy sample is a compilation of 258 galaxies, which includes (i) galaxies from the ANGST program—69 known galaxies outside the Local Group with  $D < 3.5$  Mpc and  $|b| > 20^\circ$ , plus an extension to the M 81 group, and (ii) galaxies in the 11HUGS sample—an unbiased set of  $m_B < 15.5$  mag S-Irr galaxies from the larger, and more representative, 11 Mpc volume which is visible above the Galactic Plane ( $|b| > 30^\circ$ ). These limits define the ranges over which the parent samples are known to be relatively complete, and the selection of galaxies leverages LVL’s new *Spitzer* observations on already-available multi-wavelength imaging. For details on the sample selection and properties of the precursor 11HUGS and ANGST surveys, the reader is referred to Kennicutt et al. (2008) and Dalcanton et al. (2009). A schematic illustration of LVL’s tiered volume coverage is shown in Figure 1.

---

<sup>2</sup><http://ssc.spitzer.caltech.edu/legacy/lvlhistory.html>

General properties of the LVL sample, taken primarily from Kennicutt et al. (2008) and references therein, are given in Table 1 and displayed in Figure 2. Approximately half (53%) of the LVL galaxies have spiral morphology, 38% are irregulars, 8% are S0 galaxies, and there is a single elliptical. For comparison, SINGS has larger fractions of non-spiral morphologies, with 63% spiral, 17% irregular, 12% S0, and 8% elliptical morphologies. While the 11HUGS-based portion of the sample goes as faint as  $m_B = 15.5$  mag, as explained above, Figure 2 shows that the faintest systems in the ANGST inner-tier approach  $m_B = 19$  mag (e.g., M 81 Dwarf A and BK3N).

The distances in the LVL sample range from 50-60 kpc for the Magellanic Clouds out to 11 Mpc at the outer edge of the survey. Kennicutt et al. (2008) describe in detail the origins of the adopted distances displayed in Figure 2. There exist direct stellar-based distance determinations for many of the closer galaxies in the LVL sample, whereas secondary distance indicators are frequently used for the more distant systems. The main distance indicators used are *tip of the red giant branch* (for 40% of the sample) and *flow-corrected Hubble distances* (35%). Lesser-used techniques include the utilization of *brightest blue stars* (13%), *cepheid variables* (6%), and *surface brightness fluctuations* (3%). Since the origination of this project, four LVL galaxies have new distances which place them outside of 11 Mpc: UGC 00521, UGC 06782, IC 2049, and UGC 7321. Though the observations for these four systems are presented here, these galaxies will not be included in future, LVL sample-wide studies. This is an inherent difficulty with efforts to construct a volume-limited sample. The membership of the sample will be necessarily fluid until accurate distance and photometric measurements are available for all of the galaxies that are within the volume and around its periphery.

Figure 3 shows how LVL samples the integrated infrared and infrared-to-optical galaxy properties. Also displayed in Figure 3 are the distributions for SINGS, a survey designed to broadly, but not statistically, sample the range of galaxy properties in the local universe. While the SINGS survey is slightly biased to cooler far-infrared colors and larger infrared-to-optical ratios, the two surveys dramatically differ in their distributions of total infrared luminosity (defined in § 5.3). LVL is far more effective at filling in at faint infrared luminosities, whereas SINGS focuses more on the infrared-bright and dusty systems in the local universe.

### 3. Observational Strategy and Data Processing

#### 3.1. New *Spitzer* IRAC 3.6, 4.5, 5.8, and 8.0 $\mu\text{m}$ Data

New *Spitzer* IRAC (Fazio et al. 2004) observations were obtained for 180 LVL galaxies. The IRAC observing strategy follows that of SINGS, which shows that stellar and small grain dust emission is typically detected out to the optical radius at a surface brightness level of  $\sim 0.01$ – $0.1$  MJy sr $^{-1}$  (Regan et al. 2006; Dale et al 2000). For galaxies smaller than the IRAC field of view ( $D_{25} \leq 300''$ ) the Astronomical Observing Requests (AORs) were constructed using four dithered 30 s integrations. For larger galaxies a mosaicking strategy with  $\sim$ half-array spatial offsets was

used, with the sizes of the mosaic ‘cores’ tailored to the optical size of each galaxy. Two sets of IRAC maps were obtained for each source to enable asteroid removal and to enhance map sensitivity and redundancy. Combining all eight 30 s frames thus results in a net integration per pixel of 240 s (and 120 s around the  $\sim 2'.5$ -wide mosaic peripheries). Since each source was observed in all IRAC channels, ample sky coverage is automatically provided by the non-overlapping nature of the two IRAC imagers.

The BCD data used for post-pipeline processing are from the S18 pipeline version (*should be true by submission time!*). The multi-epoch, multiple-pointing IRAC observations for each galaxy are combined into one single mosaic for each band using the MOPEX mosaicking software. Additional post-BCD processing includes: distortion corrections, rotation of the individual frames (for multi-epoch observations), bias structure and bias drift corrections, image offset determinations via pointing refinements from the SSC pipeline (MOPEX’s default), detector artifact removal, constant-level background subtraction, and image resampling to  $0''.75$  pixels using drizzling techniques. The drizzling slightly improves the final PSF over the native one; the full-width half maxima are  $\sim 1''.6$  in the shorter wavelength channels and  $\sim 1''.9$  at  $8\ \mu\text{m}$ . The final images are in units of  $\text{MJy sr}^{-1}$  and have the average sky level removed; sky values are estimated via several “blank” regions located near but beyond the target galaxy emission.

In cases where exceptionally bright target sources saturated or entered the non-linear regime of the detector during the 30 second exposure, additional 1.2 s images are used to allow for recovery of this data. Pixels affected by these issues, typically in the  $5.8$  and  $8.0\ \mu\text{m}$  frames, are flagged by MOPEX during processing. Correction begins by creating a mosaic of the 1.2 s exposures interpolated onto the same pixel grid as the original mosaic. A difference image is then created from the two mosaics and any residual, systematic difference in the background sky levels is removed. Pixels in the difference image valued at  $1\ \text{MJy sr}^{-1}$  or higher are flagged (routinely regions of  $\sim 400$  contiguous pixels) and these pixels in the long integration mosaic are replaced by their short integration counterparts. The nuclear regions for the following galaxies were affected by saturation: NGC 0253, NGC 2903, NGC 3031, NGC 3034 (at all IRAC wavelengths), NGC 3351, NGC 3593, NGC 3627, NGC 4258, NGC 5195, and NGC 5253.

### 3.2. New *Spitzer* MIPS 24, 70, and $160\ \mu\text{m}$ Data

New *Spitzer* MIPS (Rieke et al. 2004) observations were obtained for 201 LVL galaxies. Galaxies were imaged in all three MIPS bands centered at 24, 70, and  $160\ \mu\text{m}$ , using the highly successful scan mapping strategy employed in the SINGS project. The scan mode was used even on galaxies small enough to fit within the array field of view, because achieving adequate background measurements for extended targets in photometry mode is less efficient than the scan mode. Each map was executed at the medium scan rate, and includes multiple scan legs tailored to the size of the galaxy and half-array offsets between scan legs. Each galaxy was mapped twice, with the maps separated by 10-40 days to allow time for the field-of-view to rotate and for asteroids to move out of the field.

This second map was performed in the reverse direction (the “backward mapping” mode), with offsets in the cross-scan and in-scan directions. Taken together, these mapping strategies ensure that each point on the galaxy is scanned over in two different directions, which aids reduction of array artifacts on both Si:As and Ge:Ga arrays. The in-scan offset ensures that Ge:Ga stimflashes do not occur at the same point in both maps and thereby improves the calibration. The integration time per point is 160, 80, and 16 s at 24, 70, and 160  $\mu\text{m}$ , respectively.

The pixel scale of the MIPS mosaics is wavelength-dependent:  $1''.5$ ,  $4''.5$ , and  $9''.0$  at 24, 70, and 160  $\mu\text{m}$ , respectively. The MIPS images are processed with the MIPS Data Analysis Tool (DAT; Gordon et al. 2005), supplemented by custom scripts for the specific data reduction and mosaicking of extended sources. The latter include: at 24  $\mu\text{m}$ , readout offset correction, array-averaged background subtraction, and exclusion of the first five images in each scan leg due to boost frame transients. At 70 and 160  $\mu\text{m}$ , the custom scripts include a pixel-dependent background subtraction for each map to remove residual detector drifts and background cirrus and zodiacal emission. This method of reduction was used for all the SINGS galaxies as well as very large galaxies (M 31, M 33, M 101, SMC, LMC, etc.).

Finally, a correction for 70  $\mu\text{m}$  non-linearity effects is included in the data processing. A correction of the form

$$f_{\text{true}}^{70\mu\text{m}} = 0.502(f_{\text{measured}}^{70\mu\text{m}})^{1.182}, \quad (1)$$

derived from data presented by Gordon et al. (2008, in preparation), is applied to pixel values above a threshold of  $\sim 44 \text{ MJy sr}^{-1}$ . A small fraction of the pixels in a total of 40 LVL 70  $\mu\text{m}$  images require such a correction. The median correction to the global 70  $\mu\text{m}$  flux density for these 40 galaxies is only a few percent.

### 3.3. Archival *Spitzer* Data

Archival IRAC and MIPS data, with spatial coverage and sensitivity similar to or greater than that described in § 3.1 and § 3.2, are utilized for 78 (IRAC) and 57 (MIPS) galaxies. No new IRAC or MIPS observations were obtained for these subsets of the LVL sample. The data processing procedures for the archival data are the same as those followed for the new observations described above, except for the asteroid rejection in the few cases where only one epoch was measured. Table 2 indicates for which galaxies we utilize archival *Spitzer* data.

## 4. Aperture Photometry

Table 2 presents the global flux densities for the entire LVL sample, for wavelengths spanning the near- to far-infrared. The data are corrected for Galactic extinction (Schlegel, Finkbeiner, & Davis 1998) assuming  $A_V/E(B - V) \approx 3.1$  and the reddening curve of Li & Draine (2001). The

effect of airmass has been removed from the ground-based near-infrared fluxes. Below follows a description of the infrared data collected for the LVL program.

#### 4.1. 2MASS Near-Infrared JHK<sub>s</sub> Photometry

The Two Micron All Sky Survey (2MASS) obtained data for the entire sky at 1.25, 1.65, and 2.17  $\mu\text{m}$  using two automated, ground-based 1.3 m telescopes (Skrutskie et al. 2006). Galaxy photometry is available from the 2MASS Extended Source Catalog for over a million galaxies and from the 2MASS Large Galaxy Atlas for several hundred galaxies larger than 1' (Jarrett et al. 2003). Integrated fluxes for several LVL galaxies were adopted from the Large Galaxy Atlas, and these are generally consistent with expectations based on IRAC 3.6 and 4.5  $\mu\text{m}$  fluxes and simple stellar model extrapolations to 2MASS wavelengths. However, most LVL galaxies do not appear in the Large Galaxy Atlas, and for these systems many of the fluxes from the Extended Source Catalog are 0.5–2 mag low based on similar extrapolations from IRAC 3.5 and 4.5  $\mu\text{m}$  data. We find that when Extended Source Catalog fluxes appear unexpectedly faint, it is typically due to the comparatively small apertures used in the automated 2MASS extraction. Hence we have extracted 2MASS fluxes for the vast majority of the LVL sample using the same apertures and foreground star removals used to determine IRAC and MIPS fluxes, as discussed in the following section. Figure 4 displays the ratios of our near-infrared extractions with those provided in the 2MASS Extended Source Catalog. Included in the figure are results from Kirby et al. (2008) based on deep  $H$  band imaging of nearby galaxies with the 3.9 m Anglo-Australian Telescope; Kirby et al. (2008) likewise find that Extended Source Catalog extractions are 0.5–2 mag too faint.

#### 4.2. *Spitzer* 3.6, 4.5, 5.8, 8.0, 24, 70, and 160 $\mu\text{m}$ Photometry

##### 4.2.1. *Foreground Star and Background Galaxy Removal*

The presence of foreground stars and background galaxies can significantly affect the global infrared fluxes for some galaxies, particularly the fainter dwarfs and galaxies at low Galactic latitudes. Once identified, the foreground stars and background galaxies are removed through a simple interpolation of the local sky from the images using the IRAF task `IMEDIT`. Our procedure for identifying these sources relies on a multi-wavelength analysis (3.6, 8.0, 24  $\mu\text{m}$ , and  $H\alpha$ ), looking for objects  $H\alpha$ -rich or especially blue (foreground stars;  $f_\nu(3.6)/f_\nu(8.0) > 8$ ), or small red systems with galaxy-like morphologies. Archival *Hubble Space Telescope* imaging was also inspected for obvious background galaxy or foreground stellar identifications, when available. When uncertain about the identification of a particular source, we opted to err on the conservative side and allow such sources to remain in the global flux extraction. However, these sources of uncertain origin are typically very faint and negligibly impact global flux extractions. The median ratios of edited-to-unedited fluxes is [0.854,0.846,0.939,0.971,0.980,1.00,1.00] at [3.6,4.5,5.8,8.0,24,70,160]  $\mu\text{m}$ ; very

few significant corrections are made at 24, 70, and 160  $\mu\text{m}$ .

The uncertainties provided in Table 2 include both calibration and statistical uncertainties. Calibration uncertainties are 5-10% for IRAC 3.6 and 4.5  $\mu\text{m}$  data, and 10-15% for IRAC 5.8 and 8.0  $\mu\text{m}$  data; 10% IRAC calibration uncertainties are used in Table 2. MIPS calibration uncertainties are 4%, 7%, and 12% respectively at 24, 70, and 160  $\mu\text{m}$  (Engelbracht et al. 2007, Gordon et al. 2007, and Stansberry et al. 2007).

#### 4.2.2. Aperture Corrections

For a given galaxy, the same aperture was used for extracting all IRAC and MIPS fluxes. Elliptical apertures for IRAC and MIPS photometry were based on capturing all the galaxy emission visible for all IRAC and MIPS images. Typically this means that the 3.6  $\mu\text{m}$  image was used to create the aperture, since *Spitzer* is most sensitive at 3.6  $\mu\text{m}$  and that is the *Spitzer* wavelength at which stars are brightest.

Since the IRAC flux calibration is based on point source photometry for a 12'' radius aperture, the fluxes for all extended sources and aperture radii  $\neq 12''$  need to have an additional correction applied. These corrections account for the “extended” emission due to the wings of the PSF and also for the scattering of the diffuse emission across the IRAC focal plane. As described in Dale et al. (2007), the IRAC extended source correction has been derived for a variety of source morphologies and extents. For an effective aperture radius  $r = \sqrt{ab}$  in arcseconds derived from the semi-major  $a$  and semi-minor  $b$  ellipse axes provided in Table 2, the IRAC extended source aperture correction is

$$f_{\text{true}}^{\text{IRAC}} / f_{\text{measured}}^{\text{IRAC}} = Ae^{-r^B} + C, \quad (2)$$

where  $A$ ,  $B$ , and  $C$  are listed in Table 3<sup>3</sup>. The median IRAC extended source aperture corrections are [0.914, 0.941, 0.826, 0.756] at [3.6, 4.5, 5.8, 8.0]  $\mu\text{m}$ .

Somewhat different from the situation for IRAC imaging, the main reason MIPS aperture corrections are needed is due to the smearing of light outside the aperture. MIPS aperture corrections are empirically determined from a comparison of fluxes from smoothed and unsmoothed 3.6  $\mu\text{m}$  imaging, an approximate proxy for tracing the MIPS galaxy morphologies. The aperture correction for a given MIPS flux is the ratio of the fluxes from the unsmoothed 3.6  $\mu\text{m}$  image to the flux from the 3.6  $\mu\text{m}$  image smoothed to the same PSF as the MIPS image in question. The median MIPS aperture corrections are [1.01, 1.01, 1.03] at [24, 70, 160]  $\mu\text{m}$ , and the most significant corrections are [1.09, 1.12, 1.42] for CGCG 269-049.

---

<sup>3</sup>See <http://ssc.spitzer.caltech.edu/irac/calib/extcal/>



### 4.3. Upper Limits

Many of the optically-faint galaxies in the sample are frequently undetected in the infrared, particularly at wavelengths of  $5.8\ \mu\text{m}$  and longer. Upper limits are included in Table 2 for sources undetected by infrared imaging. The  $3\sigma$  upper limits for *Spitzer* imaging are derived according to

$$f_\nu(3\sigma \text{ upper limit}) = 3 \sigma_{\text{sky}} \Omega_{\text{pix}} \sqrt{N_{\text{pix}} + N_{\text{pix}}^2 / N_{\text{sky}}} \approx 3 \sigma_{\text{sky}} \Omega_{\text{pix}} \sqrt{2N_{\text{pix}}} \quad (3)$$

where  $\sigma_{\text{sky}}$  is the sky surface brightness fluctuation per pixel ( $\text{MJy sr}^{-1}$ ),  $\Omega_{\text{pix}}$  the solid angle subtended per pixel,  $N_{\text{pix}}$  the number of pixels in the galaxy aperture, and  $N_{\text{sky}}$  the number of pixels in the sky aperture. The parameter  $\sigma_{\text{sky}}$  is approximately 0.02, 0.03, 0.11, 0.12, 0.2, 0.9,  $1.7\ \text{MJy sr}^{-1}$  at 3.6, 4.5, 5.8, 8.0, 24, 70, and  $160\ \mu\text{m}$ , respectively (Lee et al. 2009). A similar computation for 2MASS near-infrared upper limits is carried out after converting that survey’s mean  $10\sigma$  point source sensitivities ( $\sim 16.4$ ,  $15.5$ , and  $14.8$  mag for  $J$ ,  $H$ , and  $K_s$ , respectively; Skrutskie et al. 2006) to  $3\sigma$  values and accounting for the difference in the  $4''$  radius 2MASS point source aperture and the LVL galaxy apertures.

## 5. Results

### 5.1. Detection Rate

The bottom panel of Figure 5 displays the detection rate as a function of  $B$  band apparent magnitude for the different *Spitzer* imaging channels. Nearly all galaxies are detected at all *Spitzer* wavelengths down to  $m_B \approx 14$  mag. Consistent with our pre-survey expectations, the  $m_B \sim 15.5$  mag cut-off for the outer tier of the sample that extends to 11 Mpc (see § 2) proved to be a useful sample selection criterion, as very few MIPS detections are available fainter than this magnitude limit. The inner tier/ANGST portion of the sample extends the sample to much fainter levels, as faint as  $m_B \approx 19$  mag in the cases of BK03N and M 81 Dwarf A. As expected for the optically-faint galaxies, the highest detection rates are found for the stellar-dominated 3.6 and  $4.5\ \mu\text{m}$  channels, while the 70 and  $160\ \mu\text{m}$  imaging proved to be far more challenging to convincingly detect cold dust emission. A stacking analysis (e.g., Dole et al. 2006) could be employed to obtain a better statistical understanding of the fainter galaxy population at long wavelengths.

### 5.2. Multi-Wavelength Spectral Energy Distributions

Figure 6 shows a *Spitzer* infrared mosaic of NGC 5236, spanning wavelengths where the emission is dominated by stars ( $3.6\ \mu\text{m}$ ), PAHs ( $8.0\ \mu\text{m}$ ), very small grains ( $24\ \mu\text{m}$ ) and large grains ( $70\ \mu\text{m}$ ). Figure 7 provides the ultraviolet-infrared spectral energy distributions for all 258 galaxies. The ultraviolet data are from Lee et al. (2009). The solid curve is the sum of a dust (dashed) and a stellar (dotted) model. The dust curve is a Dale & Helou (2002) model (least squares)

fitted to ratios of the observed 24, 70, and 160  $\mu\text{m}$  fluxes, and then scaled to match the overall infrared brightness. The  $\alpha_{\text{SED}}$  listed within each panel parametrizes the distribution of dust mass as a function of heating intensity, as described in Dale & Helou (2002). To quantify the uncertainty on  $\alpha_{\text{SED}}$  displayed within each panel of Figure 7, 1,000 Monte Carlo simulations of the fit to each galaxy’s far-infrared fluxes are performed, utilizing the tabulated flux uncertainties to add a random (Gaussian deviate) flux offset at each MIPS wavelength. The  $\alpha_{\text{SED}}$  uncertainties reflect the standard deviations in the simulations. The stellar curve is a 1 Gyr continuous star formation, solar metallicity curve from Vazquez & Leitherer (2005) fitted to the 2MASS data. The initial mass function for this curve utilizes a double power law form, with  $\alpha_{1,\text{IMF}} = 1.3$  for  $0.1 < m/M_{\odot} < 0.5$  and  $\alpha_{2,\text{IMF}} = 2.3$  for  $0.5 < m/M_{\odot} < 100$  (e.g., Kroupa 2002). Though this stellar curve is not adjusted for internal extinction and may not be applicable to many galaxies, it is included as a fiducial reference against which deviations in the ultraviolet can be compared from galaxy to galaxy.

The spectral energy distributions for the LVL sample range widely. There are stellar-dominated (NGC 0404, UGC 05373, UGCA 0193) and comparatively dusty (IC 5256, NGC 6503) systems; for sources detected by MIPS, the infrared-to-far-ultraviolet ratio in the sample spans more than three orders of magnitude, from 0.1 to over 100 (§ 5.4). There are galaxies with far-infrared spectral energy distributions indicative of warm (UGCA 0281) and cold dust grains (NGC 5055). Compared to what would be expected based on their stellar and far-infrared emission, many galaxies show a dearth of emission from PAHs in the 8.0  $\mu\text{m}$  band (e.g., ESO 245-G005, UGC 01249, UGC 05272). The variations in global spectral energy distributions are discussed in more detail below.

### 5.3. Infrared Colors

The IRAC-MIPS infrared colors for the LVL sample are displayed in Panel a of Figure 33. The  $f_{\nu}(70\mu\text{m})/f_{\nu}(160\mu\text{m})$  ratio typically traces the temperature of large interstellar grains, while the  $f_{\nu}(8.0\mu\text{m})/f_{\nu}(24\mu\text{m})$  ratio has several influences. The flux at 24  $\mu\text{m}$  mostly represents emission from very small grains (grains with effective radii of 15–40 Å; Draine & Li 2007), and the flux at 8.0  $\mu\text{m}$  can have contributions from stars, hot dust, PAHs, and AGN. Perhaps due to the diversity of emission mechanisms responsible for 8.0 and 24  $\mu\text{m}$  flux levels, the  $f_{\nu}(8.0\mu\text{m})/f_{\nu}(24\mu\text{m})$  ratio spans two orders of magnitude compared to the single factor of  $\sim 10$  stretch in the the  $f_{\nu}(70\mu\text{m})/f_{\nu}(160\mu\text{m})$  ratio. Since the LVL sample largely lacks “strong” AGN, loosely defined here as AGN that dominate a galaxy’s emission over substantial portions of the electromagnetic spectrum, it is unlikely that AGN contribute much to the scatter in Figure 33.

The far-infrared or total infrared, respectively commonly defined as the emission from 42–122  $\mu\text{m}$  (*FIR*) and 8–1000  $\mu\text{m}$  or 3–1100  $\mu\text{m}$  (*TIR*; Dale & Helou 2002), are frequently used as indications of the star formation rate in galaxies (Kennicutt 1998; Bell 2003). However, in many instances the far-infrared continuum is unavailable or not detected, so monochromatic infrared proxies for (*FIR*) or (*TIR*) are occasionally employed (e.g., Papovich & Bell 2002; Bavouzet et al. 2008). Hence, the tightness (dispersion) in monochromatic-to-bolometric ratios are of general inter-

est. Five flavors of these ratios are displayed in the remaining panels of Figure 33, and a tabulation of median LVL infrared colors and monochromatic-to-bolometric infrared ratios can be found in Table 4 along with their dispersions. Panel b of Figure 33 shows the distribution of the  $8.0\ \mu\text{m}$  emission with respect to the  $3\text{--}1100\ \mu\text{m}$  total infrared, a distribution which exhibits a dispersion of 0.23 dex, similar to that for  $f_\nu(70\mu\text{m})/f_\nu(160\mu\text{m})$  and  $f_\nu(8.0\mu\text{m})/f_\nu(24\mu\text{m})$ . While it is evident that the LVL sample is distributed fairly evenly by morphology across  $f_\nu(70\mu\text{m})/f_\nu(160\mu\text{m})$  ratios, the bulk of the systems exhibiting relatively low  $f_\nu(8.0\mu\text{m})/f_\nu(24\mu\text{m})$  and  $\nu f_\nu(8.0\mu\text{m})/TIR$  ratios are from late-type spirals and irregulars.

The preponderance of late-type spirals and irregulars showing relatively low  $8.0\ \mu\text{m}$  emission is amplified when “dust-only”  $8.0\ \mu\text{m}$  emission is considered. Panel c of Figure 33 shows a plot similar to that in Panel b but with the stellar emission removed using the expression presented in Helou et al. (2004):

$$\nu f_\nu(8.0\mu\text{m})_{\text{dust}} = \nu f_\nu(8.0\mu\text{m}) - \eta^{8*} \nu f_\nu(3.6\mu\text{m}) \quad (4)$$

where  $\eta^{8*} = 0.232 \times 3.6/8.0$ . The dispersion (0.44 dex) and overall range are significantly larger when the dust-only  $8.0\ \mu\text{m}$  emission is normalized to the total infrared. It is possible that a portion of these increases in dispersion and range are due to the inapplicability of Equation 4 to late-type spirals, but it should be noted that Equation 4 is based on a detailed analysis of NGC 300, a local system with an Sd morphological classification. Another possibility is that the late-type spirals and irregulars within LVL are on average less abundant in heavy metals, and thus either the formation of PAH molecules is starved or the relatively fragile PAHs are photo-dissociated in the hard radiation fields typically associated with low-metallicity environments (Engelbracht et al. 2005; Madden et al 2006; Wu et al. 2006; Dale et al. 2009; Sloan et al. 2008). Additional data and detailed follow-up utilizing LVL metallicities would be required to address this issue.

In contrast to the  $8.0\ \mu\text{m}$ -to- $TIR$  measures, the  $\nu f_\nu(24\mu\text{m})/TIR$  ratio (Panel d of Figure 33) shows a range less than an order of magnitude and a dispersion of 0.15 dex; the  $70\ \mu\text{m}$ -to- $TIR$  and  $160\ \mu\text{m}$ -to- $TIR$  ratios have even smaller dispersions (Panels e & f and Table 4). The implication is that, compared to the  $8.0\ \mu\text{m}$  emission from galaxies, the infrared emission from very small grains at  $24\ \mu\text{m}$  and from large grains at  $70$  and  $160\ \mu\text{m}$  are far more tightly coupled to the bolometric infrared emission. Such a conclusion may naturally arise from inspection of the global spectral energy distributions in Figure 7, but it is nonetheless important to emphasize the differences between what is being emitted in the mid-infrared versus the far-infrared. This result conceptually follows work by Calzetti et al. (2007) and Kennicutt et al. (2007; 2009), who show that  $24\ \mu\text{m}$  and total infrared fluxes are more effective than  $8.0\ \mu\text{m}$  fluxes at tracing a galaxy’s current star formation rate (they also show that these infrared fluxes correlate even better with star formation, to within  $\sim 0.1$  dex, if they are coupled with  $H\alpha$  to capture the unobscured portion of star formation).

The  $70\ \mu\text{m}$ -to- $TIR$  and  $160\ \mu\text{m}$ -to- $TIR$  cling remarkably closely to the model SED predictions, with dispersions of 0.038 and 0.031 dex, respectively. However, there is evidence for

#### 5.4. The Infrared-to-Ultraviolet Ratio and Ultraviolet Spectral Slope

The infrared-to-ultraviolet ratio is a coarse measure of dust extinction in the ultraviolet, and thus should be related to the amount of reddening in ultraviolet spectra. Indeed, starbursting galaxies follow a tight correlation between the ratio of infrared-to-ultraviolet emission and the ultraviolet spectral slope (e.g., Calzetti et al. 1994; Calzetti et al. 1997; Meurer et al. 1999). Compared to the relation defined by starbursts, normal star-forming galaxies are offset to redder ultraviolet spectral slopes, exhibit lower infrared-to-ultraviolet ratios, and show significantly larger scatter (Buat et al. 2002, 2005; Bell 2002; Kong et al. 2004; Gordon et al. 2004; Burgarella et al. 2005; Calzetti et al. 2005; Seibert et al. 2005; Cortese et al. 2006; Boissier et al. 2007; Gil de Paz et al. 2007; Dale et al. 2007). Offsets from the locus formed by starbursting and normal star-forming galaxies can be particularly pronounced for systems lacking significant current star formation, such as elliptical galaxies, systems for which the luminosity is more dominated by a passively evolving older, redder stellar population. The LVL survey provides a unique sample for exploring the relationship between the infrared-to-ultraviolet ratio and the ultraviolet slope, as it consists of a statistically complete set of star-forming galaxies, approximately half of which are dwarf/irregular systems.

Figure 34 displays the LVL infrared-to-ultraviolet ratios as a function of the ultraviolet spectral slope. The total infrared is computed from the MIPS 24, 70, and 160  $\mu\text{m}$  fluxes (Equation 4 in Dale & Helou 2002), and the ultraviolet data are from *GALEX* (Lee et al. 2009). As expected, the well-known starbursts in the LVL sample lie close to the starburst curve: NGC 0253, NGC 4631, NGC 4449, NGC 1705, and NGC 4736, with the latter formally known as a post-starburst galaxy (Walker, Lebofsky, & Rieke 1988). Overall, the LVL population is broadly segregated in the infrared-to-ultraviolet ratio according to optical morphology, with Sb and earlier-type galaxies showing relatively high values, Sc/Sd/Sm systems exhibiting intermediate values, and irregulars appearing near the bottom of the diagram. To explore this distribution further, in Figure 35 we plot an observable tracer of the “birthrate parameter” as a function of the (perpendicular) distance to the starburst curve in Figure 35. Following Carlos-Muñoz et al. (2009), the ratio of far-ultraviolet-to-near-infrared luminosity is used as a measure of the ratio of past-to-present star formation, sometimes referred to as the birthrate parameter (see also, for example, Boselli et al. 2001; Cortese et al. 2006). This ratio represents the birthrate parameter since the far-ultraviolet traces star formation over 100 Myr timescales whereas the near-infrared probes the total stellar mass built up over much longer timescales. Here the far-ultraviolet emission is corrected for extinction using the infrared-to-ultraviolet-based recipe formulated in Buat et al. (2005). The distribution of far-ultraviolet extinctions estimated by this method is provided in Figure 36. Ninety percent of the sources have far-ultraviolet extinctions less than 1.7 mag, or equivalently, ninety percent have optical extinctions  $A_V \lesssim 0.6$  mag using the Li & Draine (2001) extinction curve.

There is a clear trend in Figure 35, with lower birthrate systems exhibiting larger distances from the starburst trend. The deviations from the starburst curve are presumably driven by the differential effects young and old stellar populations and their local dust opacities have on

the intrinsic and dust-reddened luminosities, suggesting that a galaxy’s star formation history plays an important role in determining its location within Figure 34. To more directly interpret these deviations from the starburst curve as a function of the age of the stellar population, the righthand axis of Figure 35 is quantified according to the age inferred from theoretical spectra. This comparison is accomplished by convolving *GALEX* far-ultraviolet and *Spitzer* 3.6  $\mu\text{m}$  filter transmission profiles with stellar spectra similar to those described in § 5.2 but for a wide range of ages (1 Myr to 10 Gyr). The ages for the respective simulated spectra are shown along the righthand axis at levels corresponding to the computed theoretical far-ultraviolet-to-near-infrared ratios along the lefthand axis. Assuming these theoretical spectra are broadly applicable to the LVL sample, the star formation timescales range from several million years up to a few billion years, with the longest-lasting star formation episodes corresponding to the largest deviations from the starburst curve. It should be stressed that this comparison with theoretical stellar population ages is indicative—if the actual star formation rates have been declining with time instead of remaining constant, then the age axis in Figure 35 overestimates the true ages.

## 6. Summary

The Local Volume Legacy is a *Spitzer Space Telescope* legacy program built upon a foundation of *GALEX* ultraviolet and ground-based  $\text{H}\alpha$  imaging of 258 galaxies within 11 Mpc, nearly half of which are dwarf/irregulars. The proximity and nearly volume-limited nature of the survey are key aspects, enabling multi-wavelength analyses of star formation with high spatial resolution in a manner that is statistically representative of the nearby galaxy population. First results are reported based on infrared and ultraviolet fluxes. Whereas the far-infrared closely tracks the total-infrared emission, the mid-infrared-to-total-infrared ratios show large dispersions. The large scatter in comparing dust emission at 8.0  $\mu\text{m}$  and total dust emission is likely due to the notable deficiency of PAH emission from the low-metallicity galaxies prevalent in the LVL survey. The LVL sample shows a correlation between infrared-to-ultraviolet ratio and ultraviolet spectral slope, but it is shifted to redder colors than what is seen for starburst galaxies. Theoretical models are utilized to buttress the idea that deviations from the starburst relation correspond to the age of the stellar population.

Support for this work, part of the *Spitzer Space Telescope* Legacy Science Program, was provided by NASA through Contract Number XXX issued by the Jet Propulsion Laboratory, California Institute of Technology under NASA contract 1407. This research has made use of the NASA/IPAC Extragalactic Database which is operated by JPL/Caltech, under contract with NASA. This publication makes use of data products from the Two Micron All Sky Survey, which is a joint project of the University of Massachusetts and the Infrared Processing and Analysis Center/California Institute of Technology, funded by the National Aeronautics and Space Administration and the National Science Foundation. IRAF, the Image Reduction and Analysis Facility, has been devel-

oped by the National Optical Astronomy Observatories and the Space Telescope Science Institute. We gratefully acknowledge NASA’s support for construction, operation, and science analysis for the GALEX mission, developed in cooperation with the Centre National d’Etudes Spatiales of France and the Korean Ministry of Science and Technology.

## REFERENCES

- Bavouzet, N., Dole, H., Le Floch, E., Caputi, K.I., Lagache, G., & Kochanek, C.S. 2008, *A&A*, 479, 83
- Bell, E.F. 2002, *ApJ*, 577, 150
- Bell, E.F. 2003, *ApJ*, 586, 794
- Bernard, J.-P. et al. 2008, *AJ*, 136, 919
- Boissier, S. et al. 2007, *ApJS*, 173, 524
- Boselli, A., Gavazzi, G., Donas, J., & Scodeggio, M. 2001, 121, 753
- Buat, V. et al. 2001, *ApJ*, 619, L51
- Buat, V., Boselli, A., Gavazzi, G., & Bonfanti, C. 2002, *A&A*, 383, 801
- Buat, V. et al. 2005, *ApJ*, 619, L51
- Burgarella, D., Buat, V., & Iglesias-Páramo, J. 2005, *MNRAS*, 360, 1413
- Calzetti, D. 1997, *AJ*, 113, 162
- Calzetti, D. et al. 2005, *ApJ*, 633, 871
- Calzetti, D. et al. 2007, *ApJ*, 666, 870
- Carlos-Muñoz, J. et al. 2009, in preparation
- Cortese, L., Boselli, A., Buat, V., Gavazzi, G., Boissier, S., Gil de Paz, A., Seibert, M., Madore, B.F., & Martin, C. 2006, *ApJ*, 637, 242
- Cortese, L., 2006, *ApJ*, 636, 242
- Dalcanton, J. et al. 2009, *ApJ*, in press
- Dale, D.A. et al. 2000, *AJ*, 120, 583
- Dale, D.A., Helou, G., Contursi, A., Silberman, N.A., & Kolhatkar, S. 2001, *ApJ*, 549, 215
- Dale, D.A. & Helou, G. 2002, *ApJ*, 576, 159

- Dale, D.A. et al. 2007, *ApJ*, 655, 863
- Dale, D.A. et al. 2009, *ApJ*, in press
- Dole, H. et al. 2006, *A&A*, 451, 417
- Draine, B.T., & Li, A. 2007, *ApJ*, 657, 810
- Engelbracht, C.W., Gordon, K.D., Rieke, G.H., Werner, M.W., Dale, D.A., & Latter, W.B. 2005, *ApJ*, 628, L29
- Engelbracht, C.W. et al. 2007, *PASP*, 119, 914
- Fazio, G.G. et al. 2004, *ApJS*, 154, 10
- Gil de Paz, A. et al. 2007, *ApJS*, 173, 185
- Gil de Paz, A. et al. 2009, in preparation
- Gordon, K. et al. 2004, *ApJS*, 154, 215
- Gordon, K. et al. 2005, *PASP*, 117, 503
- Gordon, K. et al. 2007, *PASP*, 119, 1019
- Helou, G. et al. 2004, *ApJS*, 154, 253
- Hunter, D.A. et al. 2009, in preparation
- Jarrett, T.H., Chester, T., Cutri, R., Schneider, S.E., & Huchra, J.P. 2003, *AJ*, 125, 525
- Kennicutt, R.C. 1998, *ARA&A*, 36, 189
- Kennicutt, R.C. et al. 2003, *PASP*, 115, 928
- Kennicutt, R.C. et al. 2007, *ApJ*, 671, 333
- Kennicutt, R.C., Lee, J.C., Funes, J.G., Sakai, S., & Akiyama, S. 2008, *ApJS*, 178, 247
- Kennicutt, R.C. et al. 2009, *ApJ*, submitted
- Kirby, E.M., Jerjen, H., Ryder, S.D., & Driver, S.P. 2008, *ApJ*, in press
- Kong, X., Charlot, S., Brinchmann, J., & Fall, S.M. 2004, *MNRAS*, 349, 769
- Kroupa, P. 2002, *Science*, 295, 82
- Lee, J.C. 2006, Ph.D. thesis, University of Arizona
- Lee, J.C., Kennicutt, R.C., Funes, J.G., Sakai, S., & Akiyama, S. 2007, *ApJ*, 671, 113

- Lee, J.C. et al. 2009, in preparation
- Leroy, A., Bolatto, A., Stanimirovic, S., Mizuno, N., Israel, F., & Bot, C. 2007, *ApJ*, 658, 1027
- Li, A. & Draine, B.T. 2001, *ApJ*, 554, 778
- Madden, S.C., Galliano, F., Jones, A.P., & Sauvage, M. 2006, *A&A*, 446, 877
- Meurer, G.R., Heckman, T.M., & Calzetti, D. 1999, *ApJ*, 521, 64
- Papovich, C. & Bell, E.F. 2002, *ApJ*, 579, L1
- Regan, M. et al. 2006, *ApJ*, 652, 1112
- Rieke, G.H. et al. 2004, *ApJS*, 154, 25
- Ryan-Weber, E. et al. 2002, *AJ*, 124, 1954
- Schlegel, D.J., Finkbeiner, D.P., & Davis, M. 1998, *ApJ*, 500, 525
- Seibert, M. et al. 2005, *ApJ*, 619, L55
- Sloan, G.C., Kraemer, K.E., Wood, P.R., Zijlstra, A.A., Bernard-Salas, J., Devost, D., & Houck, J.R. 2008, *ApJ*, in press
- Skrutskie, M.F. et al. 2006, *AJ*, 131, 1163
- Stansberry, J.A. et al. 2007, *PASP*, 119, 1038
- Walker, C.E., Lebofsky, M.J., & Rieke, G.H. 1988, *ApJ*, 325, 687
- Wu, Y., Charmandaris, V., Hao, H., Brandl, B.R., Bernard-Salas, J., Spoon, H.W.W., & Houck, J.R. 2006, *ApJ*, 639, 157
- Vazquez, G.A. & Leitherer, C. 2005, *ApJ*, 621, 695
- Yan, L. et al. 2004, *ApJS*, 154, 60



Table 1. Galaxy Sample and Infrared Photometry Apertures

Galaxy	$m_B$ (mag)	$cz$ (km s <sup>-1</sup> )	$D$ (Mpc)	$T$	$E(B-V)$ (mag)	$\alpha_0$ & $\delta_0$ (J2000)	$2a$ ( $''$ )	$2b$ ( $''$ )	PA ( $^\circ$ )
WLM	11.03	-116	0.92	10	0.04	000158.9–152655	672	340	0
NGC0024	12.19	554	8.13	5	0.02	000955.9–245755	301	216	225
NGC0045	11.32	471	7.07	8	0.02	001404.6–231101	577	456	336
NGC0055	8.42	129	2.17	9	0.01	001508.2–391256	2251	714	106
NGC0059	13.12	382	5.30	-3	0.02	001525.8–212646	256	180	302
ESO410-G005	14.95	...	1.90	-1	0.01	001531.0–321048	193	144	308
Sculptor-dE1	17.78	...	4.20	10	0.02	002351.6–244204	160	103	0
ESO294-G010	15.52	117	1.90	-3	0.01	002633.7–415120	165	102	0
IC1574	14.50	361	4.92	10	0.02	004303.9–221444	202	123	0
NGC0247	9.67	160	3.65	7	0.02	004708.9–204456	1476	581	352
NGC0253	8.04	241	3.94	5	0.02	004733.2–251734	2050	808	50
ESO540-G030	16.46	...	3.40	-1	0.02	004920.8–180406	168	148	0
UGCA015	15.38	301	3.34	10	0.02	004949.1–210049	150	78	28
ESO540-G032	16.55	...	3.40	-3	0.02	005024.6–195427	100	91	0
UGC00521	15.31	659	11.32	10	0.07	005112.2+120129	107	107	90
SMC <sup>a</sup>	2.70	158	0.06	9	0.42	...	...	...	...
NGC0300	8.72	144	2.00	7	0.01	005458.1–374054	1507	1128	114
UGC00668	9.88	-234	0.65	10	0.02	010450.5+020720	682	547	60
UGC00685	14.20	157	4.70	9	0.06	010723.2+164101	179	147	122
UGC00695	15.28	664	10.20	6	0.03	010746.5+010347	129	109	0
NGC404	11.51	-48	3.10	-1	0.06	010927.7+354307	234	229	0
UGC00891	14.72	643	10.84	9	0.03	012118.9+122438	194	118	42
UGC01056	14.87	595	10.32	10	0.07	012847.6+164117	125	117	0
UGC01104	14.41	686	7.50	9	0.06	013242.5+181906	166	103	0
NGC0598	6.27	-179	0.84	6	0.04	013350.8+303920	4453	2762	12
NGC0625	11.71	405	4.07	9	0.02	013504.4–412624	499	256	90
NGC0628	9.95	657	7.30	5	0.07	013641.8+154717	721	717	338
UGC01176	14.40	633	9.00	10	0.06	014010.0+155426	202	168	25
ESO245-G005	12.70	395	4.43	10	0.02	014503.6–433528	358	253	318
UGC01249	12.07	338	7.20	9	0.08	014729.0+271960	524	290	331
NGC0672	11.47	421	7.20	6	0.08	014752.7+272550	556	361	67
ESO245-G007	13.33	56	0.44	10	0.02	015106.1–442647	288	240	0
NGC0784	12.23	198	5.19	8	0.06	020116.7+285005	480	191	3
NGC855	13.30	595	9.73	-5	0.07	021403.9+275239	190	171	68
ESO115-G021	13.34	513	4.99	8	0.03	023746.8–612018	332	147	221
ESO154-G023	12.69	578	5.76	8	0.02	025652.4–543359	486	248	39
NGC1291	9.39	839	9.37	0	0.01	031719.1–410632	840	804	0
NGC1313	9.20	475	4.15	7	0.11	031810.0–662908	896	694	338
NGC1311	13.18	571	5.45	9	0.02	032006.9–521114	300	141	36
UGC02716	14.64	379	6.23	8	0.14	032407.9+174512	174	123	90
IC1959	13.26	640	6.06	9	0.01	033312.4–502445	253	114	330
NGC1487	12.34	848	9.08	7	0.01	035545.5–422200	391	260	63
NGC1510	13.47	913	9.84	-2	0.01	040332.7–432359	126	122	0
NGC1512	11.13	896	9.64	1	0.01	040355.0–432044	491	288	55
NGC1522	13.93	905	9.32	11	0.01	040607.6–524011	151	99	37

Table 1—Continued

Galaxy	$m_B$ (mag)	$cz$ (km s <sup>-1</sup> )	$D$ (Mpc)	$T$	$E(B-V)$ (mag)	$\alpha_0$ & $\delta_0$ (J2000)	$2a$ ( $''$ )	$2b$ ( $''$ )	PA ( $^\circ$ )
IC2049	15.19	869	16.73	7	0.02	041204.2–583327	119	106	0
ESO483-G013	14.18	823	10.43	–3	0.05	041240.9–230928	205	147	322
ESO158-G003	14.01	975	9.96	9	0.01	044615.6–572044	199	172	0
ESO119-G016	14.79	969	9.84	10	0.02	045128.6–613905	221	116	26
NGC1705	12.77	628	5.10	11	0.01	045413.5–532137	167	120	220
NGC1744	11.60	748	7.65	7	0.04	045957.8–260116	410	225	349
NGC1796	12.86	987	10.32	5	0.02	050242.8–610822	256	205	99
ESO486-G021	14.47	865	8.89	2	0.03	050319.9–252524	115	99	90
MCG-05-13-004 <sup>b</sup>	13.22	686	6.63	9	0.01	...	...	...	...
NGC1800	13.07	803	8.24	9	0.01	050625.7–315715	229	163	107
UGCA106	13.05	933	9.77	9	0.02	051159.2–325817	323	245	14
LMC <sup>a</sup>	0.91	278	0.05	9	0.92	...	...	...	...
KKH037	16.40	–148	3.39	10	0.07	064744.2+800723	105	81	90
NGC2366	11.43	100	3.19	10	0.04	072850.9+691248	501	298	31
UGCA133	15.80	...	3.20	–3	0.04	073412.2+665313	215	153	0
NGC2403	8.93	131	3.22	6	0.04	073655.0+653554	1164	848	130
NGC2500	12.20	514	7.63	7	0.04	080152.4+504405	274	234	75
NGC2537	12.82	447	6.90	9	0.05	081314.7+455936	211	199	0
UGC04278	13.07	565	7.59	7	0.05	081358.7+454445	319	79	351
UGC04305	11.10	157	3.39	10	0.03	081906.8+704309	442	430	90
NGC2552	12.56	524	7.65	9	0.05	081920.0+500038	312	205	54
M81dwA	18.69	113	3.55	10	0.02	082356.0+710145	78	78	90
UGC04426	15.00	397	10.28	10	0.04	082828.4+415124	206	145	10
UGC04459	14.78	19	3.56	10	0.04	083406.8+661036	134	111	120
UGC04483	15.27	178	3.21	10	0.03	083703.5+694632	94	58	0
NGC2683	10.64	411	7.70	3	0.03	085241.0+332516	822	420	41
UGC04704	15.33	596	7.75	8	0.03	085902.5+391223	303	108	296
UGC04787	15.41	552	6.53	8	0.02	090735.1+331638	211	107	5
UGC04998	14.72	623	10.50	10	0.06	092512.9+682258	187	162	71
NGC2903	9.68	556	8.90	4	0.03	093210.9+213005	824	461	17
UGC05076	15.21	571	8.31	10	0.02	093236.5+515216	165	139	90
CGCG035-007	15.46	574	5.17	5	0.04	093444.9+062532	126	96	63
UGC05139	14.17	143	3.84	10	0.05	094030.5+711033	265	228	210
IC0559	14.82	513	4.93	5	0.03	094443.9+093655	135	124	63
F8D1	16.14	...	3.80	–3	0.11	094447.1+672619	254	254	90
[FM2000]1	17.80	...	3.40	–3	0.08	094510.0+684547	89	89	90
NGC2976	11.24	3	3.56	5	0.07	094715.9+675507	457	312	322
LEDA166101	16.94	...	3.50	–3	0.14	095013.0+673037	219	152	33
UGC05272	15.41	520	7.10	10	0.02	095023.1+312917	196	96	112
UGC05288	14.32	557	6.80	8	0.03	095116.9+074939	164	141	331
BK03N	18.78	–40	4.02	10	0.08	095348.5+685808	41	41	90
NGC3031	7.89	–34	3.63	2	0.08	095531.8+690403	1629	1123	154
NGC3034	9.30	203	3.53	7	0.16	095552.1+694057	698	581	65
UGC05340	14.76	503	5.90	10	0.02	095645.8+284932	115	81	0
KDG061	15.17	–135	3.60	8	0.07	095704.5+683536	214	119	49

Table 1—Continued

Galaxy	$m_B$ (mag)	$cz$ (km s <sup>-1</sup> )	$D$ (Mpc)	$T$	$E(B-V)$ (mag)	$\alpha_0$ & $\delta_0$ (J2000)	$2a$ ( $''$ )	$2b$ ( $''$ )	PA ( $^\circ$ )
UGC05336	14.30	46	3.70	10	0.08	095729.2+690250	248	181	220
Arp'sLoop	16.76	99	3.90	10	0.08	095732.7+691700	137	137	90
UGC05364	12.92	20	0.69	10	0.02	095926.5+304458	311	192	67
UGC05373	11.85	301	1.44	10	0.03	095959.5+051957	333	268	90
KKH057	17.95	...	3.90	-3	0.02	100014.6+631058	73	53	45
UGCA193	14.84	662	9.70	7	0.04	100236.4-060031	284	69	14
NGC3109	10.39	403	1.34	9	0.07	100307.6-260948	900	334	90
NGC3077	10.61	14	3.82	6	0.07	100319.2+684401	576	483	64
AM1001-270	16.51	362	1.30	10	0.08	100403.0-271948	169	96	319
BK05N	17.77	...	3.80	-3	0.06	100441.6+681526	207	102	330
UGC5428	15.95	-129	3.50	10	0.10	100507.5+663339	196	168	90
UGC05423	15.20	350	5.30	10	0.08	100531.3+702152	107	70	140
UGC5442	15.78	-18	3.70	-3	0.05	100701.2+674938	197	124	34
UGC05456	13.72	544	3.80	5	0.04	100719.4+102151	161	121	322
IKN	17.31	...	3.70	-3	0.06	100805.9+682357	180	156	180
SextansA	11.86	324	1.32	10	0.04	101100.8-044134	285	258	0
[HS98]117	17.01	-37	4.00	10	0.12	102125.5+710652	213	129	0
NGC3239	11.73	753	8.29	9	0.03	102504.7+170856	315	272	63
DDO078	15.84	55	3.70	-3	0.02	102627.4+673916	141	141	90
UGC05672	15.14	531	6.30	5	0.02	102820.9+223409	289	104	340
UGC05666	10.80	57	4.02	9	0.04	102822.7+682448	827	377	230
UGC05692	13.71	180	4.00	9	0.04	103036.4+703713	306	211	0
NGC3274	13.21	537	6.50	7	0.02	103216.6+274007	186	135	90
BK06N	16.85	...	3.80	-3	0.01	103432.4+660036	231	108	304
NGC3299	14.11	641	10.40	8	0.02	103623.8+124231	264	207	0
UGC05764	15.21	586	7.08	10	0.02	103643.1+313245	150	85	44
UGC05797	15.00	713	6.84	10	0.03	103925.4+014302	141	138	0
UGC05829	13.73	629	7.88	10	0.02	104241.6+342657	270	204	57
NGC3344	10.45	586	6.64	4	0.03	104332.3+245524	396	394	0
NGC3351	10.53	778	10.00	3	0.03	104357.5+114219	586	457	10
NGC3368	10.11	897	10.52	2	0.03	104645.5+114905	511	349	346
UGC05889	14.22	572	9.30	9	0.03	104722.2+140416	202	190	0
UGC05923	14.03	712	7.16	0	0.03	104907.5+065504	113	70	353
UGC05918	15.22	340	7.40	10	0.01	104936.5+653149	140	113	65
NGC3432	11.67	616	7.89	9	0.01	105232.7+363747	476	187	38
KDG73	17.28	-132	3.70	10	0.02	105256.5+693317	126	100	345
NGC3486	11.05	681	8.24	5	0.02	110023.2+285834	495	389	83
NGC3510	14.30	705	8.57	8	0.03	110343.6+285301	310	136	345
NGC3521	9.83	805	8.03	4	0.06	110548.7-000222	767	494	343
NGC3593	11.86	628	6.52	0	0.02	111436.7+124903	373	211	86
NGC3623	10.25	807	8.95	1	0.02	111856.0+130525	663	331	352
NGC3627	9.65	727	10.05	3	0.03	112013.4+125927	746	487	347
NGC3628	10.28	843	9.45	3	0.03	112014.8+133518	1039	619	102
UGC06457	15.00	963	10.24	10	0.03	112712.4-005944	150	111	19
UGC06541	14.40	249	3.89	11	0.02	113328.1+491428	124	87	316

Table 1—Continued

Galaxy	$m_B$ (mag)	$cz$ (km s <sup>-1</sup> )	$D$ (Mpc)	$T$	$E(B-V)$ (mag)	$\alpha_0$ & $\delta_0$ (J2000)	$2a$ ( $''$ )	$2b$ ( $''$ )	PA ( $^\circ$ )
NGC3738	11.97	229	4.90	10	0.01	113548.6+543129	220	175	343
NGC3741	14.49	229	3.19	10	0.02	113606.0+451709	137	108	7
UGC06782	15.07	525	14.00	9	0.03	114857.2+235016	120	120	90
UGC06817	13.56	242	2.64	10	0.03	115054.1+385259	233	174	39
UGC06900	14.80	590	7.47	10	0.02	115539.9+313106	204	145	107
NGC4020	13.82	760	9.68	7	0.02	115856.5+302442	222	136	18
NGC4068	13.02	210	4.31	10	0.02	120402.8+523523	255	178	22
NGC4080	14.28	567	6.92	10	0.03	120451.8+265932	153	131	312
NGC4096	11.48	566	8.28	5	0.02	120600.3+472847	556	243	18
NGC4144	12.05	265	9.80	6	0.01	120958.9+462730	437	189	103
NGC4163	13.75	165	2.96	10	0.02	121208.9+361008	213	164	4
NGC4190	13.90	228	3.50	10	0.03	121344.6+363808	210	164	45
ESO321-G014	15.63	610	3.20	10	0.09	121349.3-381347	171	105	22
UGC07242	14.65	68	5.42	6	0.02	121408.4+660541	157	85	0
UGCA276	15.70	284	3.18	10	0.02	121459.9+361301	161	143	301
UGC07267	15.29	472	7.33	8	0.02	121523.9+512104	189	98	45
NGC4214	10.24	291	2.92	10	0.02	121538.4+361943	476	452	0
CGCG269-049	15.30	159	3.23	10	0.02	121547.3+522315	94	67	319
NGC4236	10.05	0	4.45	8	0.01	121635.9+692808	1129	420	155
NGC4244	10.88	244	4.49	6	0.02	121729.8+374825	1182	242	47
NGC4242	11.37	517	7.43	8	0.01	121730.4+453710	410	312	28
UGC07321	14.15	408	20.00	7	0.03	121734.3+223225	370	78	81
NGC4248	13.21	484	7.24	3	0.02	121750.7+472432	251	170	107
NGC4258	9.10	448	7.98	4	0.02	121854.9+471824	1160	529	333
ISZ399	14.72	900	8.97	11	0.06	121959.5-172331	132	102	314
NGC4288	13.26	535	7.67	7	0.01	122038.3+461737	190	163	139
UGC07408	13.35	462	6.87	9	0.01	122115.5+454900	220	192	90
UGC07490	13.05	465	8.40	9	0.02	122424.6+701958	226	220	0
NGC4395	10.64	319	4.61	9	0.02	122552.2+333315	1008	790	328
UGCA281	15.36	281	5.70	11	0.01	122616.7+482939	87	73	81
UGC07559	14.20	218	4.87	10	0.01	122706.1+370830	154	108	336
UGC07577	12.84	196	2.74	10	0.02	122743.4+432926	312	218	301
NGC4449	9.99	207	4.21	10	0.02	122810.4+440525	473	354	57
UGC07599	14.88	278	6.90	8	0.02	122828.2+371401	92	70	312
UGC07605	14.79	309	4.43	10	0.01	122838.4+354301	141	86	17
NGC4455	13.80	637	7.75	7	0.02	122844.0+224918	200	90	198
UGC07608	13.67	538	7.76	10	0.02	122845.2+431332	156	138	0
NGC4460	12.78	490	9.59	-1	0.02	122845.9+445157	338	147	37
UGC07639	13.99	382	8.00	10	0.01	122953.3+473154	231	140	334
NGC4485	12.32	493	7.07	10	0.02	123031.8+414202	180	134	343
NGC4490	10.22	565	8.03	7	0.02	123034.4+413841	418	232	121
UGC07690	13.10	537	7.73	10	0.03	123226.8+424225	195	151	36
UGC07699	13.60	496	6.85	6	0.01	123248.0+373718	270	105	32
UGC07698	13.00	331	6.10	10	0.02	123254.0+313218	217	127	342
UGC07719	15.33	678	9.39	8	0.02	123400.6+390116	158	86	347

Table 1—Continued

Galaxy	$m_B$ (mag)	$cz$ (km s <sup>-1</sup> )	$D$ (Mpc)	$T$	$E(B-V)$ (mag)	$\alpha_0$ & $\delta_0$ (J2000)	$2a$ ( $''$ )	$2b$ ( $''$ )	PA ( $^\circ$ )
UGC07774	15.02	526	7.44	7	0.02	123622.8+400019	201	57	100
UGCA292	16.10	307	3.10	10	0.02	123840.1+324601	60	42	325
NGC4594	8.98	1024	9.33	1	0.05	123959.4–113714	555	233	90
NGC4605	10.89	143	5.47	5	0.01	123958.9+613628	498	330	303
NGC4618	11.22	544	7.79	8	0.02	124133.3+410841	335	267	22
NGC4625	12.92	609	8.65	9	0.02	124152.3+411618	198	191	140
NGC4631	9.75	606	8.05	7	0.02	124203.7+323205	953	540	80
UGC07866	13.71	354	4.57	10	0.02	124215.0+383020	162	125	357
NGC4656	10.96	646	8.59	9	0.01	124356.2+320930	719	255	220
UGC07916	15.00	607	8.21	10	0.02	124425.1+342312	150	102	90
UGC07950	15.10	502	7.91	10	0.02	124656.2+513649	144	124	0
UGC07949	15.12	333	9.90	10	0.02	124700.7+362850	124	85	90
NGC4707	13.40	468	7.44	9	0.01	124823.3+510952	207	177	20
NGC4736	8.99	308	4.66	2	0.02	125056.7+410706	1033	825	100
UGC08024	13.94	374	4.30	10	0.01	125405.2+270854	199	126	213
NGC4826	9.36	408	7.50	2	0.04	125642.8+214050	723	449	113
UGC08091	14.68	214	2.13	10	0.03	125839.7+141306	125	92	32
UGCA319	14.96	747	7.40	9	0.08	130214.4–171417	130	90	24
UGCA320	13.52	744	7.24	9	0.08	130317.0–172529	491	163	114
UGC08188	12.40	321	4.49	9	0.01	130550.8+373615	379	326	90
UGC08201	12.80	37	4.57	10	0.02	130625.0+674226	268	150	90
MCG-03-34-002	14.79	922	10.16	4	0.08	130756.6–164120	130	80	320
UGC08245	15.22	70	3.64	10	0.03	130835.3+785612	201	105	70
NGC5023	12.85	407	5.40	6	0.02	131211.7+440221	410	127	26
CGCG217-018	15.10	570	8.21	10	0.01	131251.6+403232	114	87	35
UGC08313	14.78	625	8.72	5	0.01	131354.3+421231	191	114	30
UGC08320	13.11	192	4.33	10	0.02	131426.5+455527	292	198	341
UGC08331	14.31	260	8.20	10	0.01	131529.6+473004	236	115	323
NGC5055	9.31	504	7.55	4	0.02	131548.3+420142	893	683	101
NGC5068	10.70	673	6.24	6	0.10	131855.4–210212	613	593	90
IC4247	14.57	274	4.97	2	0.06	132644.2–302143	129	78	333
NGC5204	11.73	201	4.65	9	0.01	132936.0+582510	338	211	351
NGC5194	8.96	463	8.00	4	0.04	132950.6+471307	1699	1130	15
NGC5195	10.45	465	8.00	2	0.04	132959.4+471556	203	192	0
UGC08508	13.94	62	2.69	10	0.02	133043.1+545436	160	120	305
NGC5229	14.18	364	5.10	7	0.02	133402.9+475452	279	102	347
NGC5238	13.60	235	5.20	8	0.01	133442.8+513650	216	166	0
[KK98]208	14.30	381	4.68	10	0.04	133635.5–293417	360	150	57
NGC5236	8.20	516	4.47	5	0.07	133700.8–295224	1100	1055	0
ESO444-G084	15.48	587	4.61	10	0.07	133720.2–280244	84	78	0
UGC08638	15.10	274	4.27	10	0.01	133919.4+244634	179	132	73
UGC08651	14.45	201	3.02	10	0.01	133953.5+404423	194	140	59
NGC5253	10.87	404	3.15	11	0.06	133956.1–313832	351	193	44
NGC5264	12.60	478	4.53	9	0.05	134136.0–295448	268	226	66
UGC08760	14.45	193	3.24	10	0.02	135051.3+380113	216	113	29

Table 1—Continued

Galaxy	$m_B$ (mag)	$cz$ (km s <sup>-1</sup> )	$D$ (Mpc)	$T$	$E(B-V)$ (mag)	$\alpha_0$ & $\delta_0$ (J2000)	$2a$ ( $''$ )	$2b$ ( $''$ )	PA ( $^\circ$ )
KKH086	16.99	287	2.60	10	0.03	135433.8+041443	131	83	0
UGC08837	13.71	144	8.30	10	0.01	135444.0+535347	364	148	17
UGC08833	15.15	228	3.20	10	0.01	135448.4+355018	121	115	0
NGC5457	8.31	241	6.70	6	0.01	140312.2+542307	1450	1039	37
NGC5474	11.82	273	7.20	6	0.01	140459.9+533913	386	335	210
NGC5477	14.24	304	7.70	9	0.01	140533.0+542732	169	124	64
[KK98]230	17.84	62	2.14	10	0.01	140710.4+350335	67	49	0
UGC09128	14.46	154	2.24	10	0.02	141556.8+230321	127	88	36
NGC5585	11.20	305	5.70	7	0.02	141948.4+564349	392	266	38
UGC09240	13.31	150	2.80	10	0.01	142443.4+443134	222	182	90
UGC09405	14.57	222	8.00	10	0.01	143524.0+571516	199	136	333
MRK475	15.46	583	9.02	11	0.01	143905.5+364819	72	71	196
NGC5832	14.09	447	8.74	3	0.03	145747.6+714056	293	180	49
NGC5949	13.37	435	8.53	4	0.02	152800.3+644548	219	135	324
UGC09992	14.86	427	8.56	10	0.04	154147.9+671515	156	109	340
KKR25	16.53	-139	1.90	10	0.01	161347.6+542216	94	87	0
NGC6503	10.91	60	5.27	6	0.03	174927.5+700838	394	217	120
IC4951	13.91	794	9.34	8	0.04	200931.8-615104	225	92	355
DDO210	14.14	-137	0.94	10	0.05	204651.6-125044	155	72	103
IC5052	11.79	598	5.86	7	0.05	205206.0-691201	450	168	323
NGC7064	13.10	797	9.86	5	0.01	212903.4-524605	250	81	90
NGC7090	11.33	857	10.41	5	0.02	213628.8-543320	539	161	308
IC5152	10.68	124	1.97	10	0.03	220242.0-511741	312	274	90
IC5256	14.58	950	10.76	8	0.03	224945.4-684127	124	76	22
UGCA438	14.67	62	2.22	10	0.01	232627.4-322317	189	163	0
ESO347-G017	14.41	690	9.37	9	0.02	232655.9-372050	212	129	90
UGC12613	12.50	-183	0.76	10	0.07	232833.7+144437	461	269	113
IC5332	11.21	706	9.53	7	0.02	233427.6-360601	645	573	0
NGC7713	11.51	689	9.28	7	0.02	233615.4-375616	370	227	345
UGCA442	13.60	267	4.27	9	0.02	234346.7-315724	245	117	43
KKH098	17.22	-137	2.50	10	0.12	234534.1+384301	126	79	5
ESO149-G003	15.04	594	6.40	10	0.01	235202.4-523428	249	100	332
NGC7793	9.63	230	3.91	7	0.02	235750.4-323530	755	499	90

Note. — Magnitudes, redshifts, distances, and optical morphologies are from Kennicutt et al. (2008), and the Milky Way foreground extinctions are from Schlegel, Finkbeiner, & Davis(1998). The position angles in the above ellipse parameters are measured east of north.

<sup>a</sup>Infrared photometry for the Large and Small Magellanic Clouds are from Bernard et al. (2008) and Leroy et al. (2007), respectively.

<sup>b</sup>NGC 1800 and MCG-05-13-004 spatially overlap so separate photometry for MCG-05-13-004 is not provided.

Table 2. Infrared Flux Densities

Galaxy	2MASS J 1.25 $\mu\text{m}$ (Jy)	2MASS H 1.65 $\mu\text{m}$ (Jy)	2MASS K <sub>s</sub> 2.17 $\mu\text{m}$ (Jy)	IRAC 3.6 $\mu\text{m}$ (Jy)	IRAC 4.5 $\mu\text{m}$ (Jy)	IRAC 5.8 $\mu\text{m}$ (Jy)	IRAC 8.0 $\mu\text{m}$ (Jy)	MIPS 24 $\mu\text{m}$ (Jy)	MIPS 70 $\mu\text{m}$ (Jy)	MIPS 160 $\mu\text{m}$ (Jy)
WLM <sup>e f</sup>	2.45±0.24E-1	3.13±0.31E-1	1.17±0.12E-1	9.09±1.23E-2	6.28±0.86E-2	4.87±0.62E-2	5.07±0.63E-2	7.58±0.82E-2	2.00±0.25E 0	3.88±0.61E 0
NGC0024 <sup>e f</sup>	2.32±0.23E-1	2.49±0.25E-1	1.90±0.19E-1	1.04±0.14E-1	7.06±1.01E-2	8.81±1.16E-2	1.28±0.16E-1	1.30±0.07E-1	2.23±0.19E 0	7.00±1.05E 0
NGC0045	2.08±0.21E-1	2.29±0.23E-1	1.67±0.17E-1	2.00±0.27E-1	1.27±0.17E-1	6.56±0.83E-2	1.69±0.21E-1	1.87±0.20E-1	3.87±0.47E 0	1.23±0.19E 0
NGC0055 <sup>e f</sup>	3.31±0.33E 0	3.08±0.31E 0	2.63±0.26E 0	2.03±0.27E 0	1.40±0.19E 0	1.50±0.19E 0	2.28±0.28E 0	6.29±0.68E 0	1.20±0.15E 2	2.53±0.40E 0
NGC0059	8.48±0.85E-2	1.13±0.11E-1	6.36±0.64E-2	3.29±0.45E-2	2.23±0.31E-2	1.56±0.20E-2	1.18±0.15E-2	4.40±0.47E-2	5.15±0.63E-1	4.07±0.66E-1
ESO410-G005	<6.18E-2	<9.05E-2	<1.11E-1	1.58±0.21E-2	6.46±0.89E-3	1.12±0.15E-2	6.40±0.81E-3	4.43±0.46E-3	5.98±0.81E-2	2.26±0.31E-1
Sculptor-dE1	<3.66E-2	<5.35E-2	<6.59E-2	<3.40E-4	<5.10E-4	<1.88E-3	<2.06E-3	<3.42E-3	<4.63E-2	<1.75E-1
ESO294-G010	1.73±0.17E-2	2.12±0.21E-2	1.35±0.14E-2	4.79±0.65E-3	3.12±0.43E-3	<1.89E-3	<2.06E-3	<3.44E-3	<4.64E-2	<1.75E-1
IC1574	1.96±0.20E-2	2.18±0.22E-2	1.55±0.16E-2	5.93±0.80E-3	3.94±0.54E-3	2.62±0.36E-3	1.73±0.24E-3	<1.22E-3	<5.65E-2	<2.13E-1
NGC0247	1.47±0.15E 0	1.30±0.13E 0	1.02±0.10E 0	8.54±1.15E-1	5.89±0.81E-1	6.12±0.77E-1	8.48±1.06E-1	9.89±1.06E-1	1.57±0.19E 1	6.88±1.07E 1
NGC0253 <sup>e</sup>	2.11±0.21E 1	2.53±0.25E 1	2.23±0.22E 1	1.23±0.17E 1	8.25±1.13E 0	1.94±0.24E 1	3.86±0.48E 1	8.00±0.86E 1	1.18±0.14E 3	1.87±0.29E 3
ESO540-G030	<5.54E-2	<8.08E-2	<9.94E-2	2.17±0.29E-3	1.58±0.22E-3	<1.66E-3	<1.81E-3	<3.42E-3	<4.07E-2	<1.53E-1
UGCA015	6.42±0.64E-3	9.01±0.90E-3	4.27±0.43E-3	2.11±0.29E-3	1.67±0.23E-3	1.58±0.18E-3	1.73±0.19E-3	<2.87E-3	<3.86E-2	<1.47E-1
ESO540-G032	4.75±0.48E-3	1.15±0.12E-2	<3.64E-2	1.46±0.20E-3	7.60±1.10E-4	<7.00E-4	<7.60E-4	<2.54E-3	<3.43E-2	<1.30E-1
UGC00521	8.60±0.86E-3	9.60±0.96E-3	5.42±0.54E-3	3.01±0.41E-3	2.24±0.31E-3	1.04±0.14E-3	1.16±0.15E-3	...	...	...
SMC <sup>a e f</sup>	...	...	...	...	...	...	...	3.51±0.52E 2	1.25±0.26E 4	1.90±0.49E 4
NGC0300	3.26±0.33E 0	3.27±0.33E 0	2.52±0.25E 0	1.63±0.22E 0	1.20±0.16E 0	1.25±0.16E 0	2.02±0.25E 0	2.50±0.27E 0	4.61±0.56E 1	1.62±0.25E 1
UGC00668 <sup>e f</sup>	3.05±0.30E-1	4.74±0.47E-1	2.32±0.23E-1	1.24±0.17E-1	9.09±1.25E-2	3.34±0.42E-2	7.13±0.89E-2	8.63±0.93E-2	2.46±0.30E 0	5.99±0.94E 0
UGC00685	4.20±0.42E-2	2.28±0.23E-2	<1.04E-1	1.14±0.16E-2	7.47±1.03E-3	4.27±0.57E-3	5.28±0.67E-3	...	...	...
UGC00695	9.45±0.95E-3	9.99±1.00E-3	<5.51E-2	4.46±0.61E-3	3.01±0.41E-3	1.84±0.25E-3	1.47±0.20E-3	...	...	...
NGC0404 <sup>e</sup>	8.10±0.81E-1	8.41±0.84E-1	6.76±0.68E-1	4.72±0.64E-1	2.53±0.35E-1	2.29±0.30E-1	1.57±0.20E-1	1.46±0.16E-1	2.84±0.35E 0	3.52±0.55E 0
UGC00891	2.43±0.24E-2	1.34±0.13E-2	1.55±0.16E-2	6.11±0.83E-3	4.19±0.58E-3	1.83±0.26E-3	3.69±0.47E-3	...	...	...
UGC01056	1.77±0.18E-2	2.60±0.26E-2	2.91±0.29E-2	5.59±0.76E-3	4.14±0.57E-3	2.60±0.35E-3	4.22±0.54E-3	...	...	...
UGC01104	2.02±0.20E-2	2.11±0.21E-2	1.58±0.16E-2	8.45±1.15E-3	5.70±0.78E-3	3.44±0.46E-3	5.01±0.64E-3	...	...	...
NGC0598 <sup>e f</sup>	2.12±0.21E 1	2.12±0.21E 1	1.67±0.17E 1	1.97±0.27E 1	1.39±0.19E 1	1.29±0.16E 1	2.78±0.35E 1	4.81±0.52E 1	7.81±0.95E 2	2.32±0.36E 2
NGC0625	2.83±0.28E-1	2.97±0.30E-1	2.42±0.24E-1	1.23±0.17E-1	8.83±1.21E-2	9.22±1.17E-2	1.37±0.17E-1	8.79±0.95E-1	6.49±0.79E 0	8.52±1.33E 0
NGC0628 <sup>e f</sup>	1.66±0.17E 0	1.67±0.17E 0	1.32±0.13E 0	8.72±1.18E-1	5.45±0.75E-1	1.15±0.15E 0	2.70±0.34E 0	3.13±0.13E 0	3.38±0.25E 1	1.19±0.15E 1
UGC01176	<7.90E-2	<1.10E-1	<1.35E-1	8.28±1.12E-3	6.22±0.85E-3	4.43±0.59E-3	4.37±0.56E-3	...	...	...
ESO245-G005	5.02±0.50E-2	5.90±0.59E-2	4.14±0.41E-2	2.18±0.30E-2	1.53±0.21E-2	1.81±0.23E-2	7.77±0.98E-3	2.47±0.27E-2	5.95±0.74E-1	1.08±0.17E-1
UGC01249	1.05±0.11E-1	1.73±0.17E-1	8.91±0.89E-2	6.19±0.84E-2	3.86±0.53E-2	3.79±0.48E-2	1.94±0.24E-2	9.50±1.03E-2	1.87±0.23E 0	4.25±0.66E 0
NGC0672	3.59±0.36E-1	3.66±0.37E-1	2.96±0.30E-1	1.52±0.21E-1	1.18±0.16E-1	1.16±0.15E-1	1.16±0.14E-1	3.38±0.36E-1	5.90±0.72E 0	1.50±0.23E 0
ESO245-G007 <sup>f</sup>	4.34±0.43E-2	3.61±0.36E-2	<5.00E-2	1.72±0.23E-2	1.25±0.17E-2	<4.32E-3	<5.45E-3	<6.98E-3	<9.41E-2	<3.55E-1
NGC0784	1.03±0.10E-1	1.02±0.10E-1	7.22±0.72E-2	4.98±0.67E-2	3.50±0.48E-2	2.69±0.34E-2	1.52±0.19E-2	4.94±0.53E-2	1.15±0.14E 0	1.92±0.30E 0

Table 2—Continued

Galaxy	2MASS J 1.25 $\mu\text{m}$ (Jy)	2MASS H 1.65 $\mu\text{m}$ (Jy)	2MASS K <sub>s</sub> 2.17 $\mu\text{m}$ (Jy)	IRAC 3.6 $\mu\text{m}$ (Jy)	IRAC 4.5 $\mu\text{m}$ (Jy)	IRAC 5.8 $\mu\text{m}$ (Jy)	IRAC 8.0 $\mu\text{m}$ (Jy)	MIPS 24 $\mu\text{m}$ (Jy)	MIPS 70 $\mu\text{m}$ (Jy)	MIPS 160 $\mu\text{m}$ (Jy)
NGC0855 <sup>e f</sup>	9.07±0.91E-2	9.78±0.98E-2	7.97±0.80E-2	4.24±0.60E-2	2.75±0.39E-2	1.83±0.30E-2	4.57±0.57E-2	8.65±0.42E-2	1.64±0.14E 0	2.29±0.30E-1
ESO115-G021	5.85±0.58E-2	6.67±0.67E-2	4.17±0.42E-2	1.87±0.25E-2	1.24±0.17E-2	8.90±1.16E-3	7.73±0.97E-3	1.71±0.19E-2	3.85±0.48E-1	7.04±1.15E-1
ESO154-G023	1.32±0.13E-1	1.41±0.14E-1	1.05±0.10E-1	3.76±0.51E-2	3.08±0.42E-2	1.59±0.20E-2	1.86±0.23E-2	4.99±0.54E-2	1.03±0.13E 0	1.84±0.25E-1
NGC1291 <sup>e f</sup>	4.37±0.44E 0	4.56±0.46E 0	3.98±0.40E 0	2.11±0.28E 0	1.27±0.18E 0	9.47±1.22E-1	6.35±0.80E-1	5.60±0.24E-1	6.17±0.46E 0	2.76±0.30E-1
NGC1313	9.81±0.98E-1	1.04±0.10E 0	7.41±0.74E-1	6.43±0.87E-1	4.87±0.67E-1	6.18±0.77E-1	1.22±0.15E 0	2.85±0.31E 0	5.15±0.63E 1	9.62±1.50E-1
NGC1311	5.13±0.51E-2	5.25±0.52E-2	4.08±0.41E-2	2.37±0.32E-2	1.68±0.23E-2	1.27±0.16E-2	1.23±0.16E-2	2.90±0.31E-2	7.20±0.88E-1	1.16±0.18E-1
UGC02716	2.53±0.25E-2	2.56±0.26E-2	2.22±0.22E-2	1.20±0.16E-2	7.58±1.04E-3	7.23±0.95E-3	8.67±1.09E-3	8.68±0.96E-3	1.56±0.20E-1	1.48±0.20E-1
IC1959	3.45±0.34E-2	3.54±0.35E-2	2.77±0.28E-2	1.91±0.26E-2	1.31±0.18E-2	9.81±1.28E-3	1.00±0.13E-2	3.24±0.35E-2	8.99±1.10E-1	1.08±0.17E-1
NGC1487	1.32±0.13E-1	1.78±0.18E-1	1.20±0.12E-1	7.10±0.96E-2	4.61±0.63E-2	7.63±0.98E-2	1.37±0.17E-1	2.94±0.32E-1	4.68±0.57E 0	7.60±1.19E-1
NGC1510	3.77±0.38E-2	3.71±0.37E-2	3.09±0.31E-2	1.71±0.23E-2	1.19±0.16E-2	1.41±0.19E-2	2.20±0.28E-2	1.35±0.15E-1	9.19±1.12E-1	6.08±0.90E-1
NGC1512 <sup>e f</sup>	8.12±0.81E-1	8.57±0.86E-1	7.30±0.73E-1	3.88±0.53E-1	2.43±0.34E-1	2.64±0.34E-1	4.37±0.55E-1	4.38±0.21E-1	6.34±0.48E 0	2.24±0.25E-1
NGC1522	2.61±0.26E-2	2.28±0.23E-2	1.99±0.20E-2	1.10±0.15E-2	7.87±1.08E-3	9.83±1.29E-3	1.51±0.19E-2	9.66±1.04E-2	9.41±1.15E-1	8.03±1.20E-1
IC2049	1.08±0.11E-2	1.26±0.13E-2	8.79±0.88E-3	4.39±0.60E-3	2.83±0.39E-3	1.10±0.16E-3	3.04±0.39E-3	4.70±0.53E-3	6.16±0.88E-2	1.25±0.22E-2
ESO483-G013	3.93±0.39E-2	3.85±0.39E-2	3.37±0.34E-2	1.68±0.23E-2	1.14±0.16E-2	1.22±0.16E-2	1.12±0.14E-2	3.46±0.37E-2	5.40±0.66E-1	4.77±0.70E-1
ESO158-G003	3.84±0.38E-2	3.54±0.35E-2	2.74±0.27E-2	1.64±0.22E-2	1.14±0.16E-2	1.11±0.14E-2	2.04±0.26E-2	2.91±0.31E-2	5.37±0.66E-1	7.02±0.10E-1
ESO119-G016	1.89±0.19E-2	2.21±0.22E-2	1.51±0.15E-2	7.40±1.00E-3	5.37±0.74E-3	2.81±0.38E-3	2.91±0.38E-3	6.11±0.70E-3	7.33±1.11E-2	1.63±0.23E-2
NGC1705 <sup>e f</sup>	5.75±0.57E-2	5.40±0.54E-2	4.44±0.44E-2	2.57±0.36E-2	1.79±0.25E-2	1.01±0.19E-2	1.68±0.20E-2	5.45±0.22E-2	1.26±0.10E 0	1.44±0.21E-1
NGC1744	1.12±0.11E-1	1.13±0.11E-1	8.94±0.89E-2	8.32±1.13E-2	6.44±0.88E-2	4.96±0.63E-2	9.56±1.19E-2	1.10±0.12E-1	1.98±0.24E 0	6.27±0.90E-1
NGC1796	1.02±0.10E-1	1.12±0.11E-1	9.55±0.95E-2	5.51±0.75E-2	3.76±0.52E-2	8.48±1.09E-2	1.91±0.24E-1	2.22±0.24E-1	3.38±0.41E 0	6.86±1.07E-1
ESO486-G021	1.87±0.19E-2	2.07±0.21E-2	1.32±0.13E-2	6.57±0.89E-3	4.25±0.58E-3	4.96±0.66E-3	6.12±0.78E-3	...	...	...
MCG-05-13-004 <sup>b</sup>	...	...	...	...	...	...	...	...	...	...
NGC1800	8.96±0.90E-2	1.03±0.10E-1	8.34±0.83E-2	3.14±0.43E-2	2.08±0.29E-2	2.58±0.33E-2	3.57±0.45E-2	6.02±0.65E-2	1.21±0.15E 0	1.88±0.25E-1
UGCA106	1.19±0.12E-1	6.95±0.69E-2	4.99±0.50E-2	2.69±0.37E-2	1.93±0.26E-2	1.75±0.22E-2	2.51±0.31E-2	5.05±0.55E-2	8.88±1.09E-1	2.36±0.37E-1
LMC <sup>a e f</sup>	...	...	...	2.05±0.29E 3	1.41±0.20E 3	1.77±0.25E 3	4.81±0.75E 3	5.96±0.60E 3	1.11±0.13E 5	2.60±0.40E 5
kkh037	5.43±0.54E-3	6.24±0.62E-3	6.43±0.64E-3	2.50±0.34E-3	1.58±0.22E-3	1.35±0.18E-3	1.48±0.17E-3	2.45±0.20E-3	3.30±0.46E-2	1.25±0.17E-2
NGC2366 <sup>e</sup>	1.45±0.15E-1	1.47±0.15E-1	1.10±0.11E-1	6.43±0.87E-2	4.90±0.67E-2	4.95±0.63E-2	5.50±0.69E-2	6.79±0.73E-1	5.40±0.66E 0	5.05±0.79E-1
UGCA133	1.79±0.18E-2	1.65±0.17E-2	9.06±0.91E-3	4.09±0.55E-3	3.10±0.43E-3	<2.65E-3	<2.89E-3	4.81±0.44E-3	6.48±1.23E-2	2.45±0.30E-2
NGC2403 <sup>e f</sup>	2.94±0.29E 0	2.91±0.29E 0	2.39±0.24E 0	1.88±0.25E 0	1.31±0.18E 0	2.10±0.27E 0	4.11±0.51E 0	5.84±0.24E 0	8.64±0.62E 1	2.41±0.30E-1
NGC2500 <sup>e</sup>	1.71±0.17E-1	1.80±0.18E-1	1.39±0.14E-1	8.76±1.19E-2	5.65±0.77E-2	1.13±0.15E-1	1.69±0.21E-1	2.09±0.23E-1	3.93±0.48E 0	8.80±1.37E-1
NGC2537 <sup>e</sup>	1.93±0.19E-1	1.95±0.19E-1	1.60±0.16E-1	7.72±1.05E-2	5.11±0.70E-2	7.67±0.99E-2	1.41±0.18E-1	2.92±0.31E-1	4.02±0.49E 0	5.70±0.89E-1
UGC04278 <sup>e f</sup>	4.79±0.48E-2	4.52±0.45E-2	3.58±0.36E-2	2.18±0.30E-2	1.57±0.22E-2	1.65±0.22E-2	1.56±0.20E-2	3.80±0.41E-2	8.96±1.10E-1	1.58±0.23E-1
UGC04305 <sup>e f</sup>	1.66±0.17E-1	2.91±0.29E-1	2.16±0.22E-1	7.13±0.98E-2	5.66±0.78E-2	3.05±0.47E-2	2.39±0.48E-2	2.04±0.08E-1	3.60±0.26E 0	4.10±0.50E-1
NGC2552	6.62±0.66E-2	8.70±0.87E-2	5.49±0.55E-2	3.35±0.45E-2	2.27±0.31E-2	2.17±0.28E-2	1.78±0.22E-2	5.77±0.62E-2	9.79±1.20E-1	2.35±0.37E-1



Table 2—Continued

Galaxy	2MASS J 1.25 $\mu\text{m}$ (Jy)	2MASS H 1.65 $\mu\text{m}$ (Jy)	2MASS K <sub>s</sub> 2.17 $\mu\text{m}$ (Jy)	IRAC 3.6 $\mu\text{m}$ (Jy)	IRAC 4.5 $\mu\text{m}$ (Jy)	IRAC 5.8 $\mu\text{m}$ (Jy)	IRAC 8.0 $\mu\text{m}$ (Jy)	MIPS 24 $\mu\text{m}$ (Jy)	MIPS 70 $\mu\text{m}$ (Jy)	MIPS 160 $\mu\text{m}$ (Jy)
M81dwA <sup>e f</sup>	3.77±0.38E-3	3.88±0.39E-3	2.92±0.29E-3	1.86±0.90E-3	9.50±9.00E-4	<3.73E-3	<2.37E-3	<1.73E-2	<1.49E-1	<1.43E-1
UGC04426	1.15±0.12E-2	1.61±0.16E-2	8.91±0.89E-3	4.58±0.62E-3	3.29±0.45E-3	<2.53E-3	3.22±0.42E-3	...	...	...
UGC04459 <sup>e f</sup>	7.54±0.75E-3	1.38±0.14E-2	7.93±0.79E-3	4.71±1.00E-3	3.88±1.00E-3	2.65±0.90E-3	7.32±1.00E-3	2.81±0.11E-2	3.48±0.34E-1	3.41±1.11E-1
UGC04483 <sup>e</sup>	5.95±0.60E-3	7.63±0.76E-3	4.19±0.42E-3	1.84±0.25E-3	9.60±1.30E-4	6.40±1.00E-4	1.13±0.15E-3	7.05±0.77E-3	1.05±0.13E-1	2.01±0.25E-1
NGC2683	2.16±0.22E 0	2.46±0.25E 0	2.10±0.21E 0	1.08±0.15E 0	6.92±0.95E-1	7.49±0.94E-1	1.18±0.15E 0	...	...	...
UGC04704	2.11±0.21E-2	2.76±0.28E-2	2.63±0.26E-2	8.88±1.20E-3	5.81±0.80E-3	6.18±0.81E-3	2.14±0.29E-3	...	...	...
UGC04787	2.59±0.26E-2	2.40±0.24E-2	1.93±0.19E-2	8.55±1.16E-3	5.86±0.81E-3	2.96±0.40E-3	5.29±0.67E-3	...	...	...
UGC04998	2.55±0.26E-2	3.08±0.31E-2	1.77±0.18E-2	1.08±0.15E-2	7.49±1.03E-3	5.72±0.75E-3	6.57±0.83E-3	<4.64E-3	<6.23E-2	<2.36E-1
NGC2903	3.00±0.30E 0	3.14±0.31E 0	2.74±0.27E 0	1.61±0.22E 0	1.09±0.15E 0	2.20±0.28E 0	5.11±0.64E 0	7.00±0.75E 0	7.26±0.89E 1	1.82±0.28E 1
UGC05076	1.62±0.16E-2	1.26±0.13E-2	9.06±0.91E-3	5.02±0.68E-3	3.29±0.45E-3	1.49±0.22E-3	4.59±0.58E-3	...	...	...
CGCG035-007	1.23±0.12E-2	1.41±0.14E-2	1.35±0.14E-2	4.27±0.58E-3	2.89±0.40E-3	1.83±0.25E-3	2.03±0.26E-3	4.46±0.50E-3	1.18±0.15E-1	1.00±0.18E-1
UGC05139 <sup>e f</sup>	3.09±0.31E-2	3.97±0.40E-2	1.60±0.16E-2	1.19±0.14E-2	7.55±1.20E-3	7.31±1.80E-3	7.54±1.60E-3	1.31±0.20E-2	4.02±0.79E-1	7.97±1.70E-1
IC0559	1.92±0.19E-2	1.72±0.17E-2	2.37±0.24E-2	8.10±1.10E-3	5.56±0.76E-3	5.24±0.69E-3	2.35±0.30E-3	5.01±0.57E-3	9.31±1.26E-2	1.49±0.26E-1
F8D1	2.96±0.30E-2	7.01±0.70E-2	1.88±0.19E-2	1.08±0.15E-2	8.75±1.20E-3	<5.59E-3	<6.15E-3	<6.78E-3	<9.11E-2	<3.44E-1
[FM2000]1	<1.85E-2	<2.56E-2	<3.14E-2	<3.60E-4	<5.30E-4	<1.95E-3	<2.13E-3	<2.36E-3	<3.18E-2	<1.20E-1
NGC2976 <sup>e f</sup>	8.60±0.86E-1	8.93±0.89E-1	7.07±0.71E-1	4.34±0.59E-1	2.84±0.39E-1	5.04±0.65E-1	1.02±0.13E 0	1.38±0.06E 0	1.99±0.14E 1	4.83±0.64E 1
LEDA166101	<8.21E-2	<1.12E-1	<1.35E-1	6.13±0.83E-3	4.10±0.56E-3	<2.68E-3	<2.94E-3	<4.87E-3	<6.53E-2	<2.46E-1
UGC05272	1.99±0.20E-2	2.57±0.26E-2	1.58±0.16E-2	7.36±1.00E-3	5.12±0.70E-3	3.78±0.50E-3	1.84±0.24E-3	1.31±0.14E-2	3.09±0.38E-1	3.09±0.50E-1
UGC05288	2.91±0.29E-2	2.34±0.23E-2	2.44±0.24E-2	8.50±1.15E-3	5.69±0.78E-3	4.95±0.65E-3	3.13±0.40E-3	1.12±0.12E-2	1.79±0.23E-1	4.27±0.68E-1
BK03N	<3.81E-3	<5.29E-3	<6.48E-3	<1.70E-4	<2.50E-4	<9.10E-4	<1.00E-3	<1.10E-3	<1.48E-2	<5.61E-2
NGC3031 <sup>e f</sup>	2.35±0.24E 1	2.55±0.25E 1	2.13±0.21E 1	1.09±0.15E 1	6.53±0.90E 0	5.88±0.75E 0	8.04±1.00E 0	5.09±0.20E 0	8.52±0.60E 1	3.56±0.43E 1
NGC3034 <sup>c e f</sup>	9.29±0.93E 0	1.08±0.11E 1	1.01±0.10E 1	7.51±1.02E 0	5.93±0.81E 0	2.45±0.31E 1	6.42±0.80E 1	>8.72E 1	>1.29E 3	>8.58E 3
UGC05340 <sup>e</sup>	8.67±0.87E-3	7.35±0.73E-3	<8.58E-3	2.54±0.35E-3	1.61±0.22E-3	<1.41E-3	<1.54E-3	<2.60E-3	<3.51E-2	<1.32E-1
KDG061	9.81±0.98E-3	7.28±0.73E-3	1.18±0.12E-2	4.66±0.63E-3	2.89±0.40E-3	<2.33E-3	<2.56E-3	<4.25E-3	<7.05E-2	<2.66E-1
UGC05336	2.47±0.25E-2	2.05±0.20E-2	1.47±0.15E-2	7.38±1.10E-3	3.79±1.00E-3	<1.30E-2	<1.20E-2	<3.64E-2	<2.28E-1	<4.58E-1
ArpsLoop	<4.43E-2	<6.12E-2	<7.51E-2	<3.70E-4	<5.50E-4	<2.01E-3	<2.20E-3	<3.66E-3	<4.91E-2	<1.85E-1
UGC05364 <sup>f</sup>	<1.35E-1	<1.90E-1	<2.36E-1	1.95±0.26E-2	1.36±0.19E-2	<7.13E-3	<7.77E-3	<6.49E-3	<8.75E-2	<3.30E-1
UGC05373 <sup>f</sup>	1.22±0.12E-1	1.32±0.13E-1	1.36±0.14E-1	4.97±0.67E-2	3.61±0.50E-2	1.51±0.19E-2	1.55±0.19E-2	2.10±0.23E-2	1.21±0.19E-1	1.88±0.39E-1
kkh057	<8.50E-3	<1.20E-2	<1.49E-2	6.00±0.80E-4	2.20±0.30E-4	<4.60E-4	<5.00E-4	<1.65E-3	<2.23E-2	<8.30E-2
UGCA193	1.58±0.16E-2	1.21±0.12E-2	1.91±0.19E-2	5.72±0.78E-3	3.83±0.53E-3	2.75±0.37E-3	2.35±0.31E-3	3.64±0.44E-3	4.08±0.76E-2	6.20±1.55E-2
NGC3109	5.77±0.58E-1	3.56±0.36E-1	3.44±0.34E-1	2.34±0.32E-1	1.73±0.24E-1	1.10±0.14E-1	1.20±0.15E-1	2.56±0.28E-1	6.75±0.82E 0	1.21±0.19E 1
NGC3077 <sup>f</sup>	1.05±0.11E 0	1.04±0.10E 0	8.70±0.87E-1	5.54±0.75E-1	3.75±0.51E-1	4.34±0.55E-1	8.11±1.01E-1	...	...	...
AM1001-270 <sup>f</sup>	<8.51E-3	<1.22E-2	<1.48E-2	3.26±0.44E-3	2.25±0.31E-3	2.80±0.29E-3	3.08±0.33E-3	3.41±0.30E-3	4.58±0.74E-2	1.73±0.25E-1

Table 2—Continued

Galaxy	2MASS J 1.25 $\mu\text{m}$ (Jy)	2MASS H 1.65 $\mu\text{m}$ (Jy)	2MASS K <sub>s</sub> 2.17 $\mu\text{m}$ (Jy)	IRAC 3.6 $\mu\text{m}$ (Jy)	IRAC 4.5 $\mu\text{m}$ (Jy)	IRAC 5.8 $\mu\text{m}$ (Jy)	IRAC 8.0 $\mu\text{m}$ (Jy)	MIPS 24 $\mu\text{m}$ (Jy)	MIPS 70 $\mu\text{m}$ (Jy)	MIPS 160 $\mu\text{m}$ (Jy)
BK05N	<4.85E-2	<6.74E-2	<8.30E-2	1.69±0.23E-3	7.90±1.10E-4	<1.06E-3	<1.17E-3	<3.86E-3	<5.20E-2	<1.96E-1
UGC05428	1.41±0.14E-2	1.28±0.13E-2	1.03±0.10E-2	4.22±0.57E-3	2.63±0.36E-3	<2.42E-3	<2.64E-3	<4.85E-3	<6.51E-2	<2.46E-1
UGC05423 <sup>e f</sup>	1.20±0.12E-2	1.37±0.14E-2	1.36±0.14E-2	4.86±1.00E-3	3.43±1.00E-3	2.65±0.90E-3	2.52±0.80E-3	8.30±1.20E-3	1.40±0.34E-1	2.55±1.79E-1
UGC05442	1.51±0.15E-2	1.46±0.15E-2	1.33±0.13E-2	5.09±0.69E-3	3.55±0.49E-3	1.51±0.22E-3	3.11±0.40E-3	2.60±2.20E-4	<5.60E-2	<2.11E-1
UGC05456	3.80±0.38E-2	5.01±0.50E-2	3.10±0.31E-2	1.33±0.18E-2	9.09±1.25E-3	8.98±1.18E-3	1.04±0.13E-2	5.67±0.61E-2	6.28±0.77E-1	6.88±1.08E-1
IKN	<6.58E-2	<9.17E-2	<1.13E-1	<2.20E-4	<3.30E-4	<1.22E-3	<1.34E-3	<4.45E-3	<6.00E-2	<2.27E-1
SextansA <sup>e f</sup>	<1.69E-1	<2.44E-1	<2.98E-1	3.24±0.44E-2	2.18±0.30E-2	2.66±0.34E-2	1.77±0.22E-2	3.05±0.33E-2	7.05±0.87E-1	9.76±1.55E-1
[HS98]117	5.42±0.54E-3	6.82±0.68E-3	9.03±0.90E-3	2.87±0.39E-3	1.57±0.22E-3	<1.22E-3	<1.33E-3	<4.42E-3	<5.93E-2	<2.24E-1
NGC3239	1.60±0.16E-1	1.72±0.17E-1	1.25±0.12E-1	7.42±1.00E-2	4.97±0.68E-2	7.47±0.96E-2	8.72±1.09E-2	3.58±0.39E-1	4.95±0.60E 0	7.40±1.16E 0
DDO078	<4.45E-2	<6.27E-2	<7.79E-2	<1.90E-4	<2.80E-4	<1.03E-3	<1.12E-3	<3.74E-3	<5.04E-2	<1.91E-1
UGC05672	4.06±0.41E-2	3.45±0.34E-2	2.53±0.25E-2	1.19±0.16E-2	7.71±1.06E-3	7.16±0.94E-3	6.96±0.88E-3	8.49±0.95E-3	7.49±1.16E-2	3.93±0.63E-1
UGC05666 <sup>e f</sup>	3.36±0.34E-1	2.31±0.23E-1	1.65±0.16E-1	1.51±0.21E-1	9.05±1.27E-2	6.48±0.87E-2	6.63±0.89E-2	2.74±0.13E-1	5.19±0.43E 0	1.05±0.15E 0
UGC05692	9.28±0.93E-2	8.24±0.82E-2	6.64±0.66E-2	2.69±0.36E-2	1.77±0.24E-2	1.66±0.21E-2	1.12±0.14E-2	1.12±0.13E-2	2.98±0.38E-1	6.14±0.98E-1
NGC3274	4.24±0.42E-2	4.15±0.41E-2	3.59±0.36E-2	2.02±0.27E-2	1.35±0.19E-2	1.73±0.22E-2	2.24±0.28E-2	6.23±0.67E-2	1.25±0.15E 0	1.61±0.25E 0
BK06N	8.54±0.85E-3	<1.16E-2	<1.23E-2	2.06±0.28E-3	1.50±0.21E-3	<1.15E-3	<1.26E-3	<4.19E-3	<5.66E-2	<2.14E-1
NGC3299	8.22±0.82E-2	7.11±0.71E-2	6.80±0.68E-2	2.99±0.40E-2	2.04±0.28E-2	1.83±0.24E-2	2.83±0.35E-2	2.48±0.27E-2	3.03±0.38E-1	1.03±0.16E 0
UGC05764	6.61±0.66E-3	6.87±0.69E-3	7.29±0.73E-3	2.66±0.36E-3	1.89±0.26E-3	1.25±0.18E-3	1.02±0.14E-3	3.45±0.40E-3	6.03±0.87E-2	8.71±1.67E-1
UGC05797	1.91±0.19E-2	1.48±0.15E-2	1.17±0.12E-2	6.48±0.88E-3	4.08±0.56E-3	3.74±0.50E-3	3.01±0.39E-3	4.29±0.50E-3	1.11±0.15E-1	2.27±0.37E-1
UGC05829	5.48±0.55E-2	3.74±0.37E-2	2.22±0.22E-2	1.36±0.18E-2	9.20±1.26E-3	5.90±0.77E-3	6.46±0.82E-3	3.16±0.34E-2	7.17±0.88E-1	9.06±1.43E-1
NGC3344 <sup>e</sup>	9.42±0.94E-1	8.91±0.89E-1	6.94±0.69E-1	4.01±0.54E-1	2.49±0.34E-1	4.74±0.60E-1	9.74±1.21E-1	1.18±0.13E 0	1.51±0.18E 1	5.12±0.80E 1
NGC3351 <sup>e f</sup>	1.68±0.17E 0	1.77±0.18E 0	1.54±0.15E 0	8.13±1.10E-1	5.14±0.71E-1	7.20±0.93E-1	1.34±0.16E 0	2.49±0.12E 0	2.29±0.19E 1	6.11±0.83E 1
NGC3368 <sup>e</sup>	2.29±0.23E 0	2.52±0.25E 0	2.11±0.21E 0	1.09±0.15E 0	6.65±0.91E-1	6.84±0.87E-1	8.86±1.10E-1	7.82±0.84E-1	1.41±0.17E 1	4.77±0.75E 1
UGC05889	3.39±0.34E-2	3.91±0.39E-2	3.03±0.30E-2	1.34±0.18E-2	8.66±1.19E-3	6.37±0.83E-3	4.35±0.56E-3	8.05±0.91E-3	<7.03E-2	<2.66E-1
UGC05923 <sup>e</sup>	2.63±0.26E-2	2.92±0.29E-2	2.18±0.22E-2	9.64±1.31E-3	6.38±0.88E-3	6.03±0.80E-3	9.36±1.19E-3	1.09±0.12E-2	2.46±0.30E-1	2.33±0.37E-1
UGC05918	<3.53E-2	<4.00E-2	<4.97E-2	3.00±0.41E-3	2.00±0.28E-3	<1.83E-3	<2.00E-3	<3.33E-3	<4.50E-2	<1.70E-1
NGC3432	2.03±0.20E-1	2.10±0.21E-1	1.71±0.17E-1	1.02±0.14E-1	7.38±1.01E-2	1.36±0.17E-1	2.29±0.29E-1	5.99±0.65E-1	9.67±1.18E 0	1.85±0.29E 0
KDG073	<2.85E-2	<4.02E-2	<5.00E-2	1.94±0.26E-3	6.10±0.80E-4	<8.20E-4	<9.00E-4	<2.98E-3	<4.03E-2	<1.52E-1
NGC3486 <sup>e</sup>	4.80±0.48E-1	5.82±0.58E-1	4.47±0.45E-1	2.36±0.32E-1	1.58±0.22E-1	2.60±0.33E-1	5.88±0.73E-1	6.41±0.69E-1	9.65±1.18E 0	2.70±0.42E 0
NGC3510	5.82±0.58E-2	3.81±0.38E-2	2.32±0.23E-2	2.07±0.28E-2	1.45±0.20E-2	1.52±0.20E-2	2.31±0.29E-2	5.34±0.58E-2	1.18±0.14E 0	1.82±0.28E 0
NGC3521 <sup>e f</sup>	3.74±0.37E 0	4.22±0.42E 0	3.50±0.35E 0	2.05±0.28E 0	1.36±0.19E 0	2.53±0.32E 0	6.27±0.76E 0	5.51±0.22E 0	6.26±0.45E 1	2.12±0.27E 1
NGC3593 <sup>e</sup>	7.76±0.78E-1	9.45±0.94E-1	7.66±0.77E-1	3.75±0.51E-1	2.51±0.34E-1	5.26±0.67E-1	1.21±0.15E 0	1.69±0.18E 0	2.22±0.27E 1	3.31±0.52E 1
NGC3623	2.89±0.29E 0	3.20±0.32E 0	2.65±0.27E 0	1.27±0.17E 0	7.95±1.09E-1	7.43±0.94E-1	7.67±0.96E-1	5.55±0.60E-1	7.01±0.86E 0	3.57±0.56E 0
NGC3627 <sup>e f</sup>	3.34±0.33E 0	3.73±0.37E 0	3.17±0.32E 0	1.87±0.25E 0	1.25±0.17E 0	2.35±0.30E 0	5.58±0.69E 0	7.43±0.30E 0	9.22±0.70E 1	2.20±0.28E 1

Table 2—Continued

Galaxy	2MASS J 1.25 $\mu\text{m}$ (Jy)	2MASS H 1.65 $\mu\text{m}$ (Jy)	2MASS K <sub>s</sub> 2.17 $\mu\text{m}$ (Jy)	IRAC 3.6 $\mu\text{m}$ (Jy)	IRAC 4.5 $\mu\text{m}$ (Jy)	IRAC 5.8 $\mu\text{m}$ (Jy)	IRAC 8.0 $\mu\text{m}$ (Jy)	MIPS 24 $\mu\text{m}$ (Jy)	MIPS 70 $\mu\text{m}$ (Jy)	MIPS 160 $\mu\text{m}$ (Jy)
NGC3628	2.43±0.24E 0	2.98±0.30E 0	2.66±0.27E 0	1.52±0.21E 0	1.04±0.14E 0	1.86±0.23E 0	4.08±0.51E 0	5.10±0.55E 0	6.26±0.76E 1	1.90±0.3
UGC06457	1.52±0.15E-2	1.65±0.17E-2	1.18±0.12E-2	5.52±0.75E-3	3.13±0.43E-3	2.92±0.39E-3	2.31±0.30E-3	2.07±0.29E-3	1.09±0.14E-1	1.39±0.2
UGC06541 <sup>e</sup>	1.13±0.11E-2	1.26±0.13E-2	1.26±0.13E-2	5.28±0.72E-3	3.88±0.53E-3	1.98±0.27E-3	2.29±0.30E-3	6.57±0.72E-3	1.95±0.24E-1	7.30±1.4
NGC3738 <sup>e</sup>	1.32±0.13E-1	1.40±0.14E-1	1.04±0.10E-1	6.03±0.82E-2	4.02±0.55E-2	4.22±0.55E-2	5.09±0.64E-2	1.24±0.13E-1	2.71±0.33E 0	3.21±0.5
NGC3741	1.13±0.11E-2	1.83±0.18E-2	1.12±0.11E-2	4.61±0.63E-3	3.19±0.44E-3	2.20±0.30E-3	1.16±0.16E-3	5.71±0.64E-3	1.75±0.22E-1	1.20±0.2
UGC06782	<3.29E-2	<4.63E-2	<5.74E-2	2.76±0.38E-3	1.90±0.26E-3	1.46±0.17E-3	1.58±0.25E-3	2.64±0.18E-3	3.57±0.49E-2	1.35±0.1
UGC06817	2.33±0.23E-2	2.62±0.26E-2	2.15±0.22E-2	9.23±1.25E-3	5.51±0.76E-3	4.28±0.57E-3	2.21±0.30E-3	7.25±0.83E-3	1.33±0.18E-1	2.28±0.4
UGC06900	2.38±0.24E-2	1.82±0.18E-2	1.81±0.18E-2	7.68±1.04E-3	5.39±0.74E-3	5.47±0.72E-3	4.25±0.54E-3	4.13±0.51E-3	<6.16E-2	<2.3
NGC4020	6.58±0.66E-2	5.44±0.54E-2	5.91±0.59E-2	3.12±0.42E-2	2.04±0.28E-2	3.40±0.44E-2	6.82±0.86E-2	9.39±1.01E-2	1.25±0.15E 0	3.66±0.5
NGC4068	5.05±0.50E-2	4.16±0.42E-2	3.72±0.37E-2	2.42±0.33E-2	1.69±0.23E-2	1.20±0.16E-2	9.10±1.15E-3	3.22±0.35E-2	7.02±0.86E-1	9.26±1.4
NGC4080	5.25±0.52E-2	5.12±0.51E-2	3.45±0.34E-2	1.85±0.25E-2	1.21±0.17E-2	1.77±0.23E-2	3.94±0.50E-2	3.47±0.38E-2	4.34±0.53E-1	1.46±0.2
NGC4096	5.58±0.56E-1	6.22±0.62E-1	5.35±0.54E-1	2.91±0.39E-1	2.00±0.27E-1	3.91±0.50E-1	8.77±1.09E-1	8.74±0.94E-1	1.09±0.13E 1	4.08±0.6
NGC4144 <sup>e</sup>	1.60±0.16E-1	1.55±0.16E-1	1.24±0.12E-1	7.01±0.95E-2	4.81±0.66E-2	4.45±0.57E-2	6.14±0.77E-2	1.13±0.12E-1	2.37±0.29E 0	5.12±0.8
NGC4163	5.98±0.60E-2	4.39±0.44E-2	3.26±0.33E-2	1.73±0.23E-2	1.15±0.16E-2	7.26±0.95E-3	5.64±0.71E-3	1.24±0.14E-2	1.78±0.23E-1	2.38±0.4
NGC4190	5.96±0.60E-2	4.99±0.50E-2	3.69±0.37E-2	1.83±0.25E-2	1.20±0.16E-2	9.91±1.29E-3	5.83±0.74E-3	1.78±0.19E-2	5.65±0.69E-1	7.94±1.1
ESO321-G014	1.18±0.12E-2	9.34±0.93E-3	<7.33E-2	5.08±0.69E-3	3.52±0.48E-3	9.10±1.50E-4	1.17±0.17E-3	4.00±1.90E-4	<4.79E-2	<1.8
UGC07242	<2.97E-2	<4.19E-2	<4.96E-2	<1.50E-4	<2.30E-4	<8.50E-4	<9.20E-4	<3.07E-3	<4.15E-2	<1.5
UGCA276	1.24±0.12E-2	7.66±0.77E-3	4.49±0.45E-3	2.69±0.36E-3	1.52±0.21E-3	<1.10E-3	<1.21E-3	<4.02E-3	<5.42E-2	<2.0
UGC07267	2.50±0.25E-2	1.98±0.20E-2	1.75±0.18E-2	7.27±0.99E-3	4.82±0.66E-3	2.65±0.36E-3	1.73±0.23E-3	3.57±0.43E-3	6.92±1.02E-2	1.80±0.3
NGC4214 <sup>e</sup>	5.86±0.59E-1	6.39±0.64E-1	4.88±0.49E-1	3.11±0.42E-1	2.14±0.29E-1	3.27±0.41E-1	5.43±0.68E-1	2.00±0.22E 0	2.20±0.27E 1	3.79±0.5
CGCG269-049 <sup>e f</sup>	4.91±0.49E-3	6.62±0.66E-3	3.31±0.33E-3	1.49±0.20E-3	1.16±0.16E-3	6.30±1.00E-4	6.20±0.90E-4	2.87±0.33E-3	4.63±0.65E-2	<1.0
NGC4236 <sup>e f</sup>	6.35±0.63E-1	8.31±0.83E-1	5.70±0.57E-1	2.50±0.34E-1	2.10±0.29E-1	1.07±0.14E-1	2.16±0.27E-1	5.47±0.22E-1	8.18±0.59E 0	1.96±0.2
NGC4244 <sup>e f</sup>	6.73±0.67E-1	6.86±0.69E-1	5.78±0.58E-1	3.05±0.41E-1	2.10±0.29E-1	2.08±0.26E-1	2.87±0.36E-1	4.58±0.49E-1	7.44±0.91E 0	2.35±0.3
NGC4242 <sup>e</sup>	1.94±0.19E-1	2.40±0.24E-1	1.60±0.16E-1	1.03±0.14E-1	6.15±0.84E-2	6.34±0.81E-2	9.90±1.23E-2	1.07±0.12E-1	1.98±0.24E 0	7.00±1.0
UGC07321 <sup>e f</sup>	4.37±0.44E-2	4.75±0.47E-2	3.86±0.39E-2	2.28±0.31E-2	1.46±0.20E-2	1.71±0.22E-2	2.37±0.30E-2	2.98±0.32E-2	5.87±0.72E-1	1.99±0.3
NGC4248	8.41±0.84E-2	7.31±0.73E-2	6.94±0.69E-2	4.13±0.56E-2	2.50±0.34E-2	2.43±0.31E-2	3.09±0.39E-2	3.43±0.37E-2	4.95±0.61E-1	1.28±0.2
NGC4258 <sup>e</sup>	5.03±0.50E 0	5.50±0.55E 0	4.63±0.46E 0	2.28±0.31E 0	1.50±0.21E 0	1.18±0.15E 0	2.52±0.31E 0	2.77±0.30E 0	3.95±0.48E 1	1.40±0.2
ISZ399	3.54±0.35E-2	3.99±0.40E-2	3.45±0.34E-2	2.26±0.31E-2	1.60±0.22E-2	4.91±0.65E-2	1.22±0.15E-1	4.36±0.47E-1	2.92±0.36E 0	2.22±0.3
NGC4288	5.35±0.54E-2	6.46±0.65E-2	3.25±0.33E-2	2.38±0.32E-2	1.53±0.21E-2	2.28±0.30E-2	4.15±0.52E-2	6.80±0.73E-2	1.37±0.17E 0	2.71±0.4
UGC07408	4.48±0.45E-2	3.67±0.37E-2	3.29±0.33E-2	1.31±0.18E-2	7.74±1.06E-3	6.22±0.81E-3	5.04±0.64E-3	<5.46E-3	<7.36E-2	<1.2
UGC07490	7.21±0.72E-2	8.07±0.81E-2	6.83±0.68E-2	2.48±0.34E-2	1.68±0.23E-2	1.57±0.20E-2	1.88±0.23E-2	2.24±0.24E-2	3.86±0.48E-1	1.39±0.2
NGC4395	4.68±0.47E-1	4.45±0.44E-1	3.20±0.32E-1	3.20±0.43E-1	2.54±0.35E-1	2.49±0.31E-1	2.59±0.32E-1	5.09±0.55E-1	1.06±0.13E 1	2.73±0.4
UGCA281 <sup>f</sup>	7.42±0.74E-3	8.22±0.82E-3	7.28±0.73E-3	3.64±0.50E-3	2.64±0.36E-3	1.79±0.25E-3	1.77±0.23E-3	6.12±0.66E-2	4.47±0.55E-1	1.73±0.2

Table 2—Continued

Galaxy	2MASS J 1.25 $\mu\text{m}$ (Jy)	2MASS H 1.65 $\mu\text{m}$ (Jy)	2MASS K <sub>s</sub> 2.17 $\mu\text{m}$ (Jy)	IRAC 3.6 $\mu\text{m}$ (Jy)	IRAC 4.5 $\mu\text{m}$ (Jy)	IRAC 5.8 $\mu\text{m}$ (Jy)	IRAC 8.0 $\mu\text{m}$ (Jy)	MIPS 24 $\mu\text{m}$ (Jy)	MIPS 70 $\mu\text{m}$ (Jy)	MIPS 160 $\mu\text{m}$ (Jy)
UGC07559	1.50±0.15E-2	1.50±0.15E-2	1.12±0.11E-2	5.95±0.81E-3	3.78±0.52E-3	2.13±0.29E-3	1.83±0.24E-3	6.45±0.72E-3	1.51±0.19E-1	1.74±0.29E-
UGC07577	7.76±0.78E-2	7.78±0.78E-2	4.19±0.42E-2	2.60±0.35E-2	1.48±0.20E-2	7.79±1.01E-3	4.08±0.53E-3	7.97±0.93E-3	1.01±0.16E-1	4.69±0.77E-
NGC4449 <sup>e</sup>	1.03±0.10E 0	1.11±0.11E 0	8.93±0.89E-1	4.81±0.65E-1	3.14±0.43E-1	6.32±0.80E-1	1.35±0.17E 0	3.21±0.35E 0	4.49±0.55E 1	8.43±1.32E
UGC07599	6.60±0.66E-3	9.16±0.92E-3	4.01±0.40E-3	2.71±0.37E-3	1.49±0.21E-3	2.35±0.24E-3	2.56±0.26E-3	2.13±0.15E-3	2.88±0.40E-2	1.09±0.15E-
UGC07605	1.39±0.14E-2	1.11±0.11E-2	6.09±0.61E-3	4.31±0.59E-3	2.41±0.33E-3	1.61±0.19E-3	1.76±0.20E-3	1.63±0.23E-3	5.60±0.82E-2	1.49±0.21E-
NGC4455	5.22±0.52E-2	5.47±0.55E-2	4.28±0.43E-2	2.17±0.30E-2	1.46±0.20E-2	1.36±0.18E-2	1.62±0.20E-2	3.41±0.37E-2	9.52±1.16E-1	1.95±0.30E
UGC07608	2.12±0.21E-2	1.55±0.15E-2	1.49±0.15E-2	5.57±0.76E-3	3.62±0.50E-3	2.62±0.35E-3	3.49±0.45E-3	1.94±0.21E-2	2.36±0.29E-1	3.15±0.51E-
NGC4460 <sup>e</sup>	1.92±0.19E-1	2.03±0.20E-1	1.95±0.19E-1	8.35±1.13E-2	5.62±0.77E-2	7.77±1.00E-2	1.24±0.16E-1	3.05±0.33E-1	3.71±0.45E 0	5.42±0.85E
UGC07639	2.54±0.25E-2	2.67±0.27E-2	2.64±0.26E-2	1.14±0.15E-2	7.69±1.06E-3	4.53±0.60E-3	3.29±0.42E-3	5.57±0.65E-3	1.19±0.16E-1	1.19±0.24E-
NGC4485 <sup>e</sup>	9.47±0.95E-2	9.93±0.99E-2	6.95±0.69E-2	4.25±0.58E-2	2.97±0.41E-2	5.72±0.75E-2	9.46±1.19E-2	1.87±0.20E-1	3.09±0.38E 0	9.62±1.50E
NGC4490 <sup>e</sup>	9.34±0.93E-1	9.35±0.93E-1	8.14±0.81E-1	4.71±0.64E-1	3.23±0.44E-1	7.92±1.01E-1	1.69±0.21E 0	4.29±0.46E 0	6.29±0.77E 1	1.07±0.17E
UGC07690	4.76±0.48E-2	5.26±0.53E-2	2.77±0.28E-2	1.86±0.25E-2	1.26±0.17E-2	1.09±0.14E-2	1.18±0.15E-2	3.01±0.33E-2	7.88±0.96E-1	1.18±0.18E
UGC07699	5.39±0.54E-2	7.75±0.77E-2	5.35±0.54E-2	2.24±0.30E-2	1.43±0.20E-2	1.50±0.19E-2	2.00±0.25E-2	3.75±0.41E-2	7.21±0.88E-1	1.54±0.24E
UGC07698	2.61±0.26E-2	2.58±0.26E-2	2.11±0.21E-2	8.48±1.15E-3	6.98±0.96E-3	4.84±0.91E-3	1.08±0.14E-2	9.86±1.09E-3	1.81±0.23E-1	4.04±0.65E-
UGC07719	1.02±0.10E-2	1.76±0.18E-2	8.71±0.87E-3	4.66±0.63E-3	3.10±0.43E-3	1.71±0.24E-3	1.22±0.17E-3	1.34±0.14E-2	2.20±0.27E-1	1.31±0.23E-
UGC07774	2.03±0.20E-2	2.81±0.28E-2	1.48±0.15E-2	9.08±1.23E-3	5.52±0.76E-3	3.97±0.53E-3	5.24±0.67E-3	9.34±1.02E-3	1.44±0.18E-1	3.68±0.58E-
UGCA292 <sup>e f</sup>	<5.69E-3	<8.04E-3	<1.00E-2	1.68±0.23E-3	5.80±0.80E-4	<6.80E-4	3.00±0.39E-3	<2.47E-3	3.91±0.61E-2	<1.26E-
NGC4594 <sup>e f</sup>	8.07±0.81E 0	9.20±0.92E 0	7.56±0.76E 0	3.94±0.53E 0	2.31±0.32E 0	1.73±0.22E 0	1.30±0.16E 0	6.74±0.43E-1	7.36±0.68E 0	3.61±0.56E
NGC4605	6.49±0.65E-1	6.92±0.69E-1	5.61±0.56E-1	3.25±0.44E-1	2.27±0.31E-1	3.88±0.49E-1	7.36±0.92E-1	1.05±0.11E 0	2.04±0.25E 1	3.74±0.58E
NGC4618 <sup>e</sup>	2.81±0.28E-1	3.26±0.33E-1	2.44±0.24E-1	1.58±0.21E-1	1.04±0.14E-1	1.72±0.22E-1	3.27±0.41E-1	4.01±0.43E-1	7.89±0.96E 0	1.73±0.27E
NGC4625 <sup>e f</sup>	9.82±0.98E-2	1.13±0.11E-1	8.98±0.90E-2	4.85±0.64E-2	3.02±0.40E-2	5.85±0.76E-2	1.29±0.16E-1	1.36±0.06E-1	2.07±0.16E 0	5.07±0.68E
NGC4631 <sup>e f</sup>	1.75±0.17E 0	1.98±0.20E 0	1.84±0.18E 0	1.26±0.17E 0	8.36±1.15E-1	2.45±0.31E 0	5.86±0.73E 0	8.15±0.33E 0	1.30±0.10E 2	2.76±0.35E
UGC07866	2.26±0.23E-2	2.87±0.29E-2	3.16±0.32E-2	8.46±1.15E-3	5.12±0.70E-3	2.53±0.34E-3	2.86±0.37E-3	6.76±0.76E-3	2.42±0.30E-1	2.35±0.39E-
NGC4656	2.01±0.20E-1	1.90±0.19E-1	1.35±0.14E-1	9.54±1.29E-2	7.05±0.97E-2	7.65±0.97E-2	1.02±0.13E-1	5.41±0.58E-1	9.23±1.13E 0	1.23±0.19E
UGC07916	<3.46E-2	<4.89E-2	<6.08E-2	2.51±0.34E-3	1.71±0.24E-3	9.50±1.30E-4	1.06±0.14E-3	6.33±0.69E-3	6.98±0.91E-2	8.10±1.42E-
UGC07950	3.63±0.36E-2	4.17±0.42E-2	3.19±0.32E-2	1.07±0.14E-2	7.41±1.02E-3	7.12±0.94E-3	4.30±0.55E-3	1.16±0.13E-2	3.03±0.37E-1	4.16±0.66E-
UGC07949	9.22±0.92E-3	1.05±0.10E-2	6.88±0.69E-3	3.24±0.44E-3	<8.20E-4	<1.51E-3	<1.64E-3	2.19±0.28E-3	<3.68E-2	<1.39E-
NGC4707	2.39±0.24E-2	2.30±0.23E-2	1.62±0.16E-2	1.09±0.15E-2	6.28±0.86E-3	5.09±0.67E-3	4.30±0.55E-3	1.11±0.12E-2	2.28±0.29E-1	4.67±0.75E-
NGC4736 <sup>e f</sup>	6.95±0.69E 0	7.68±0.77E 0	6.44±0.64E 0	3.60±0.49E 0	2.32±0.32E 0	2.72±0.35E 0	5.17±0.64E 0	5.65±0.23E 0	9.39±0.73E 1	1.74±0.21E
UGC08024 <sup>e f</sup>	9.92±0.99E-3	1.24±0.12E-2	1.20±0.12E-2	4.07±1.00E-3	2.99±1.00E-3	<5.81E-3	<3.99E-3	7.40±1.10E-3	5.70±5.02E-2	2.62±1.25E-
NGC4826 <sup>e f</sup>	5.68±0.57E 0	6.31±0.63E 0	5.28±0.53E 0	2.52±0.34E 0	1.57±0.22E 0	1.64±0.21E 0	2.35±0.29E 0	2.52±0.15E 0	5.07±0.51E 1	8.70±1.27E
UGC08091 <sup>f</sup>	8.86±0.89E-3	1.21±0.12E-2	8.40±0.84E-3	3.06±0.42E-3	2.29±0.32E-3	1.57±0.22E-3	1.47±0.20E-3	4.29±0.49E-3	1.56±0.20E-1	1.48±0.25E-
UGCA319	1.22±0.12E-2	1.39±0.14E-2	1.28±0.13E-2	5.50±0.75E-3	3.51±0.48E-3	2.50±0.34E-3	5.15±0.65E-3	<2.55E-3	<3.43E-2	<1.30E-

Table 2—Continued

Galaxy	2MASS J 1.25 $\mu\text{m}$ (Jy)	2MASS H 1.65 $\mu\text{m}$ (Jy)	2MASS K <sub>s</sub> 2.17 $\mu\text{m}$ (Jy)	IRAC 3.6 $\mu\text{m}$ (Jy)	IRAC 4.5 $\mu\text{m}$ (Jy)	IRAC 5.8 $\mu\text{m}$ (Jy)	IRAC 8.0 $\mu\text{m}$ (Jy)	MIPS 24 $\mu\text{m}$ (Jy)	MIPS 70 $\mu\text{m}$ (Jy)	MIPS 160 $\mu\text{m}$ (Jy)
UGCA320	3.51±0.35E-2	4.67±0.47E-2	<3.27E-1	1.80±0.24E-2	1.45±0.20E-2	3.23±0.42E-3	3.42±0.43E-3	2.33±0.25E-2	5.17±0.63E-1	4.92±0.70E-1
UGC08188	1.18±0.12E-1	1.70±0.17E-1	1.22±0.12E-1	5.96±0.81E-2	4.47±0.61E-2	4.11±0.52E-2	3.56±0.44E-2	6.88±0.74E-2	1.52±0.19E 0	2.88±0.43E-1
UGC08201 <sup>e f</sup>	3.20±0.32E-2	4.69±0.47E-2	3.73±0.37E-2	1.56±0.23E-2	1.18±0.15E-2	5.35±1.70E-3	4.08±0.80E-3	1.42±0.10E-2	1.43±0.69E-1	2.88±2.58E-1
MCG-03-34-002	1.72±0.17E-2	1.78±0.18E-2	2.22±0.22E-2	7.24±0.98E-3	5.10±0.70E-3	4.03±0.54E-3	2.93±0.38E-3	6.79±0.74E-3	1.15±0.15E-1	1.09±0.19E-1
UGC08245	1.78±0.18E-2	1.67±0.17E-2	1.39±0.14E-2	9.41±1.28E-3	5.98±0.82E-3	2.63±0.36E-3	2.89±0.37E-3	4.22±0.50E-3	9.64±1.32E-2	2.42±0.40E-1
NGC5023 <sup>e</sup>	9.86±0.99E-2	1.04±0.10E-1	8.98±0.90E-2	4.50±0.61E-2	2.87±0.39E-2	2.48±0.32E-2	1.99±0.25E-2	5.68±0.61E-2	9.49±1.16E-1	2.30±0.30E-1
CGCG217-018	1.60±0.16E-2	2.13±0.21E-2	1.62±0.16E-2	6.64±0.90E-3	4.24±0.58E-3	3.89±0.52E-3	4.72±0.60E-3	1.19±0.13E-2	1.70±0.21E-1	1.91±0.30E-1
UGC08313	1.81±0.18E-2	2.88±0.29E-2	2.41±0.24E-2	9.25±1.25E-3	5.89±0.81E-3	5.70±0.75E-3	7.10±0.90E-3	2.78±0.30E-2	2.36±0.29E-1	3.57±0.57E-1
UGC08320	5.83±0.58E-2	6.20±0.62E-2	5.02±0.50E-2	1.98±0.27E-2	1.47±0.20E-2	5.37±0.71E-3	7.10±0.90E-3	1.69±0.19E-2	5.64±0.70E-1	7.76±1.23E-1
UGC08331	2.18±0.22E-2	2.33±0.23E-2	1.58±0.16E-2	6.45±0.87E-3	4.49±0.62E-3	2.25±0.31E-3	2.21±0.29E-3	6.98±0.79E-3	1.67±0.22E-1	3.85±0.63E-1
NGC5055 <sup>e f</sup>	4.21±0.42E 0	4.96±0.50E 0	4.05±0.41E 0	2.38±0.32E 0	1.55±0.21E 0	2.63±0.34E 0	5.64±0.70E 0	5.74±0.23E 0	7.27±0.52E 1	2.95±0.37E-1
NGC5068	8.64±0.86E-1	8.12±0.81E-1	7.10±0.71E-1	4.59±0.62E-1	3.26±0.45E-1	4.87±0.61E-1	1.24±0.15E 0	1.37±0.15E 0	2.08±0.25E 1	5.42±0.83E-1
IC4247	1.85±0.19E-2	1.57±0.16E-2	1.39±0.14E-2	6.36±0.86E-3	4.33±0.60E-3	2.07±0.28E-3	1.90±0.25E-3	...	...	...
NGC5204 <sup>e</sup>	1.43±0.14E-1	1.48±0.15E-1	1.12±0.11E-1	6.80±0.92E-2	4.59±0.63E-2	5.04±0.65E-2	8.22±1.03E-2	1.78±0.19E-1	4.01±0.49E 0	7.36±1.14E-1
NGC5194 <sup>e f</sup>	4.99±0.50E 0	5.89±0.59E 0	4.52±0.45E 0	2.66±0.36E 0	1.80±0.26E 0	4.23±0.54E 0	1.06±0.13E 1	1.27±0.05E 1	1.47±0.11E 2	4.91±0.60E-1
NGC5195 <sup>e f</sup>	2.37±0.24E 0	2.80±0.28E 0	2.25±0.23E 0	8.34±1.13E-1	5.11±0.70E-1	4.62±0.61E-1	6.46±0.81E-1	1.39±0.27E 0	1.55±0.33E 1	1.34±0.30E-1
UGC08508	2.18±0.22E-2	2.13±0.21E-2	1.39±0.14E-2	8.43±1.14E-3	5.10±0.70E-3	3.91±0.52E-3	4.27±0.54E-3	6.27±0.70E-3	1.46±0.19E-1	1.95±0.33E-1
NGC5229	3.60±0.36E-2	4.76±0.48E-2	4.23±0.42E-2	1.31±0.18E-2	8.57±1.18E-3	7.39±0.97E-3	8.07±1.02E-3	1.66±0.18E-2	3.56±0.44E-1	5.54±0.83E-1
NGC5238	4.44±0.44E-2	5.07±0.51E-2	3.47±0.35E-2	1.23±0.17E-2	8.72±1.20E-3	8.29±1.08E-3	5.30±0.67E-3	1.63±0.18E-2	4.01±0.50E-1	7.38±1.10E-1
[KK98]208	<2.20E-1	<3.19E-1	<3.91E-1	<3.10E-4	<4.60E-4	<1.70E-3	<1.86E-3	...	...	...
NGC5236 <sup>f</sup>	1.13±0.11E 1	1.26±0.13E 1	1.04±0.10E 1	6.23±0.84E 0	4.11±0.56E 0	9.49±1.18E 0	2.41±0.30E 1	3.96±0.43E 1	3.50±0.43E 2	7.93±1.23E-1
ESO444-G084	<1.54E-2	<2.21E-2	<2.69E-2	2.79±0.38E-3	1.76±0.24E-3	1.59±0.22E-3	6.30±0.90E-4	...	...	...
UGC08638	1.32±0.13E-2	2.29±0.23E-2	1.52±0.15E-2	7.48±1.01E-3	5.01±0.69E-3	2.77±0.37E-3	2.24±0.29E-3	9.00±0.99E-3	1.41±0.18E-1	2.30±0.30E-1
UGC08651	2.09±0.21E-2	1.59±0.16E-2	1.59±0.16E-2	5.93±0.80E-3	3.91±0.54E-3	1.79±0.24E-3	1.35±0.18E-3	3.41±0.40E-3	7.38±1.13E-2	1.30±0.23E-1
NGC5253 <sup>e</sup>	4.40±0.44E-1	4.44±0.44E-1	3.54±0.35E-1	2.42±0.33E-1	2.62±0.36E-1	5.38±0.69E-1	8.07±1.01E-1	...	...	...
NGC5264	1.50±0.15E-1	1.15±0.12E-1	1.08±0.11E-1	5.31±0.72E-2	3.68±0.50E-2	3.60±0.46E-2	4.22±0.53E-2	...	...	...
UGC08760	1.48±0.15E-2	1.29±0.13E-2	1.59±0.16E-2	6.10±0.83E-3	4.36±0.60E-3	2.08±0.28E-3	1.35±0.18E-3	1.19±0.14E-3	<5.58E-2	<2.10E-1
kkh086	<2.53E-2	<3.56E-2	<4.41E-2	1.29±0.18E-3	7.20±1.00E-4	<7.60E-4	<8.30E-4	<2.76E-3	<3.72E-2	<1.40E-1
UGC08837	3.44±0.34E-2	2.27±0.23E-2	2.65±0.26E-2	1.56±0.21E-2	1.00±0.14E-2	7.17±0.94E-3	1.06±0.13E-2	1.90±0.21E-2	2.86±0.36E-1	7.69±1.23E-1
UGC08833	1.20±0.12E-2	6.30±0.63E-3	3.43±0.34E-3	2.45±0.33E-3	2.05±0.28E-3	<1.73E-3	<1.89E-3	<3.14E-3	<4.24E-2	<1.60E-1
NGC5457 <sup>e f</sup>	4.38±0.44E 0	5.04±0.50E 0	4.41±0.44E 0	2.52±0.34E 0	1.74±0.24E 0	3.40±0.42E 0	7.48±0.93E 0	1.03±0.11E 1	1.14±0.14E 2	3.96±0.63E-1
NGC5474 <sup>e f</sup>	1.43±0.14E-1	1.59±0.16E-1	1.14±0.11E-1	1.04±0.14E-1	7.34±1.02E-2	7.59±1.01E-2	1.17±0.15E-1	1.84±0.08E-1	3.72±0.27E 0	9.87±1.23E-1
NGC5477 <sup>f</sup>	2.39±0.24E-2	2.47±0.25E-2	2.20±0.22E-2	7.41±1.01E-3	5.16±0.71E-3	4.19±0.56E-3	2.60±0.34E-3	1.72±0.19E-2	4.25±0.52E-1	4.38±0.70E-1

Table 2—Continued

Galaxy	2MASS J 1.25 $\mu\text{m}$ (Jy)	2MASS H 1.65 $\mu\text{m}$ (Jy)	2MASS K <sub>s</sub> 2.17 $\mu\text{m}$ (Jy)	IRAC 3.6 $\mu\text{m}$ (Jy)	IRAC 4.5 $\mu\text{m}$ (Jy)	IRAC 5.8 $\mu\text{m}$ (Jy)	IRAC 8.0 $\mu\text{m}$ (Jy)	MIPS 24 $\mu\text{m}$ (Jy)	MIPS 70 $\mu\text{m}$ (Jy)	MIPS 160 $\mu\text{m}$ (Jy)
[KK98]230	<7.67E-3	<1.08E-2	<1.35E-2	4.60±0.60E-4	3.30±0.50E-4	<8.60E-4	<9.40E-4	<3.44E-3	<4.64E-2	<1.75E-1
UGC09128 <sup>e</sup>	1.30±0.13E-2	9.19±0.92E-3	9.25±0.93E-3	3.10±0.42E-3	2.39±0.33E-3	<1.54E-3	<1.68E-3	<2.80E-3	<3.78E-2	<1.43E-1
NGC5585 <sup>e</sup>	1.45±0.14E-1	1.57±0.16E-1	1.12±0.11E-1	8.69±1.18E-2	5.87±0.81E-2	6.56±0.84E-2	8.89±1.11E-2	1.38±0.15E-1	3.00±0.37E 0	7.46±1.17E-1
UGC09240	4.80±0.48E-2	4.17±0.42E-2	3.32±0.33E-2	1.55±0.21E-2	1.07±0.15E-2	7.95±1.04E-3	7.80±0.98E-3	2.32±0.25E-2	3.60±0.45E-1	4.96±0.79E-1
UGC09405	1.51±0.15E-2	2.01±0.20E-2	1.29±0.13E-2	6.67±0.90E-3	3.98±0.55E-3	2.73±0.37E-3	3.74±0.48E-3	4.57±0.54E-3	5.66±0.97E-2	1.65±0.30E-1
MRK475	2.26±0.23E-3	2.00±0.20E-3	1.42±0.14E-3	9.80±1.30E-4	8.00±1.10E-4	5.40±0.90E-4	8.20±1.10E-4	9.27±1.00E-3	1.14±0.14E-1	4.15±0.89E-1
NGC5832	1.07±0.11E-1	1.09±0.11E-1	9.68±0.97E-2	4.50±0.61E-2	2.92±0.40E-2	2.98±0.38E-2	4.59±0.57E-2	4.39±0.47E-2	8.13±1.00E-1	2.68±0.42E-1
NGC5949	1.39±0.14E-1	1.47±0.15E-1	1.21±0.12E-1	7.01±0.95E-2	4.48±0.62E-2	7.55±0.98E-2	1.50±0.19E-1	1.44±0.16E-1	2.18±0.27E 0	6.11±0.95E-1
UGC09992	1.14±0.11E-2	9.90±0.99E-3	9.72±0.97E-3	4.80±0.65E-3	3.24±0.45E-3	1.51±0.21E-3	3.79±0.48E-3	6.79±0.75E-3	1.16±0.15E-1	1.37±0.24E-1
KKR25 <sup>e f</sup>	<1.89E-2	<2.68E-2	<3.34E-2	<2.40E-4	<3.60E-4	<1.32E-3	<1.44E-3	<2.40E-3	<3.24E-2	<1.22E-1
NGC6503 <sup>e</sup>	9.49±0.95E-1	1.05±0.10E 0	8.60±0.86E-1	4.34±0.59E-1	2.91±0.40E-1	5.01±0.64E-1	9.28±1.16E-1	8.65±0.93E-1	1.44±0.18E 1	3.58±0.56E-1
IC4951	3.47±0.35E-2	3.60±0.36E-2	3.44±0.34E-2	1.02±0.14E-2	7.20±0.99E-3	5.75±0.76E-3	3.53±0.45E-3	...	...	...
DDO210 <sup>f</sup>	<2.59E-2	<3.75E-2	<4.59E-2	2.80±0.38E-3	1.69±0.23E-3	<1.55E-3	<1.69E-3	<2.82E-3	<3.79E-2	<1.43E-1
IC5052 <sup>e</sup>	2.38±0.24E-1	2.47±0.25E-1	2.01±0.20E-1	1.24±0.17E-1	8.65±1.19E-2	9.01±1.16E-2	1.39±0.17E-1	3.82±0.41E-1	4.56±0.56E 0	8.52±1.33E-1
NGC7064	6.58±0.66E-2	4.87±0.49E-2	4.41±0.44E-2	2.37±0.32E-2	1.54±0.21E-2	1.12±0.15E-2	1.19±0.15E-2	3.24±0.35E-2	1.01±0.12E 0	1.93±0.21E-1
NGC7090 <sup>e</sup>	4.34±0.43E-1	4.83±0.48E-1	3.92±0.39E-1	2.18±0.30E-1	1.45±0.20E-1	2.49±0.32E-1	4.87±0.61E-1	6.53±0.70E-1	1.03±0.13E 1	2.84±0.44E-1
IC5152 <sup>d e</sup>	4.60±0.46E-1	3.37±0.34E-1	3.06±0.31E-1	...	1.66±0.23E-1	...	2.27±0.28E-1	2.09±0.23E-1	4.86±0.59E 0	1.13±0.18E-1
IC5256	2.85±0.28E-2	2.58±0.26E-2	2.10±0.21E-2	8.08±1.10E-3	5.37±0.74E-3	8.82±1.17E-3	1.75±0.22E-2	1.88±0.20E-2	2.79±0.34E-1	6.06±0.95E-1
UGCA438	2.18±0.22E-2	2.27±0.23E-2	1.68±0.17E-2	9.02±1.22E-3	6.34±0.87E-3	3.85±0.51E-3	4.23±0.53E-3	<4.66E-3	<6.29E-2	<2.38E-1
ESO347-G017	1.86±0.19E-2	2.00±0.20E-2	1.59±0.16E-2	8.80±1.19E-3	5.68±0.78E-3	3.21±0.43E-3	2.94±0.38E-3	8.51±0.95E-3	2.77±0.35E-1	2.91±0.48E-1
UGC12613 <sup>f</sup>	1.22±0.12E-1	9.81±0.98E-2	1.14±0.11E-1	5.55±0.75E-2	3.31±0.46E-2	1.84±0.24E-2	2.63±0.33E-2	2.57±0.28E-2	3.48±0.45E-1	1.21±0.19E-1
IC5332	4.14±0.41E-1	5.73±0.57E-1	3.86±0.39E-1	2.38±0.32E-1	1.64±0.23E-1	1.85±0.23E-1	2.93±0.37E-1	3.34±0.36E-1	4.61±0.56E 0	1.98±0.31E-1
NGC7713	1.79±0.18E-1	2.24±0.22E-1	1.51±0.15E-1	1.00±0.14E-1	6.85±0.94E-2	8.53±1.09E-2	1.40±0.17E-1	2.84±0.31E-1	5.69±0.69E 0	1.09±0.17E-1
UGCA442	2.32±0.23E-2	2.37±0.24E-2	1.34±0.13E-2	1.12±0.15E-2	7.51±1.03E-3	3.81±0.51E-3	2.63±0.34E-3	1.01±0.11E-2	1.20±0.16E-1	2.63±0.44E-1
kkh098	1.02±0.10E-2	1.07±0.11E-2	7.56±0.76E-3	2.42±0.33E-3	1.56±0.22E-3	<1.46E-3	<1.60E-3	<2.65E-3	<3.56E-2	<1.34E-1
ESO149-G003	1.03±0.10E-2	1.27±0.13E-2	<1.01E-1	3.55±0.48E-3	2.59±0.36E-3	6.90±1.00E-4	8.40±1.10E-4	8.90±1.60E-4	5.59±0.82E-2	<2.14E-1
NGC7793 <sup>e f</sup>	1.68±0.17E 0	1.70±0.17E 0	1.31±0.13E 0	7.71±1.04E-1	4.69±0.64E-1	1.02±0.13E 0	1.85±0.23E 0	2.03±0.08E 0	3.33±0.24E 1	1.17±0.15E-1

Note. — See § 4 for corrections that have been applied to the data. The uncertainties include both statistical and systematic effects ( $\lesssim 10\%$  for the near-infrared data).

<sup>a</sup>Infrared photometry for the Large and Small Magellanic Clouds are from Bernard et al. (2008) and Leroy et al. (2007), respectively.

<sup>b</sup>NGC 1800 and MCG-05-13-004 spatially overlap so separate photometry for MCG-05-13-004 is not provided.

<sup>c</sup>The bright core of NGC 3034 (M 82) has rendered the *Spitzer* data extremely difficult to process; saturation effects severely limit our ability to extract reliable flux densities.

<sup>d</sup>Only 4.5 and 8.0  $\mu\text{m}$  data were obtained for IC 5152.

<sup>e</sup>IRAC imaging taken from the archives.

<sup>f</sup>MIPS imaging taken from the archives.

Table 3. IRAC Aperture Correction Parameters

$\lambda$	A	B	C
3.5 $\mu\text{m}$	0.82	0.370	0.910
4.5 $\mu\text{m}$	1.16	0.443	0.940
5.8 $\mu\text{m}$	1.49	0.207	0.710
8.0 $\mu\text{m}$	1.37	0.330	0.740

Note. — See § 4 and  
<http://ssc.spitzer.caltech.edu/irac/calib/extcal/>

Table 4. LVL Infrared Ratios and Dispersions

Ratio	Median	Dispersion (dex)
$f_\nu(70\mu\text{m})/f_\nu(160\mu\text{m})$	0.84	0.22
$f_\nu(8.0\mu\text{m})/f_\nu(24\mu\text{m})$	0.41	0.27
$\nu f_\nu(8.0\mu\text{m})/TIR$	0.098	0.23
$\nu f_\nu(8.0\mu\text{m})_{\text{dust}}/TIR$	0.19	0.44
$\nu f_\nu(24\mu\text{m})/TIR$	0.080	0.15
$\nu f_\nu(70\mu\text{m})/TIR$	0.60	0.11
$\nu f_\nu(160\mu\text{m})/TIR$	0.31	0.12



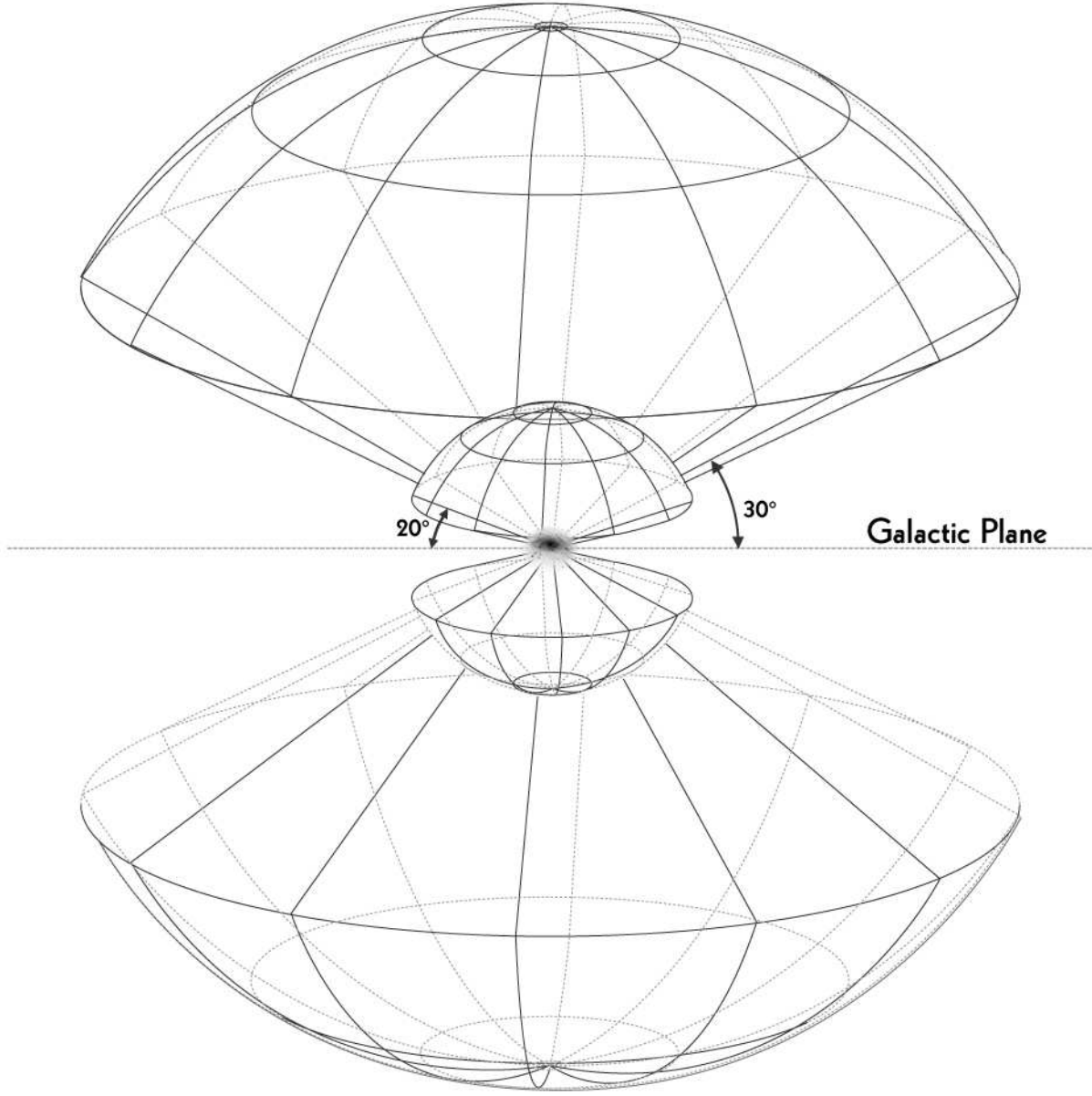


Fig. 1.— Schematic representation of the tiered observing strategy for the Local Volume Legacy survey. LVL is obtaining *Spitzer* MIPS and IRAC imaging for *i*) all known galaxies in the inner tier, which begins beyond the Local Group and extends to 3.5 Mpc, and *ii*) a magnitude-limited sample to  $m_B = 15.5$  mag within the outer tier which extends to 11 Mpc. These *Spitzer* data complement the groundbased  $H\alpha$  and *GALEX* ultraviolet imaging already available throughout the two-tiered volume. Image designed by Pete Marenfeld (NOAO/AURA/NSF).

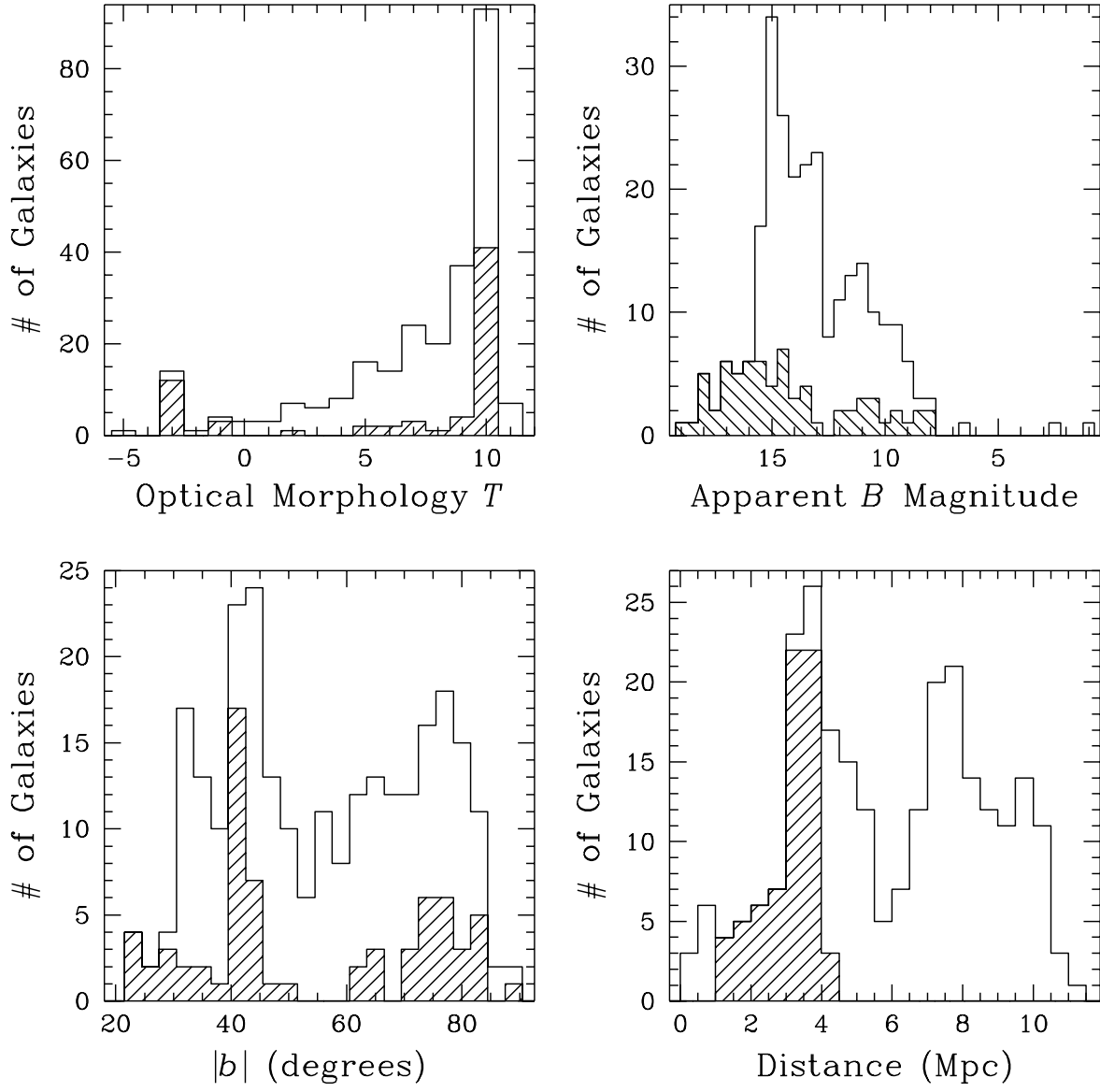


Fig. 2.— TDistributions of RC3 type (top left), apparent B magnitude (top right), Galactic latitude (bottom left) and distance (bottom right) for the Local Volume Legacy galaxy sample. The histograms outlined by the solid lines show the entire sample, whereas the shaded portions of the histograms portray only the inner-tier ANGST subsample for which *Hubble* ACS imaging is available.

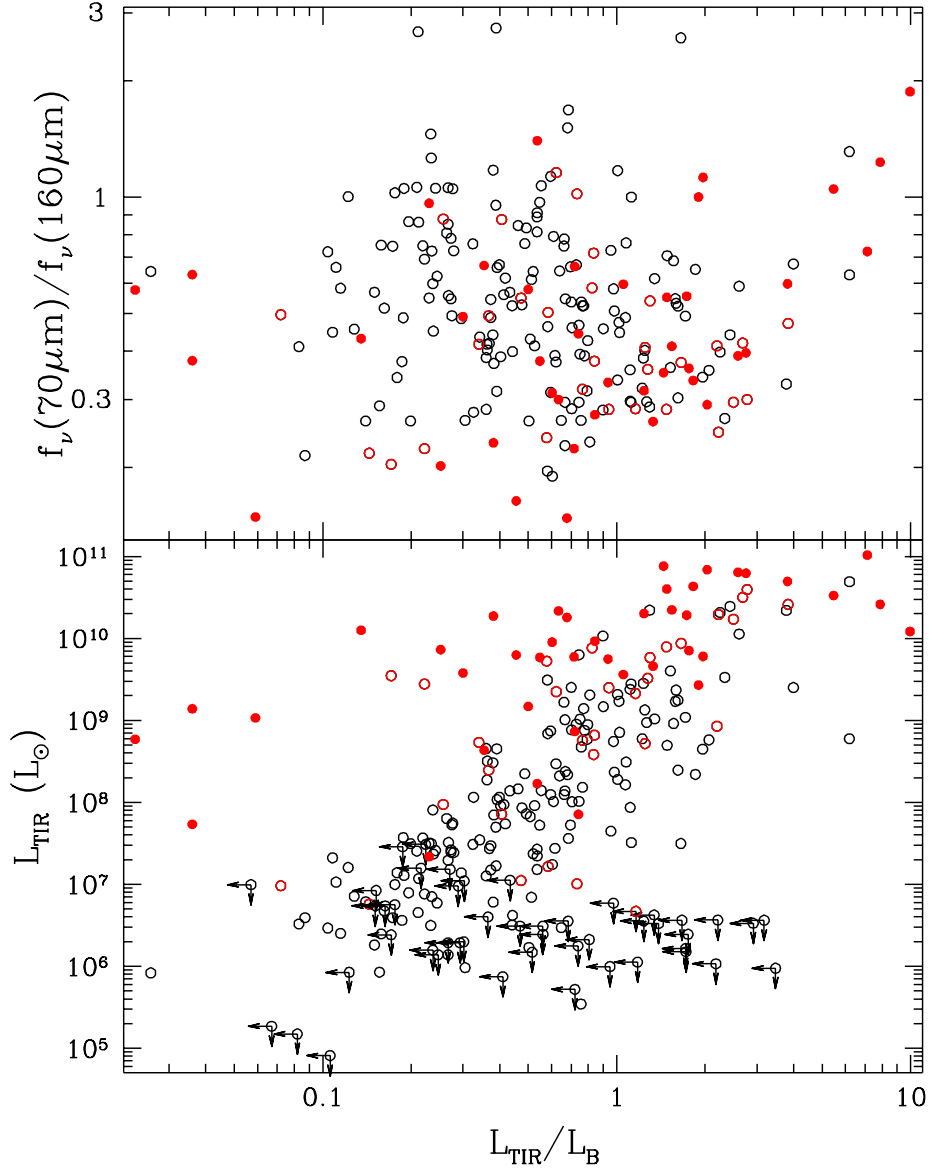


Fig. 3.— The range of total infrared and total infrared-to-optical properties in the LVL (open black circles) and SINGS (filled red circles) samples. Open red circles denote galaxies in both samples. SINGS data are taken from Dale et al. (2007).

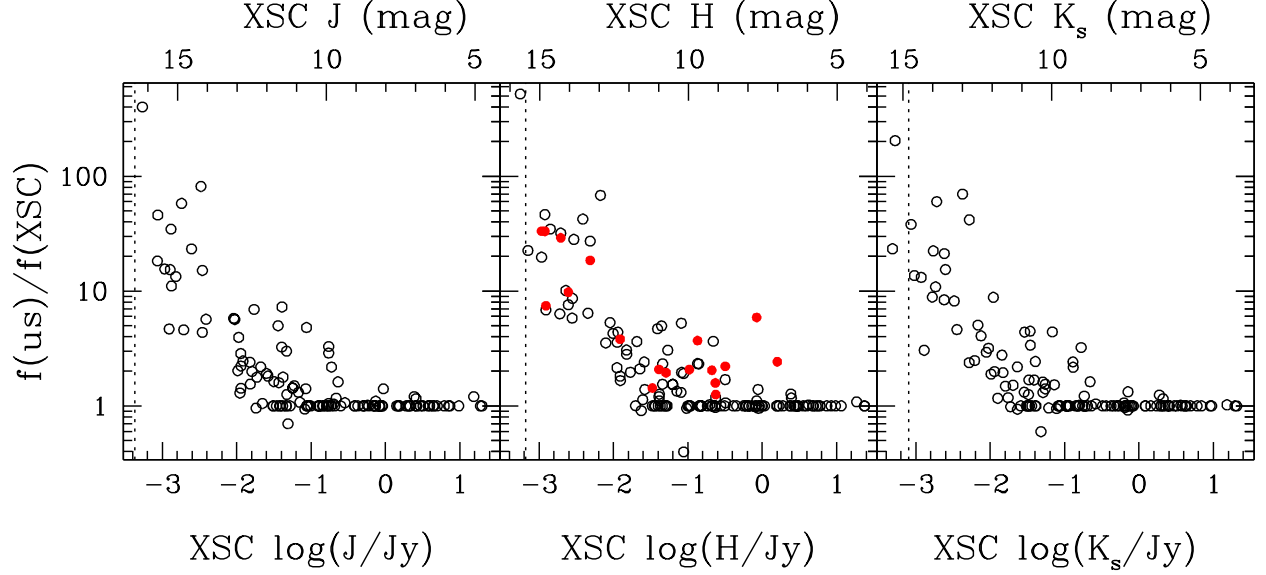


Fig. 4.— A comparison of near-infrared fluxes extracted from the 2MASS image archives using the apertures described in § 4.2 with those from the 2MASS Extended Source Catalog. The filled red circles are based on deep  $H$  band imaging of nearby galaxies with the 3.9 m Anglo-Australian Telescope (Kirby et al. 2008). The vertical dotted lines indicate the 2MASS  $10\sigma$  point source detection limits.

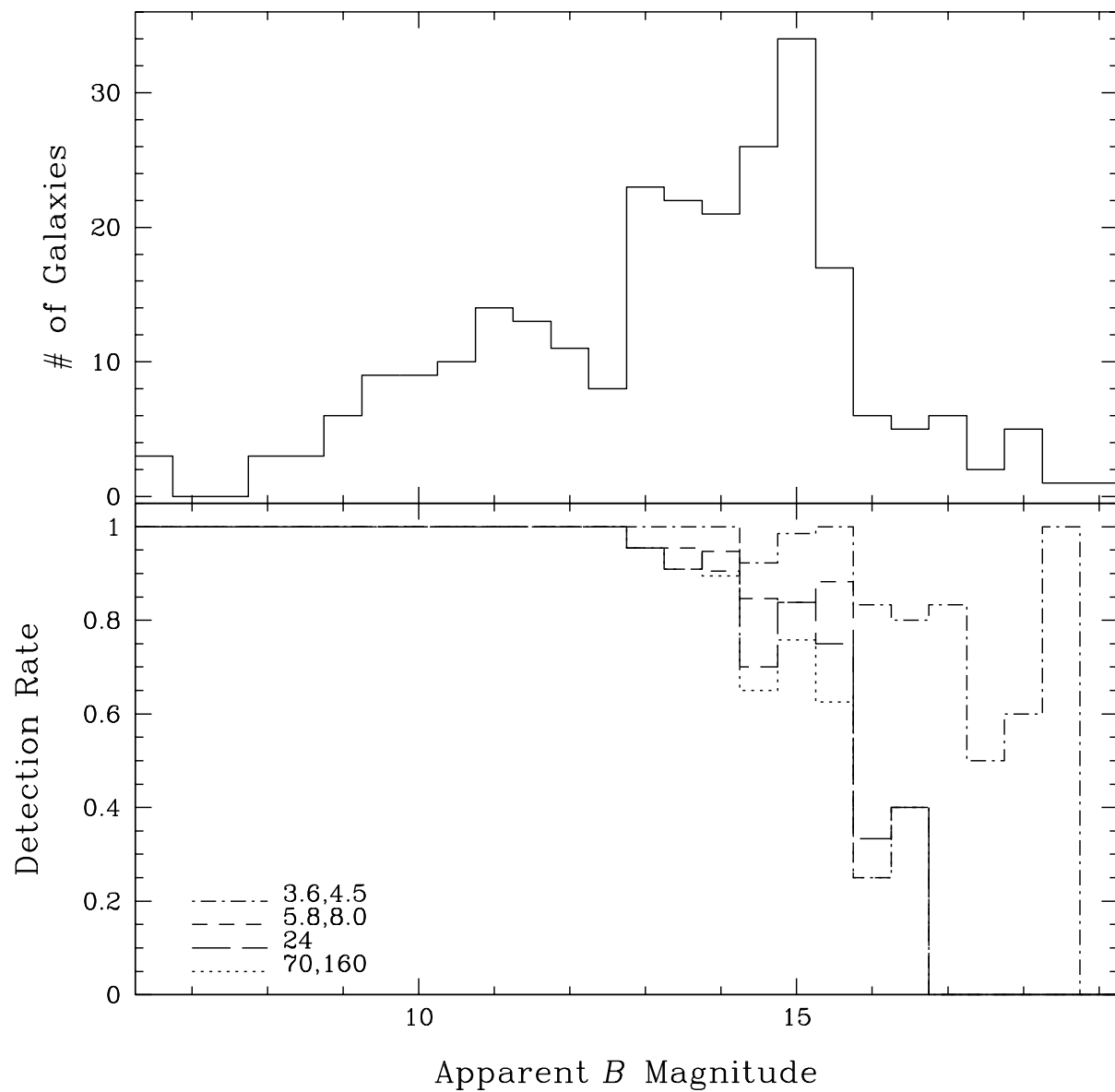


Fig. 5.— Top: The distribution of LVL galaxies as a function of apparent  $B$ -band magnitude. Bottom: The imaging detection rate for different *Spitzer* wavelengths.

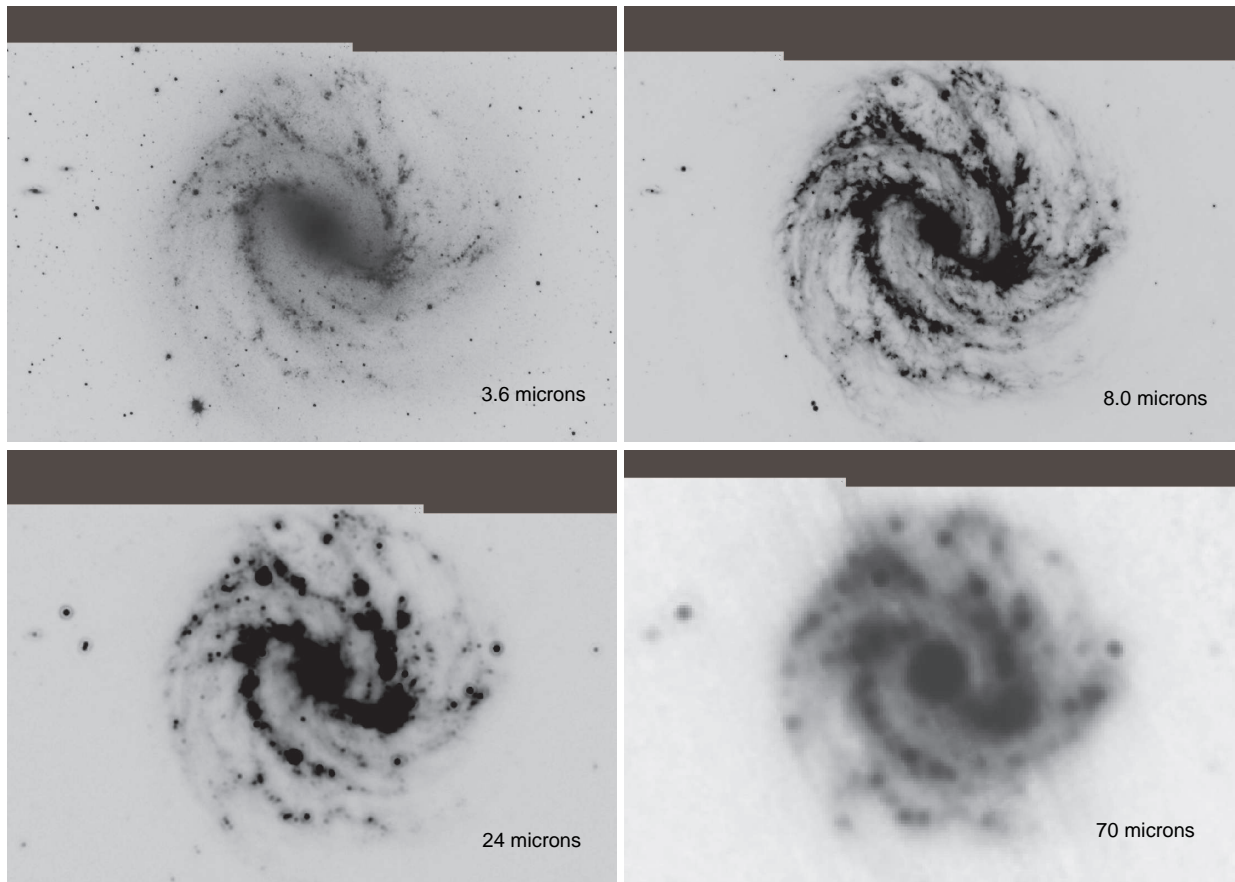


Fig. 6.— An infrared mosaic of NGC 5236.

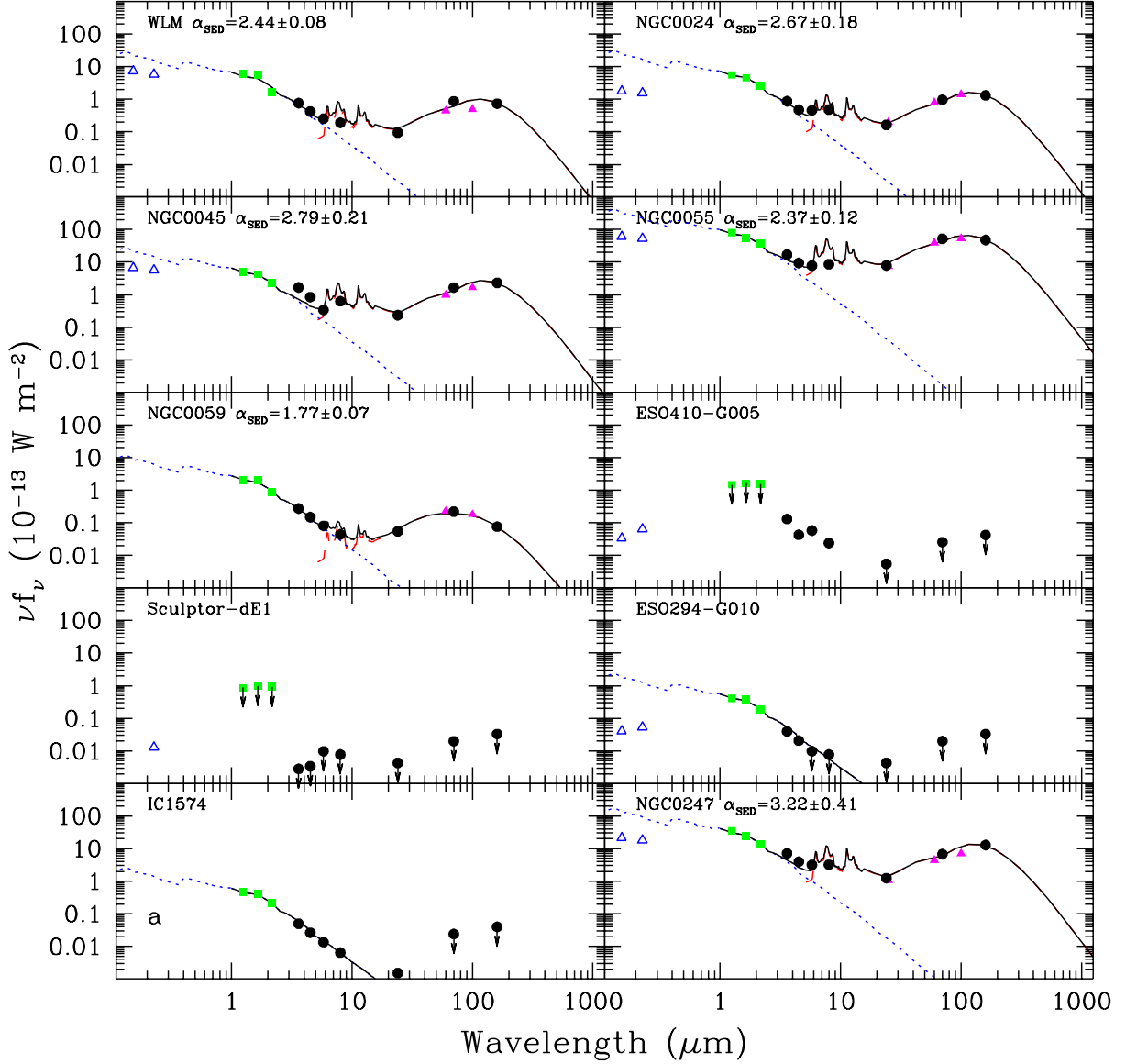


Fig. 7.— Globally-integrated 0.15-160  $\mu\text{m}$  spectral energy distributions for the LVL sample. *GALEX* (Gil de Paz et al. 2009), 2MASS, and *Spitzer* data are represented by open triangles, filled squares, and filled circles, respectively. Downward-pointing arrows, if present, indicate  $3\sigma$  upper limits. The solid curve is the sum of a dust (dashed) and a stellar (dotted) model. The dust curve is a Dale & Helou (2002) model fitted to the amplitude and ratios of the observed 24, 70, and 160  $\mu\text{m}$  fluxes; the  $\alpha_{\text{SED}}$  listed within each panel parametrizes the distribution of dust mass as a function of heating intensity, as described in Dale & Helou (2002). The stellar curve, serving merely as a fiducial visual aid, is a 1 Gyr continuous star formation, solar metallicity curve from Vazquez & Leitherer (2005) fitted to the 2MASS data (see § 5.2 for details).

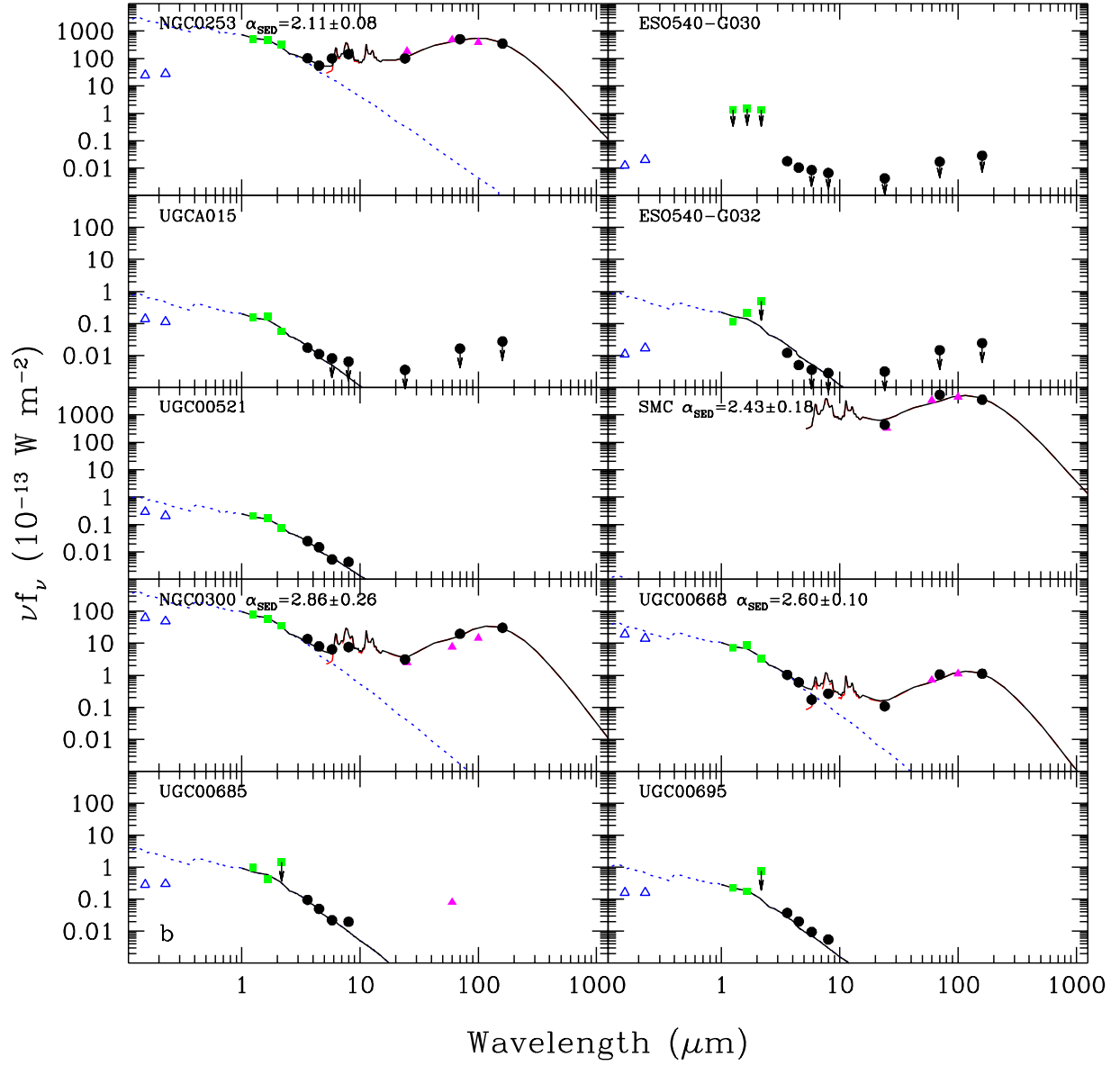


Fig. 8.— Globally-integrated 0.15-160  $\mu\text{m}$  spectral energy distributions for the LVL sample (continued).



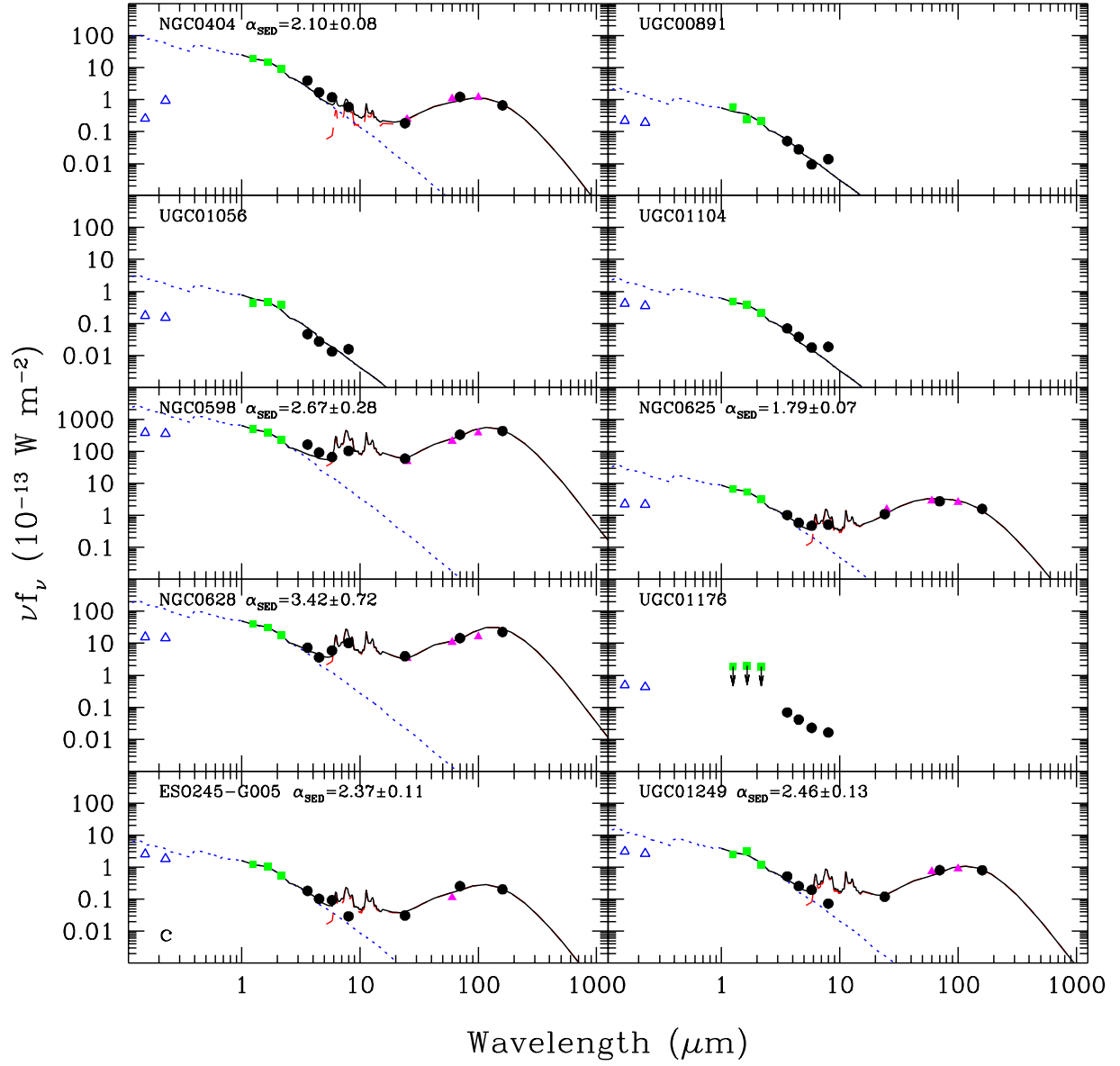


Fig. 9.— Globally-integrated 0.15-160  $\mu\text{m}$  spectral energy distributions for the LVL sample (continued).

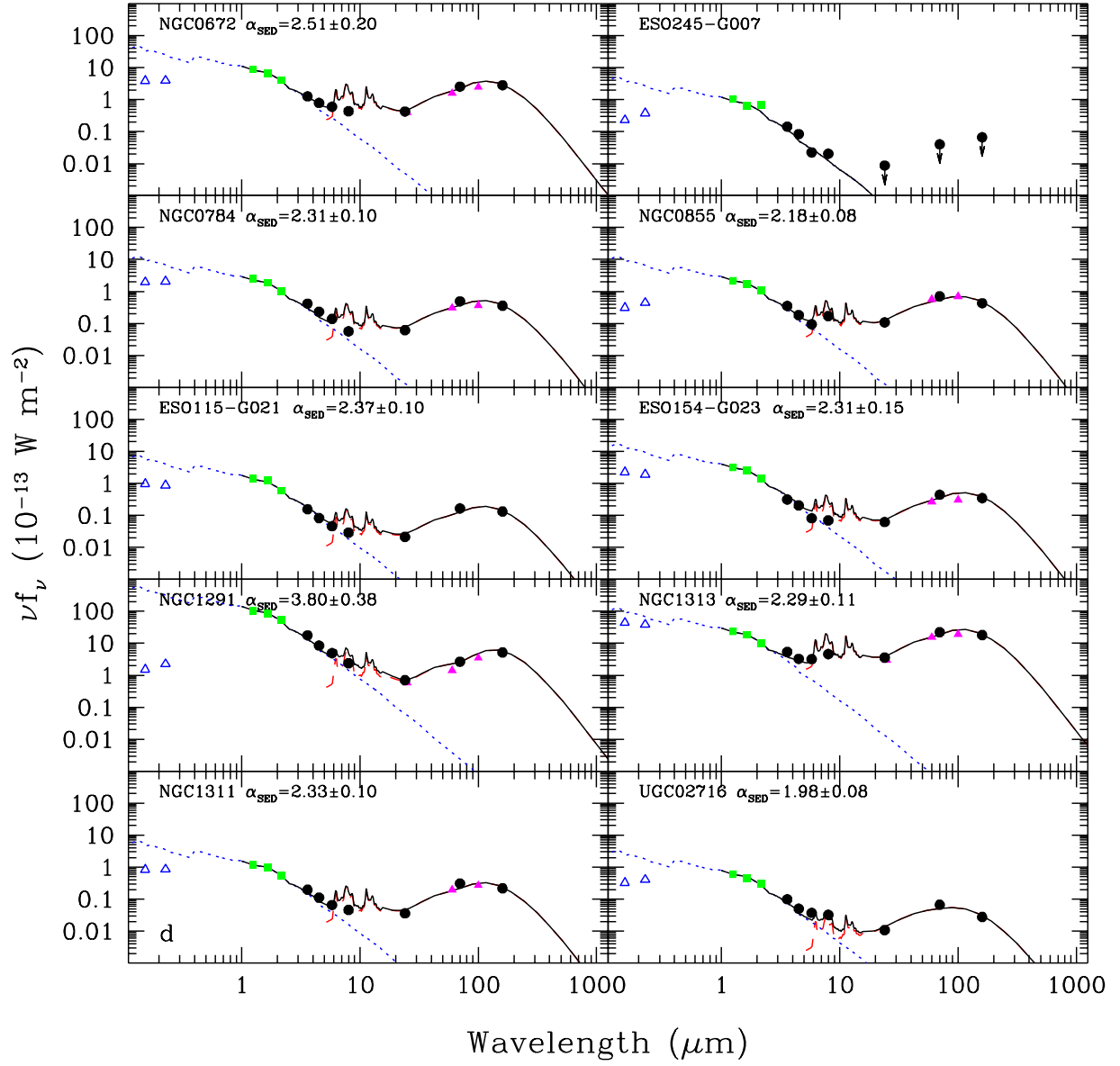


Fig. 10.— Globally-integrated 0.15-160  $\mu\text{m}$  spectral energy distributions for the LVL sample (continued).

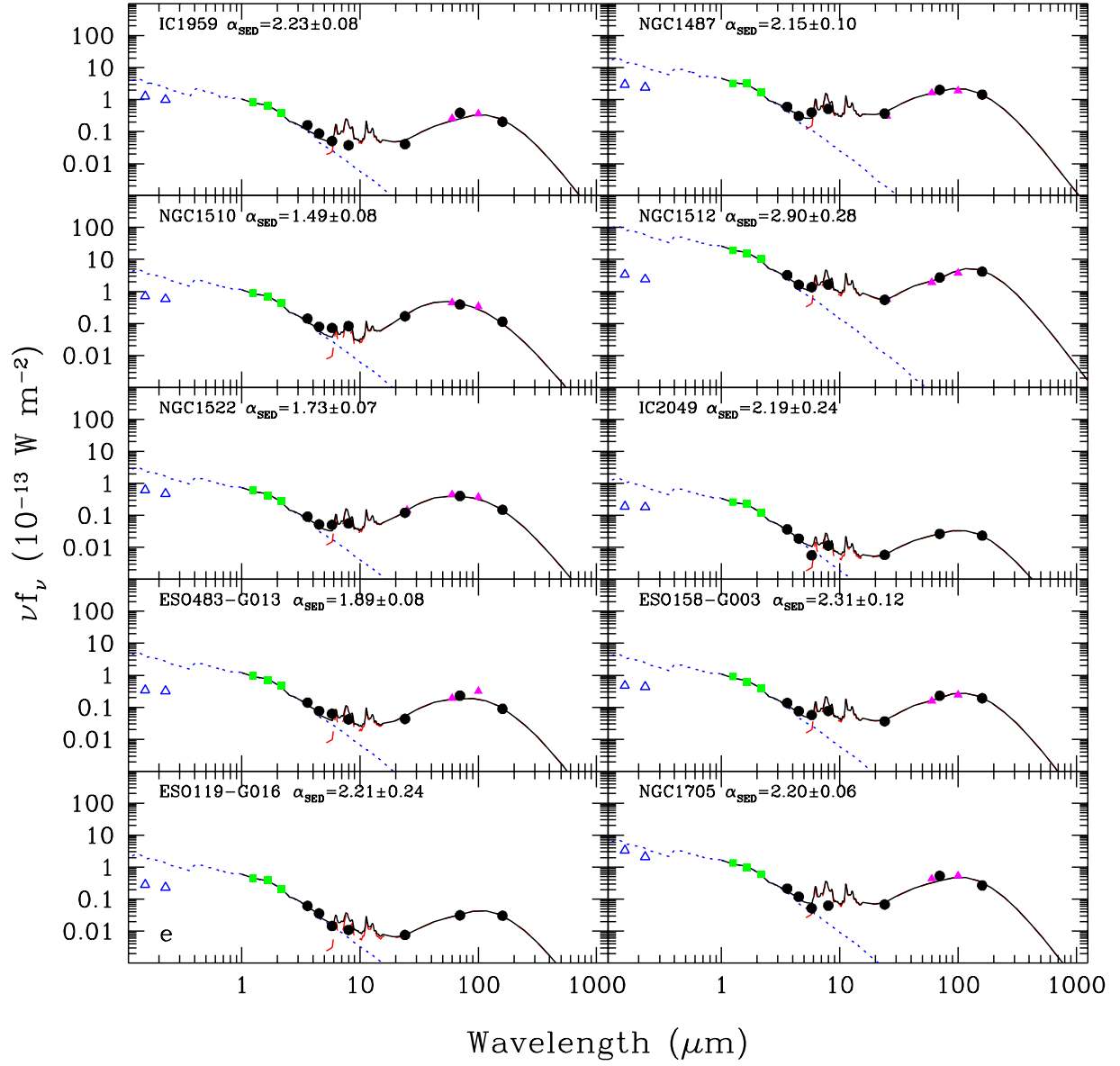


Fig. 11.— Globally-integrated 0.15-160  $\mu\text{m}$  spectral energy distributions for the LVL sample (continued).

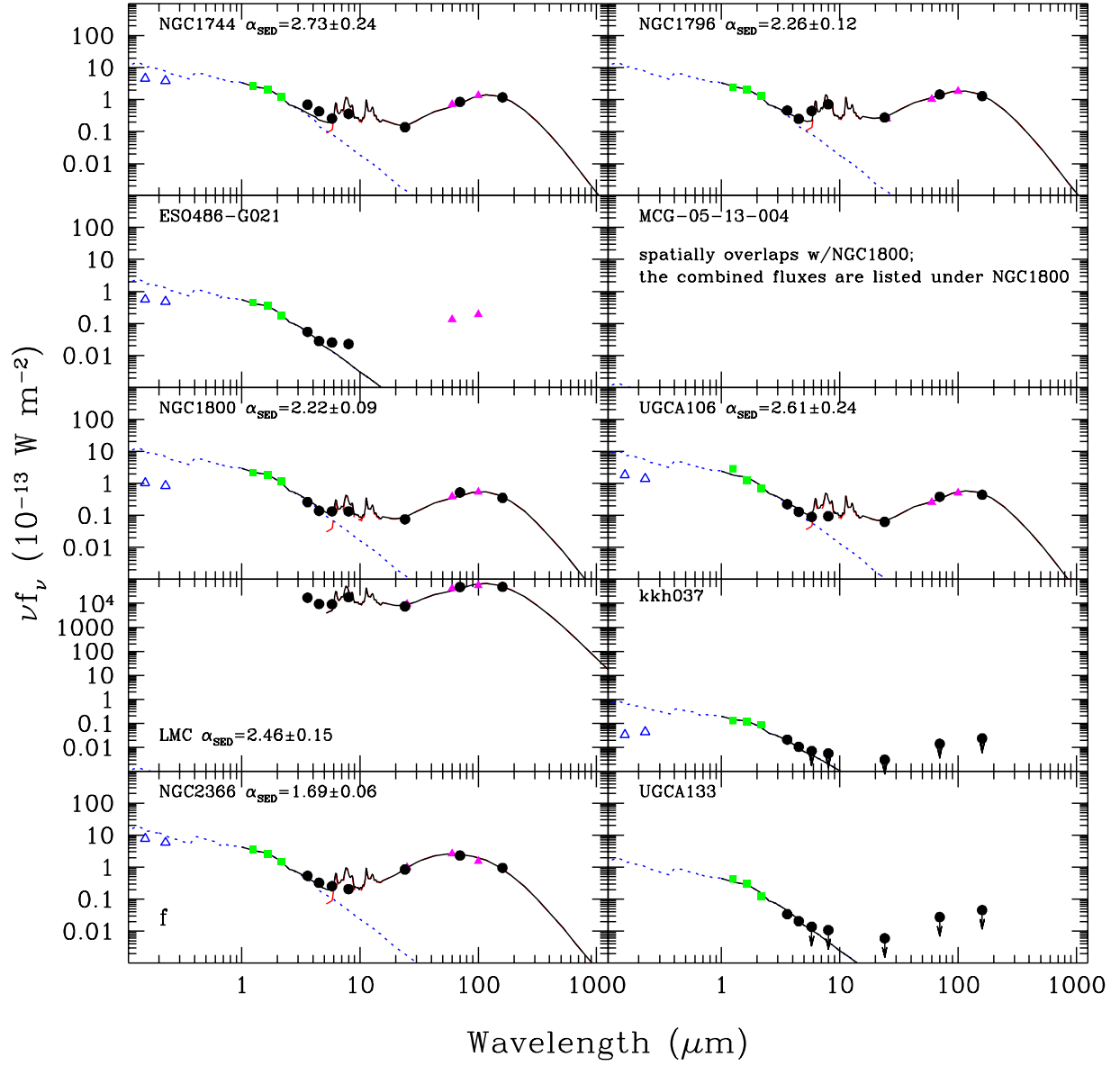


Fig. 12.— Globally-integrated 0.15-160  $\mu\text{m}$  spectral energy distributions for the LVL sample (continued).

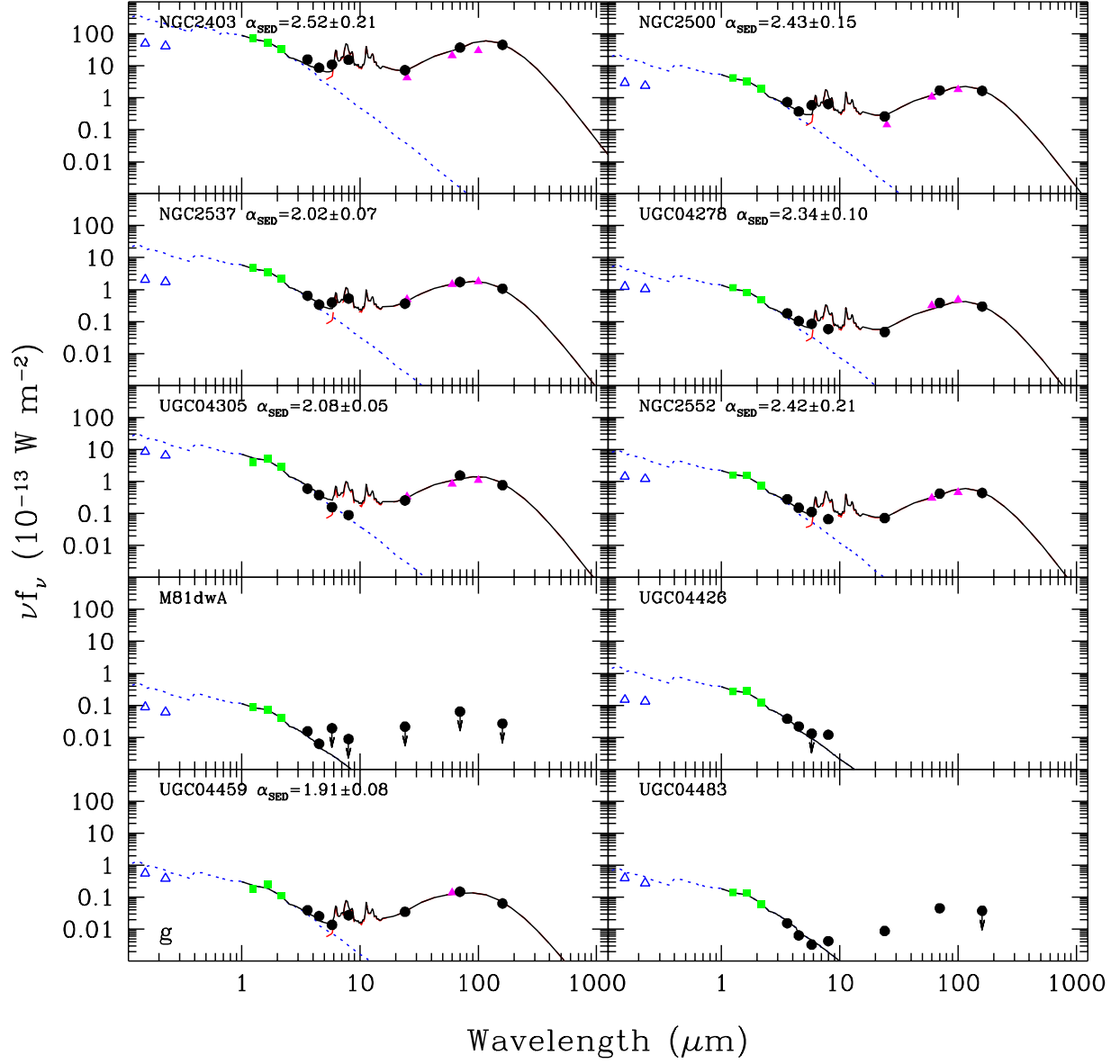


Fig. 13.— Globally-integrated 0.15-160  $\mu\text{m}$  spectral energy distributions for the LVL sample (continued).

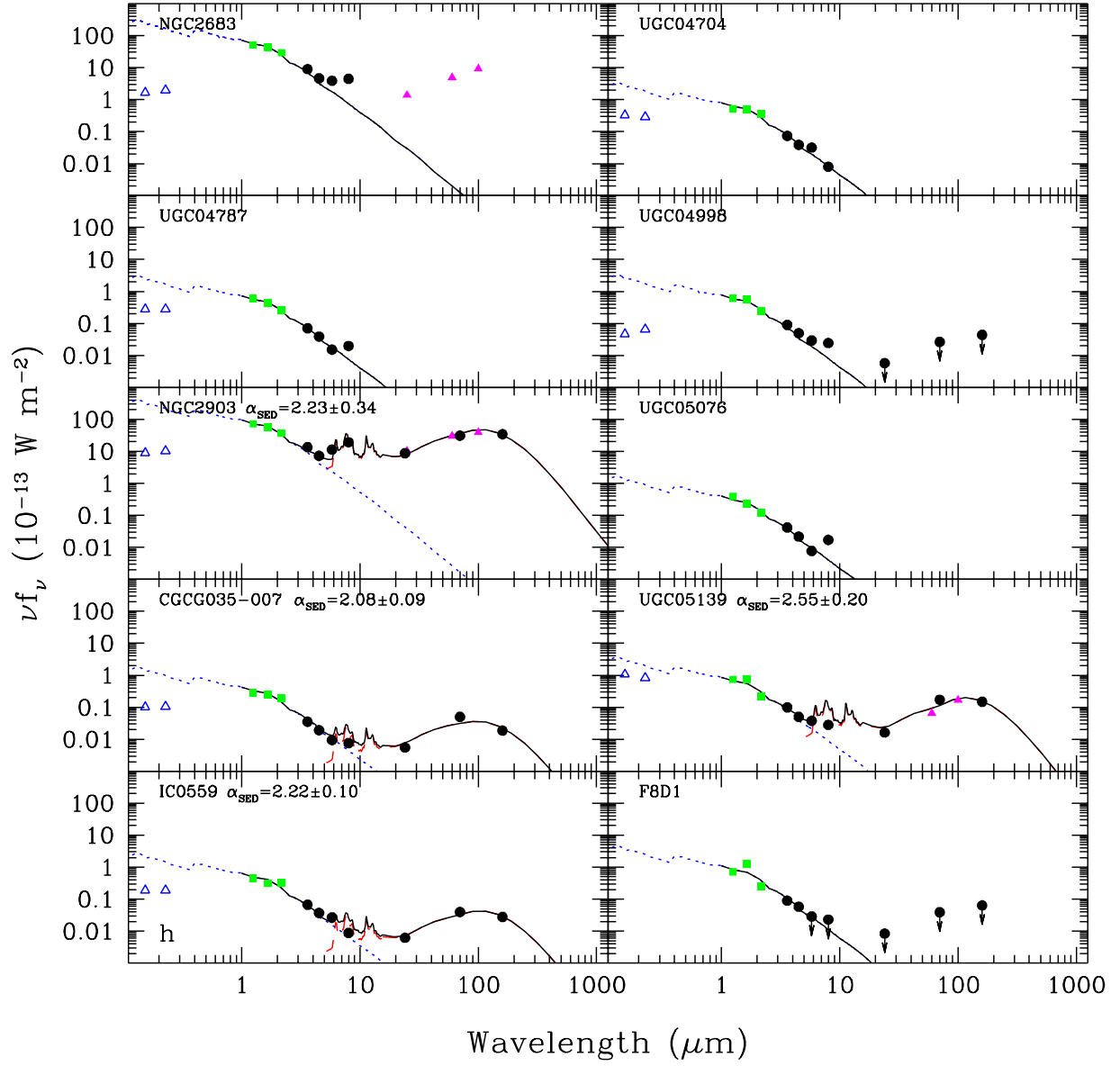


Fig. 14.— Globally-integrated 0.15-160  $\mu\text{m}$  spectral energy distributions for the LVL sample (continued).

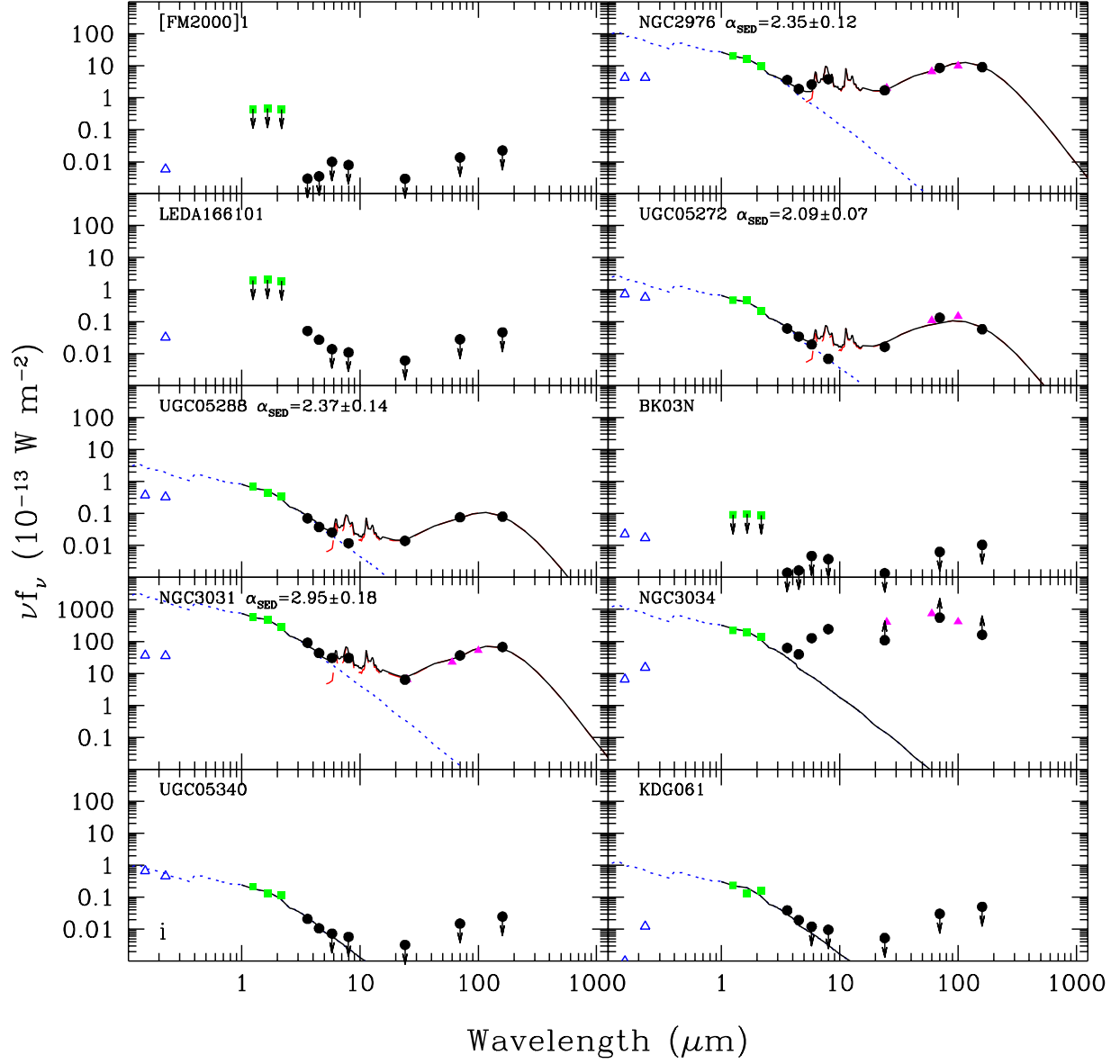


Fig. 15.— Globally-integrated 0.15-160  $\mu\text{m}$  spectral energy distributions for the LVL sample (continued).

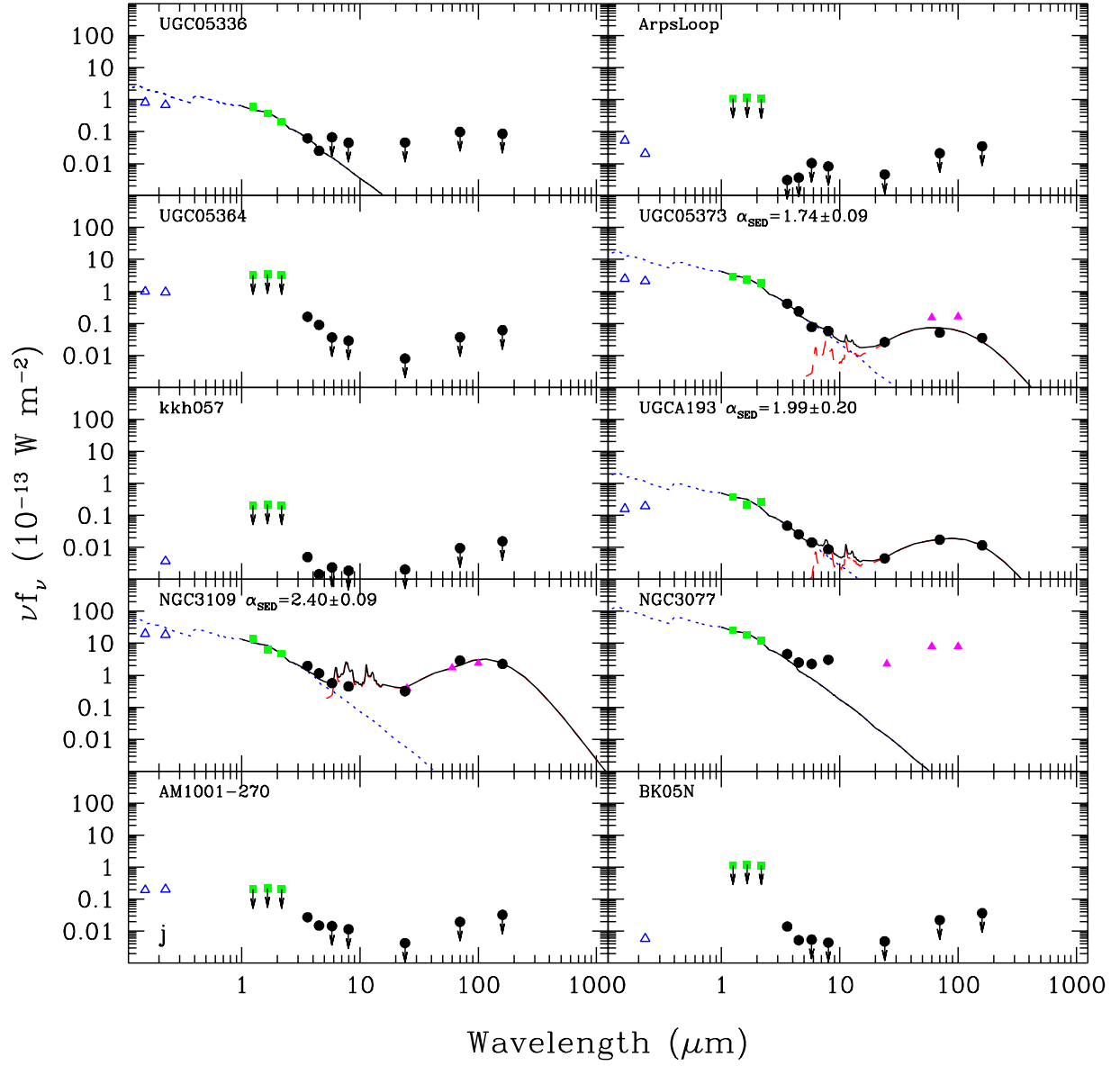


Fig. 16.— Globally-integrated 0.15-160  $\mu\text{m}$  spectral energy distributions for the LVL sample (continued).



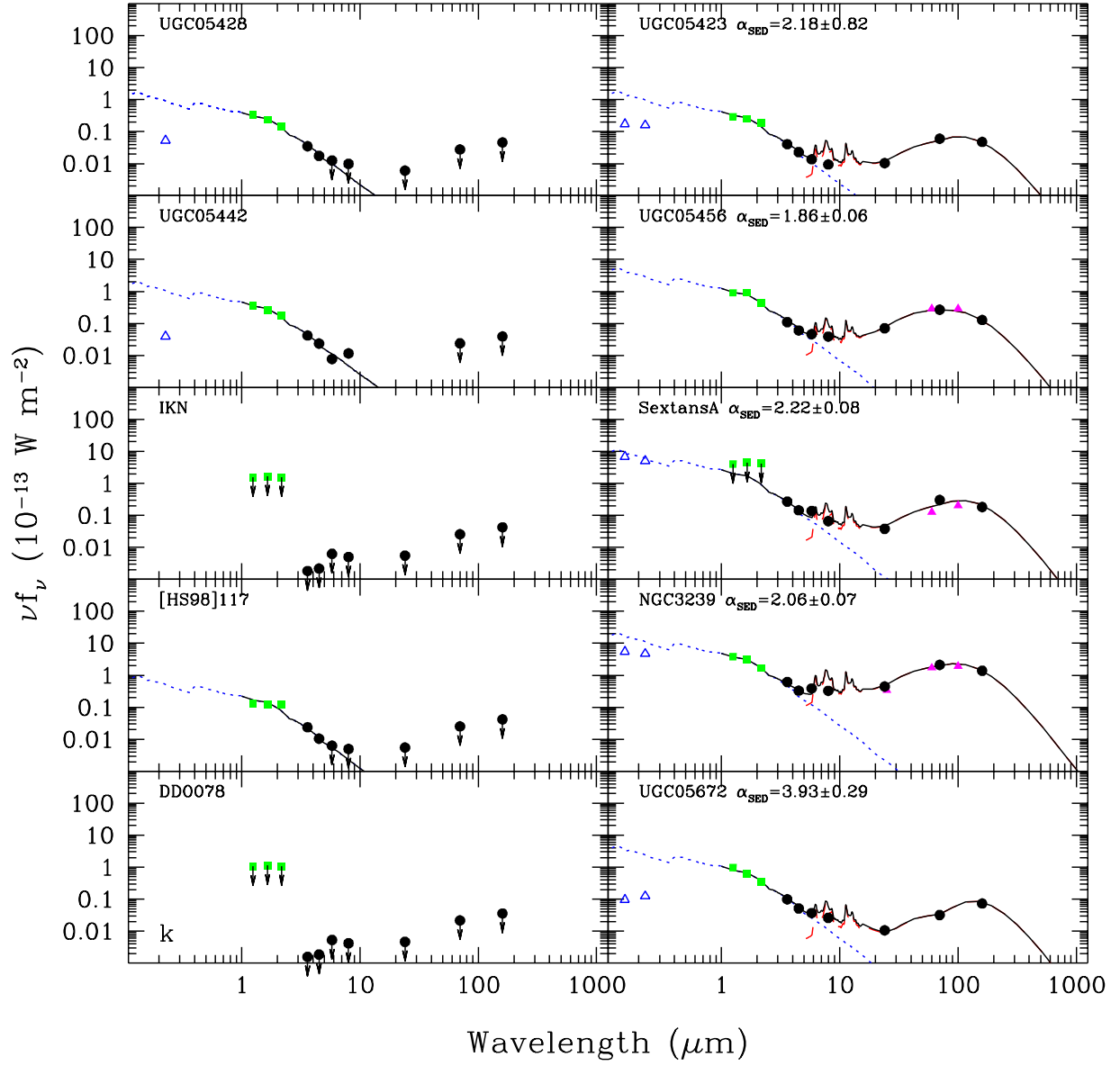


Fig. 17.— Globally-integrated 0.15-160  $\mu\text{m}$  spectral energy distributions for the LVL sample (continued).

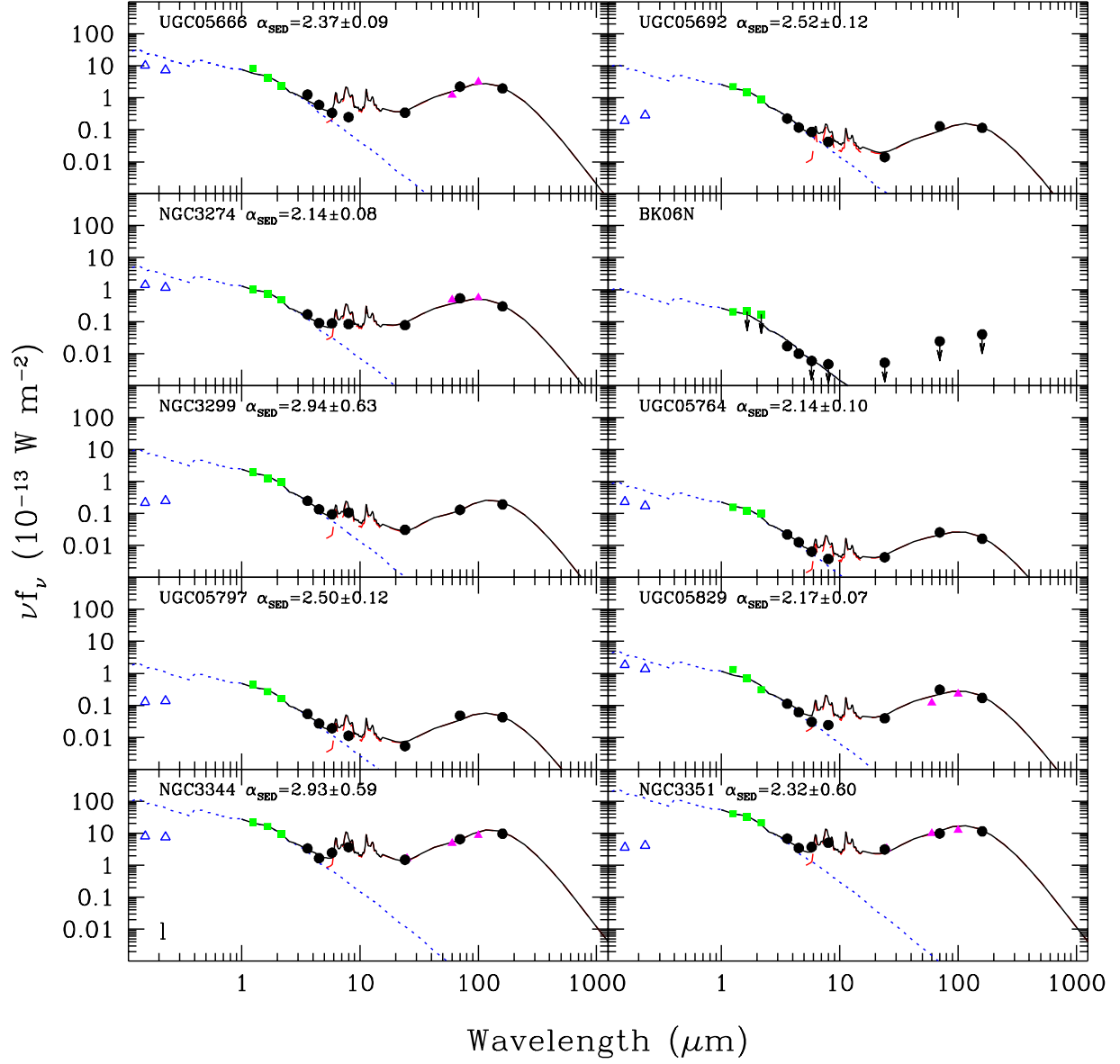


Fig. 18.— Globally-integrated 0.15-160  $\mu\text{m}$  spectral energy distributions for the LVL sample (continued).

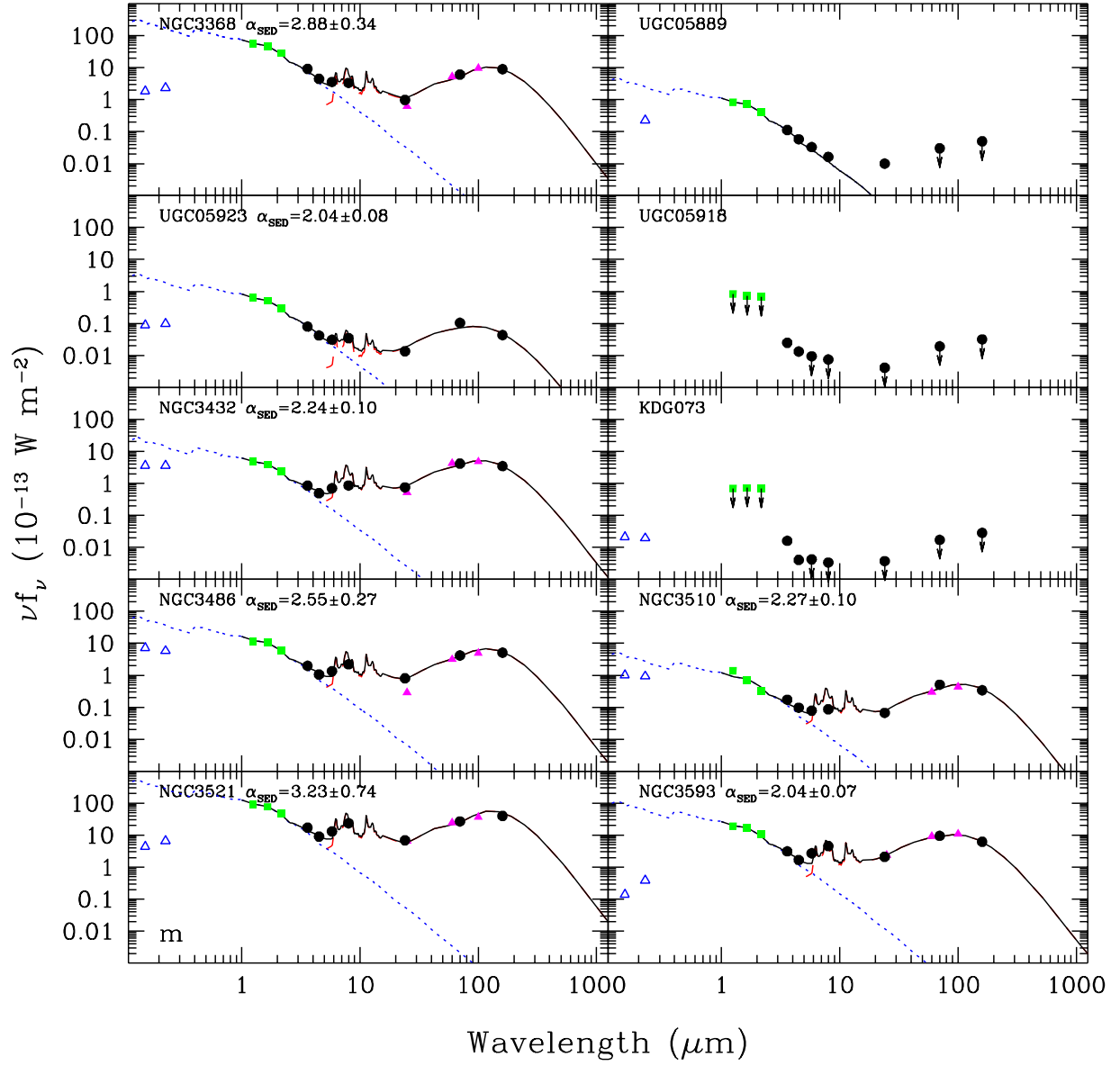


Fig. 19.— Globally-integrated 0.15-160  $\mu\text{m}$  spectral energy distributions for the LVL sample (continued).

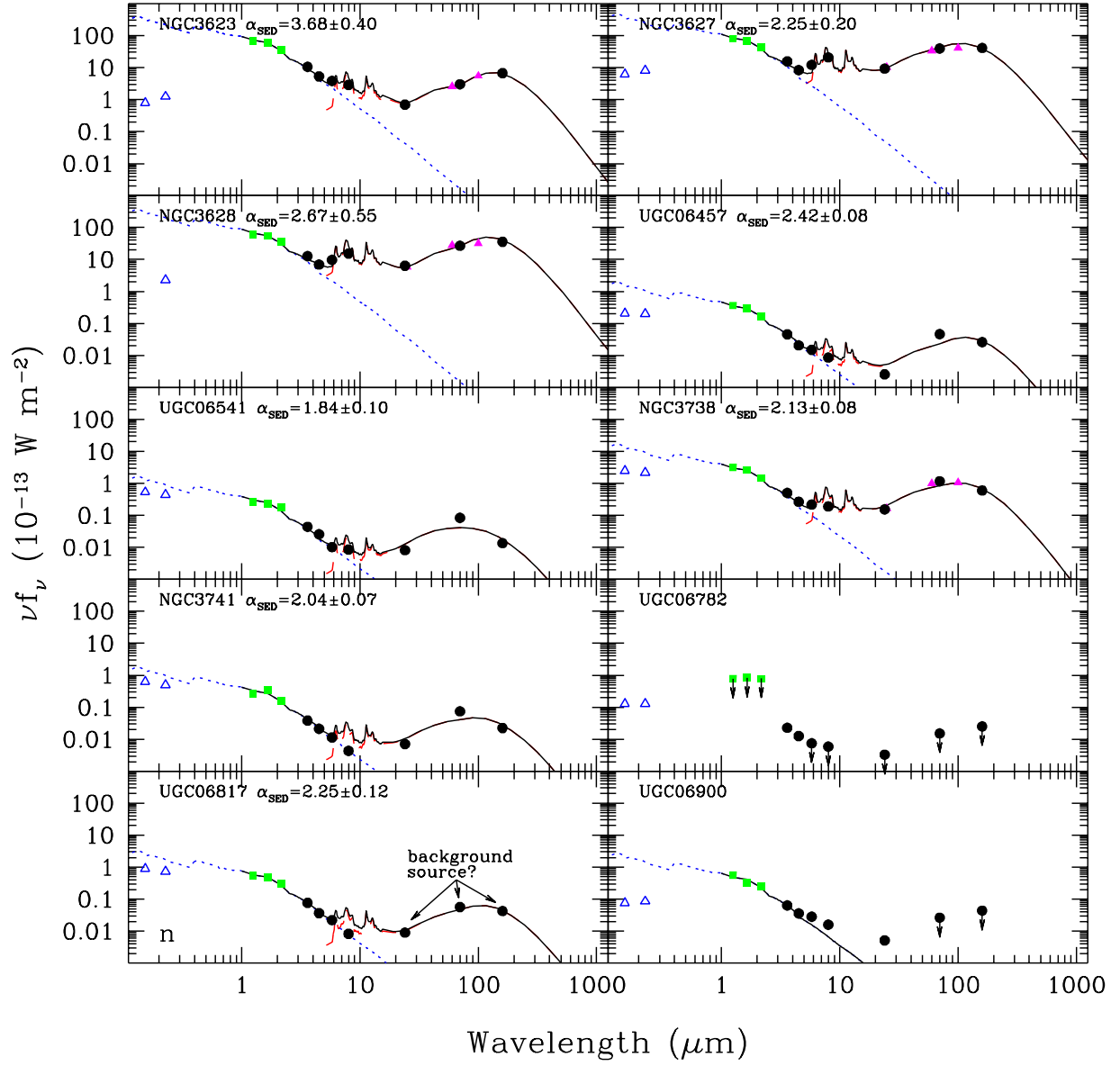


Fig. 20.— Globally-integrated 0.15-160  $\mu\text{m}$  spectral energy distributions for the LVL sample (continued).

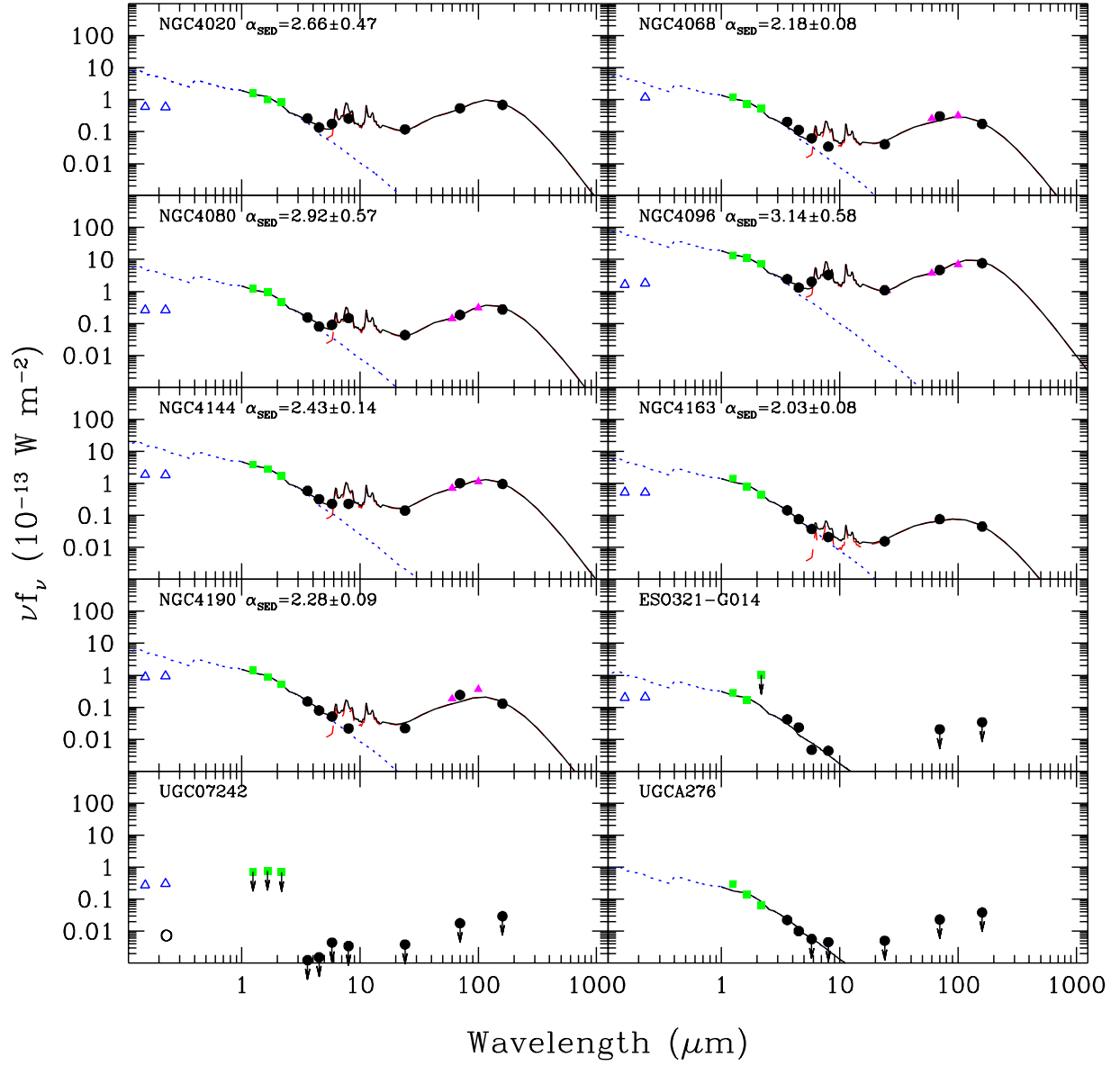


Fig. 21.— Globally-integrated 0.15-160  $\mu\text{m}$  spectral energy distributions for the LVL sample (continued).

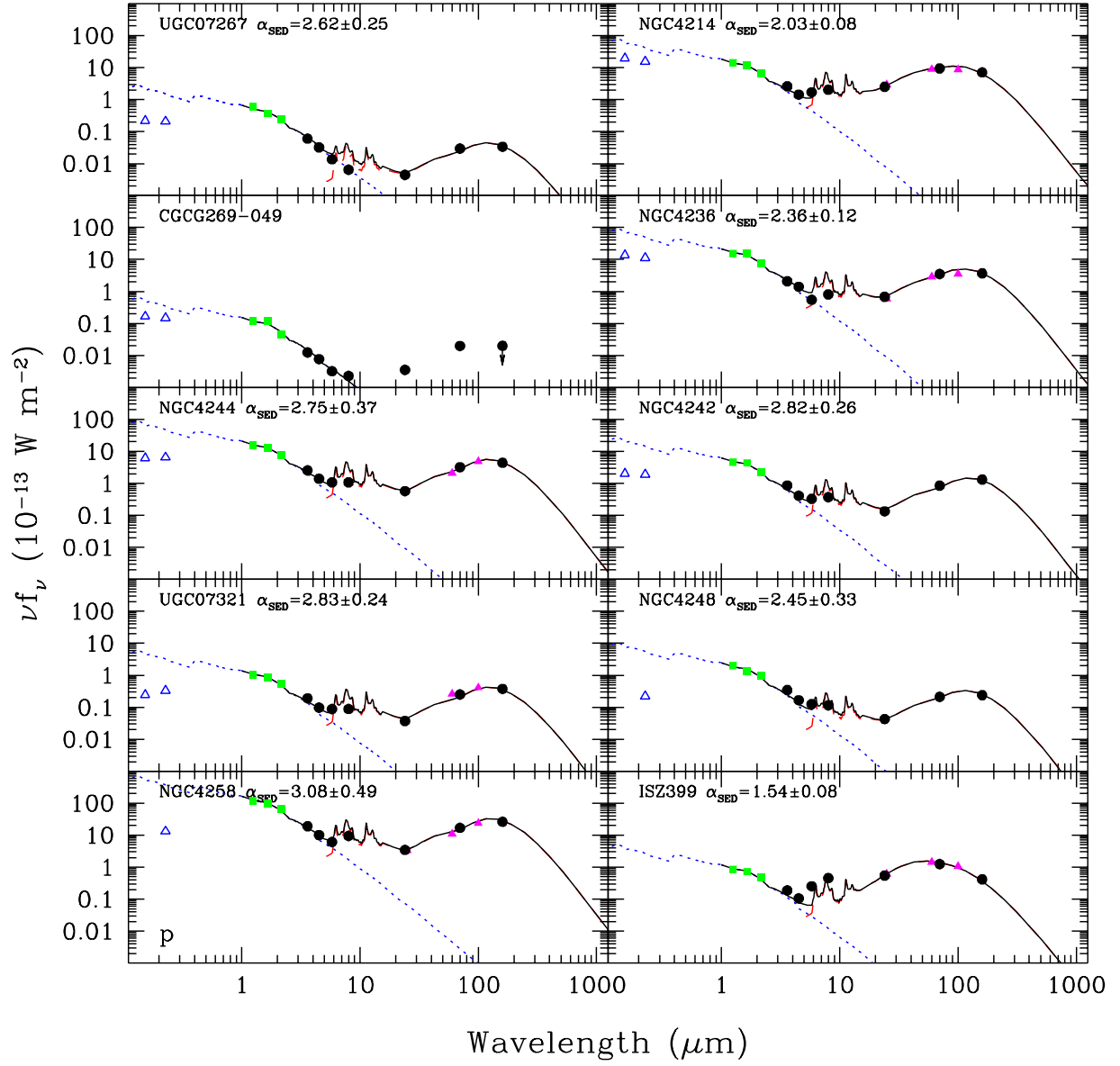


Fig. 22.— Globally-integrated 0.15-160  $\mu\text{m}$  spectral energy distributions for the LVL sample (continued).

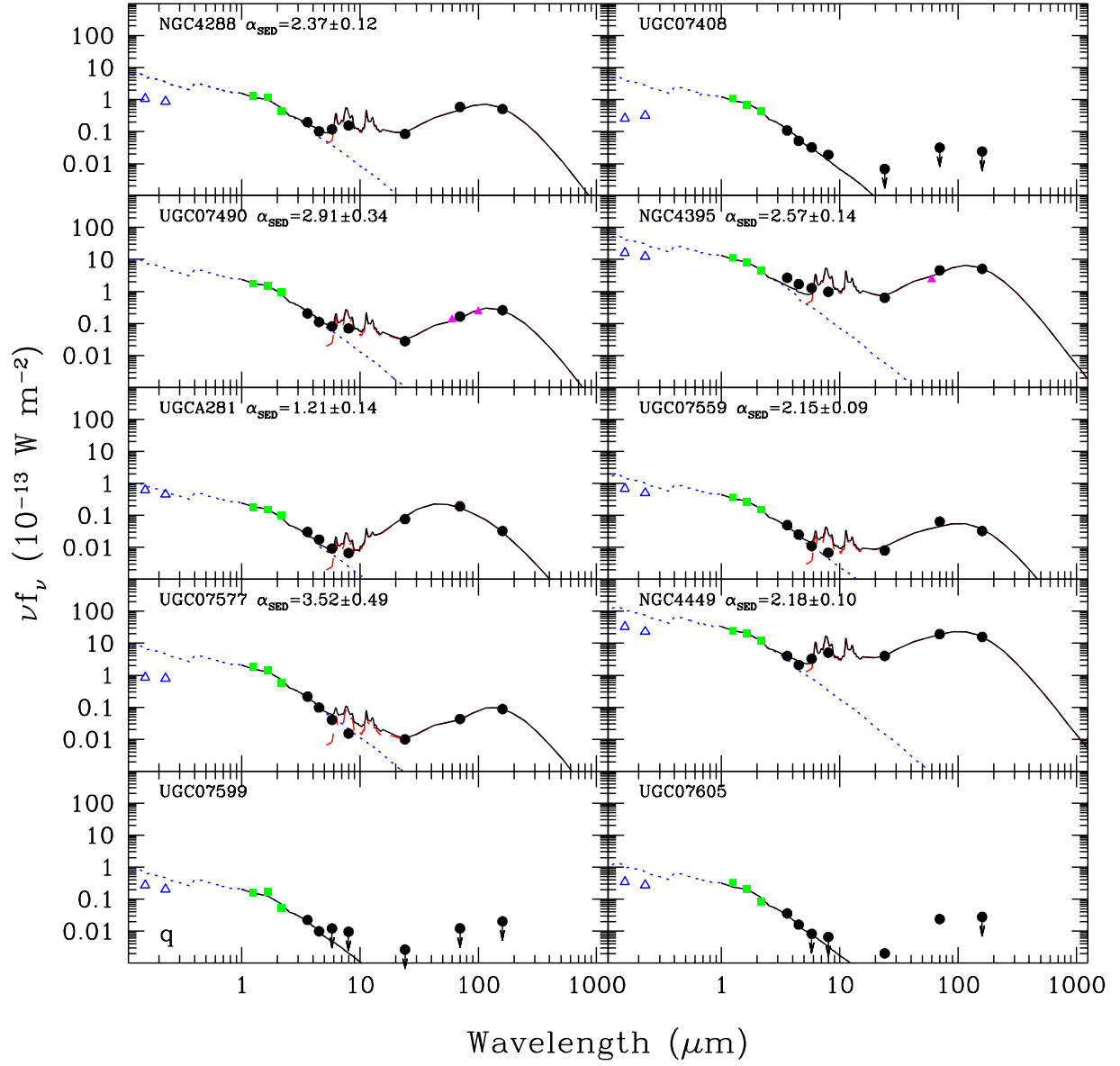


Fig. 23.— Globally-integrated 0.15-160  $\mu\text{m}$  spectral energy distributions for the LVL sample (continued).

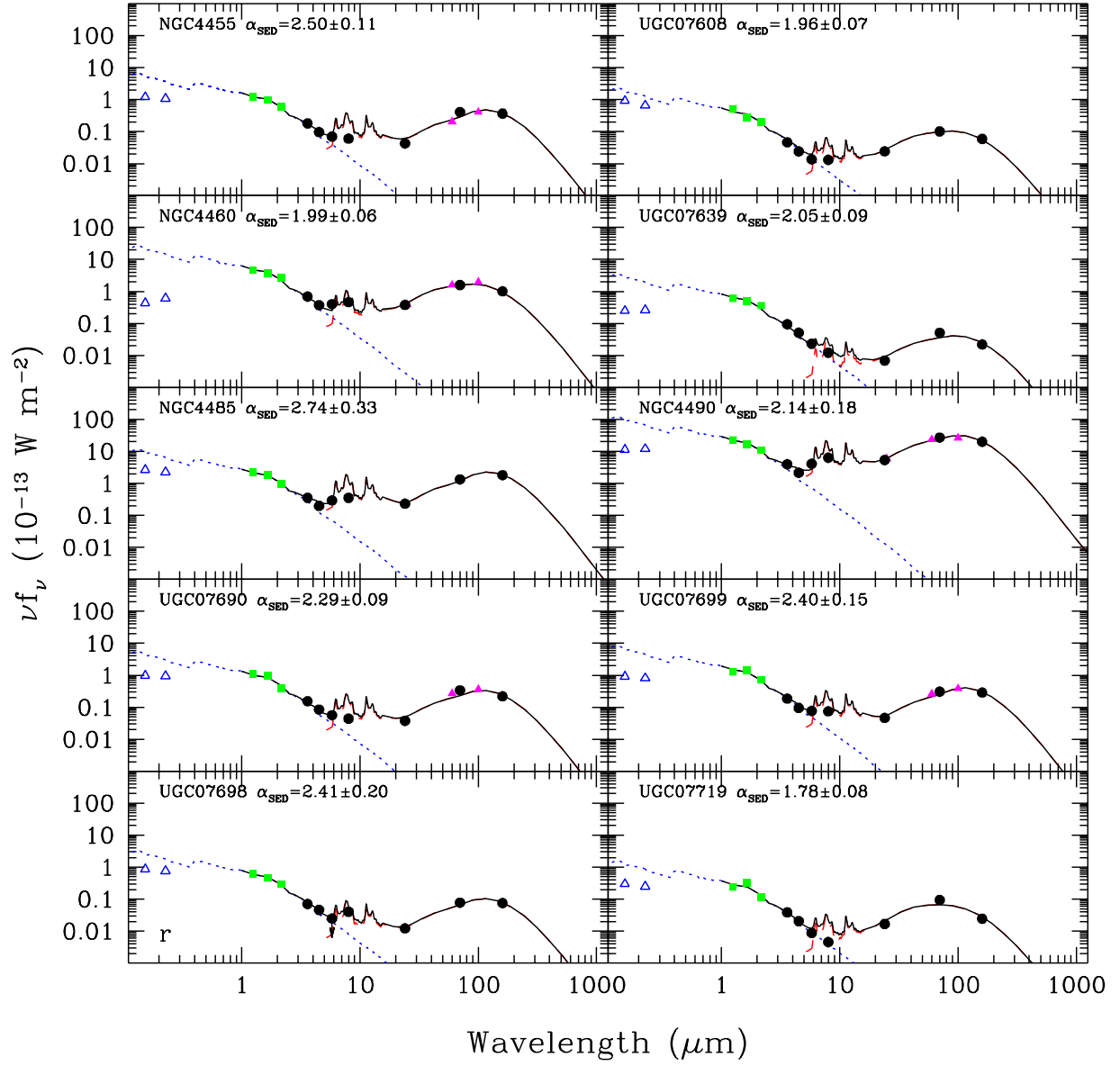


Fig. 24.— Globally-integrated 0.15-160  $\mu\text{m}$  spectral energy distributions for the LVL sample (continued).



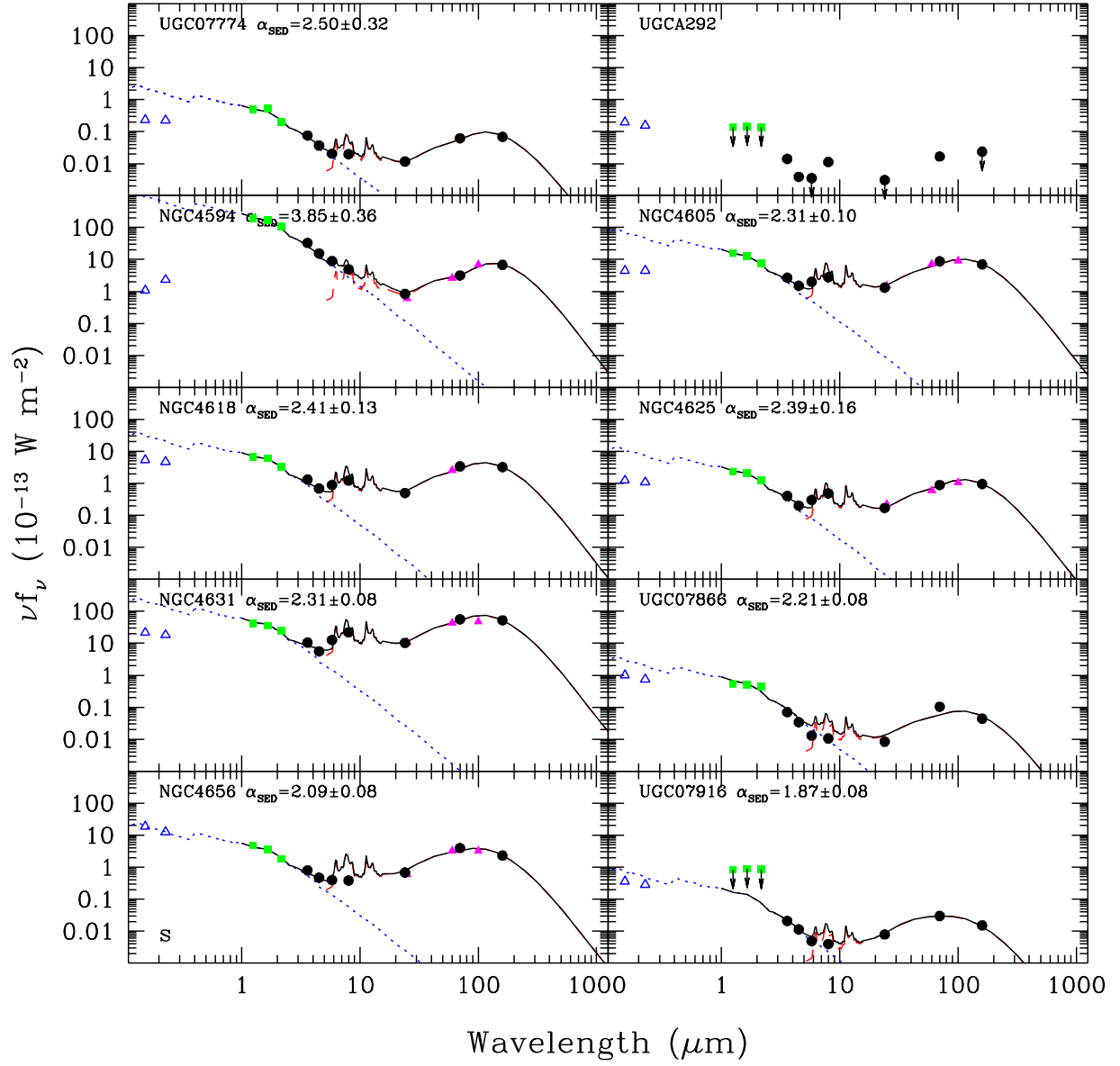


Fig. 25.— Globally-integrated 0.15-160  $\mu\text{m}$  spectral energy distributions for the LVL sample (continued).

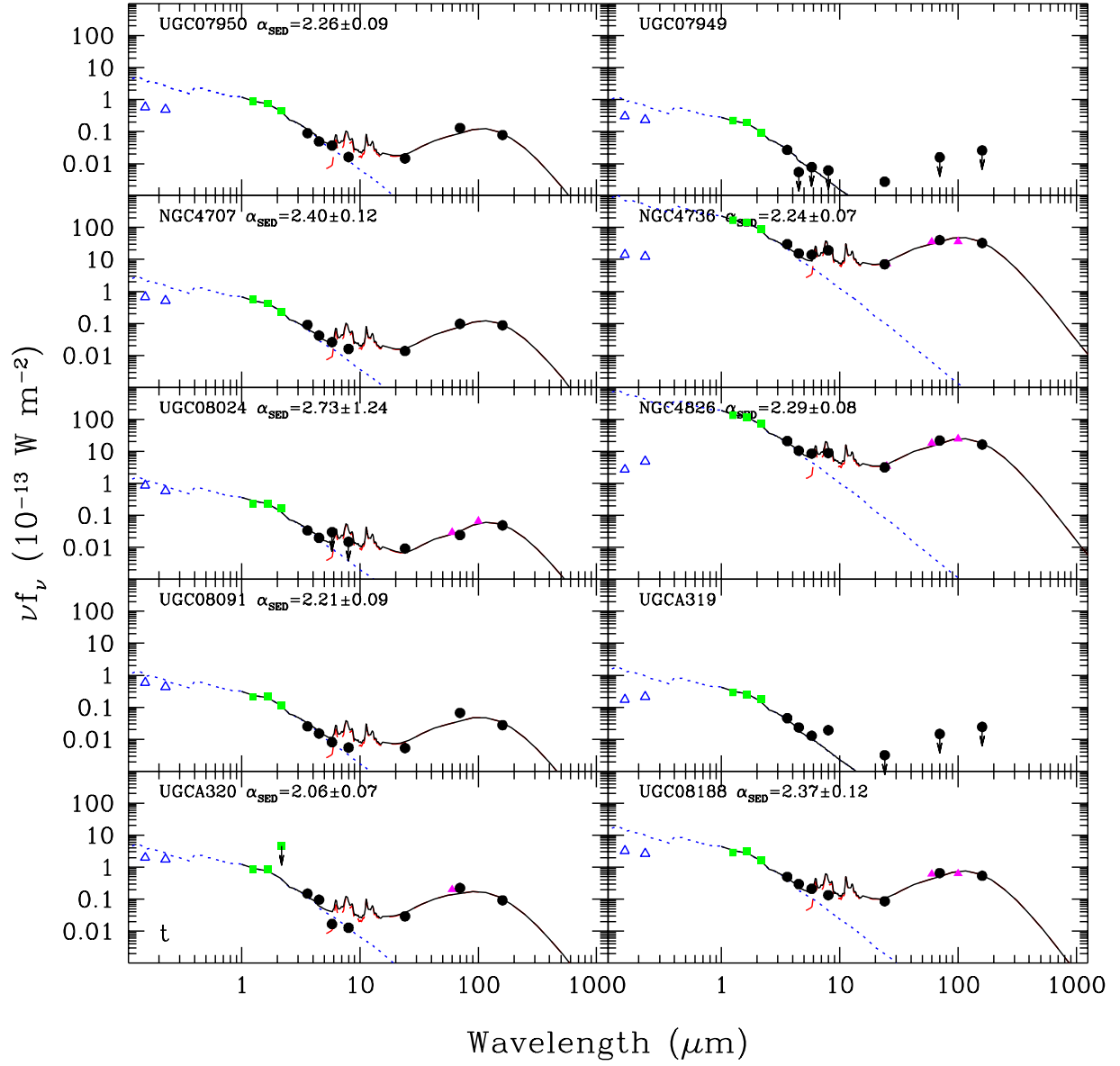


Fig. 26.— Globally-integrated 0.15-160  $\mu\text{m}$  spectral energy distributions for the LVL sample (continued).

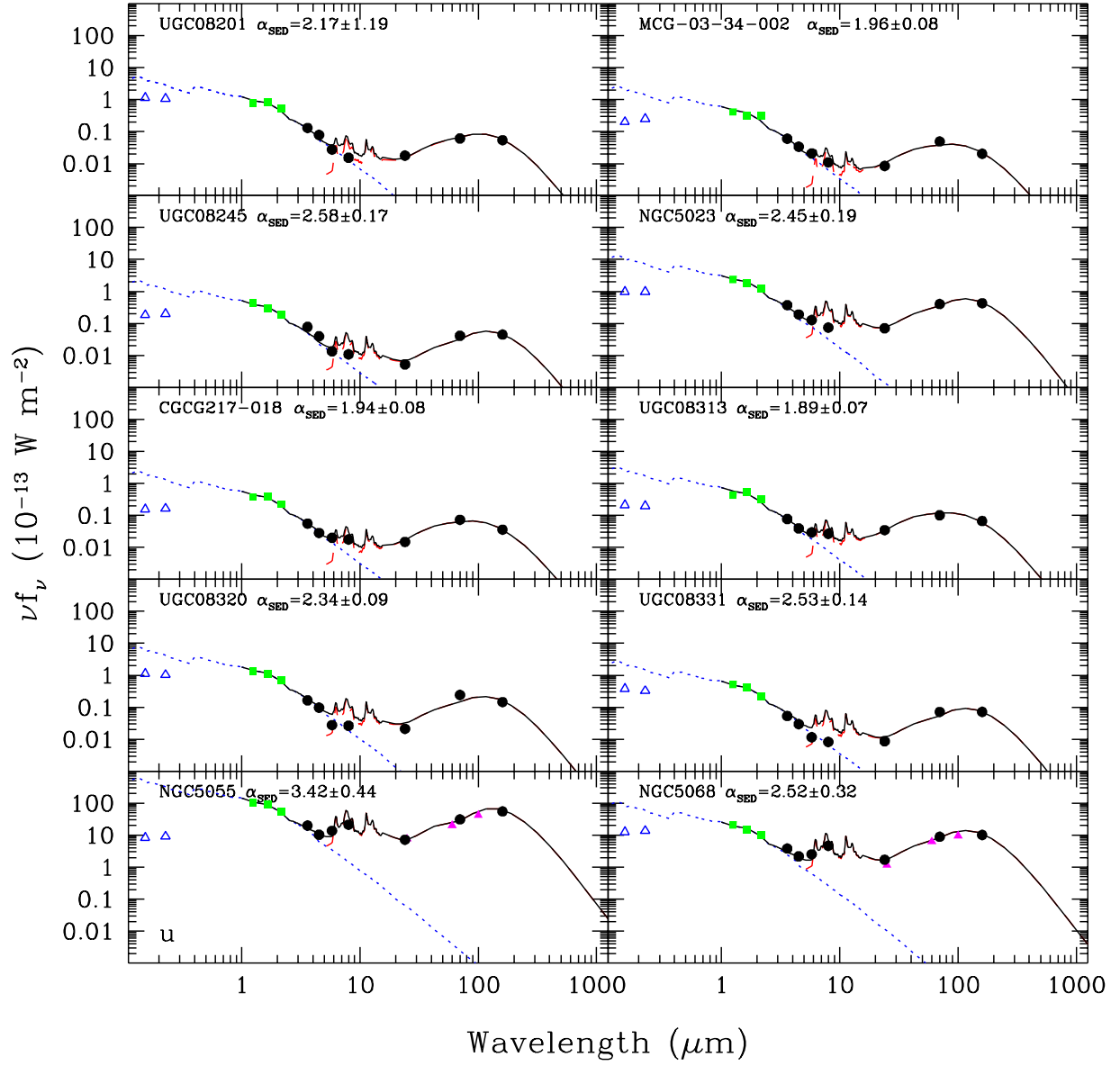


Fig. 27.— Globally-integrated 0.15-160  $\mu\text{m}$  spectral energy distributions for the LVL sample (continued).

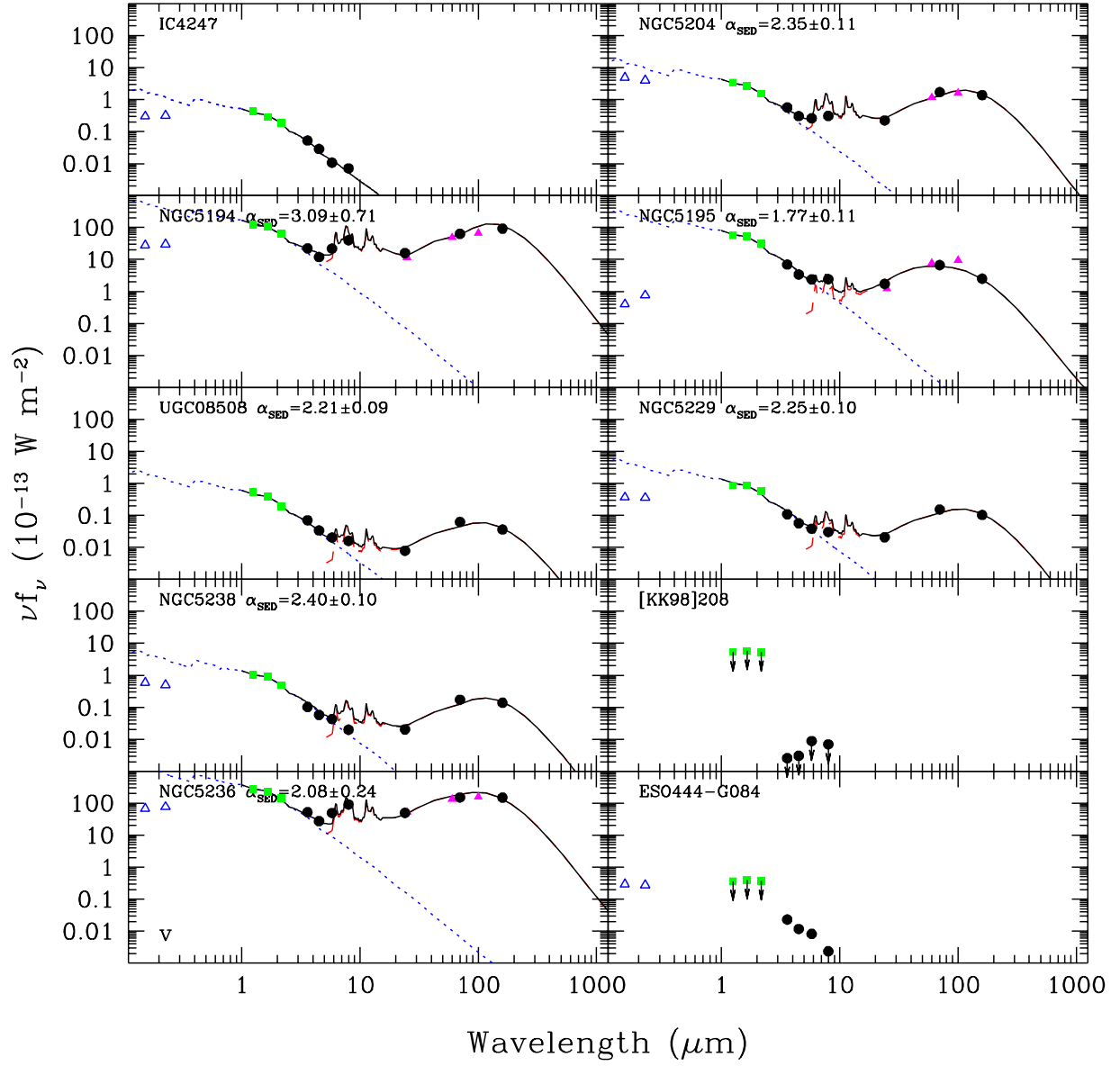


Fig. 28.— Globally-integrated 0.15-160  $\mu\text{m}$  spectral energy distributions for the LVL sample (continued).

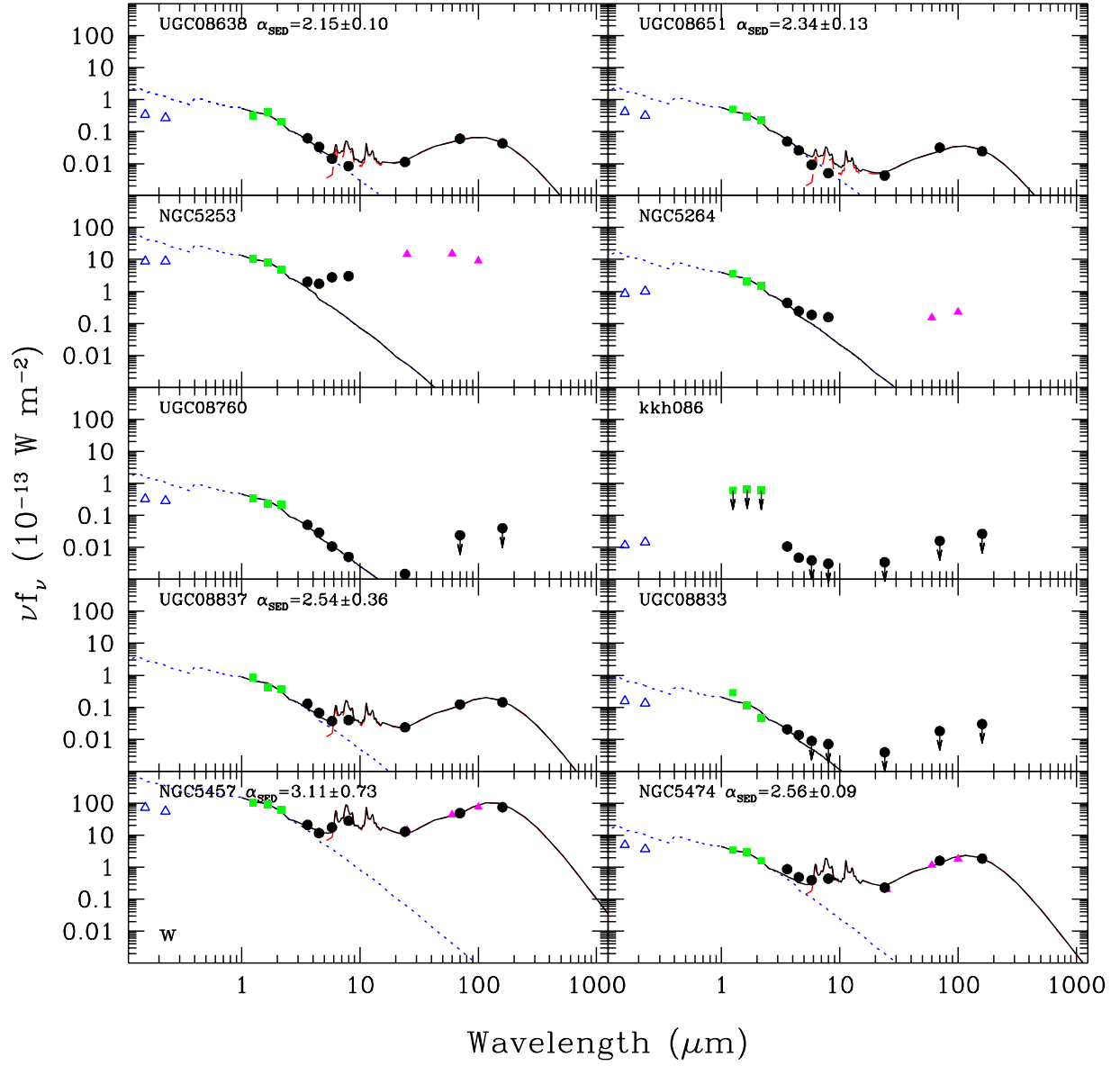


Fig. 29.— Globally-integrated 0.15-160  $\mu\text{m}$  spectral energy distributions for the LVL sample (continued).

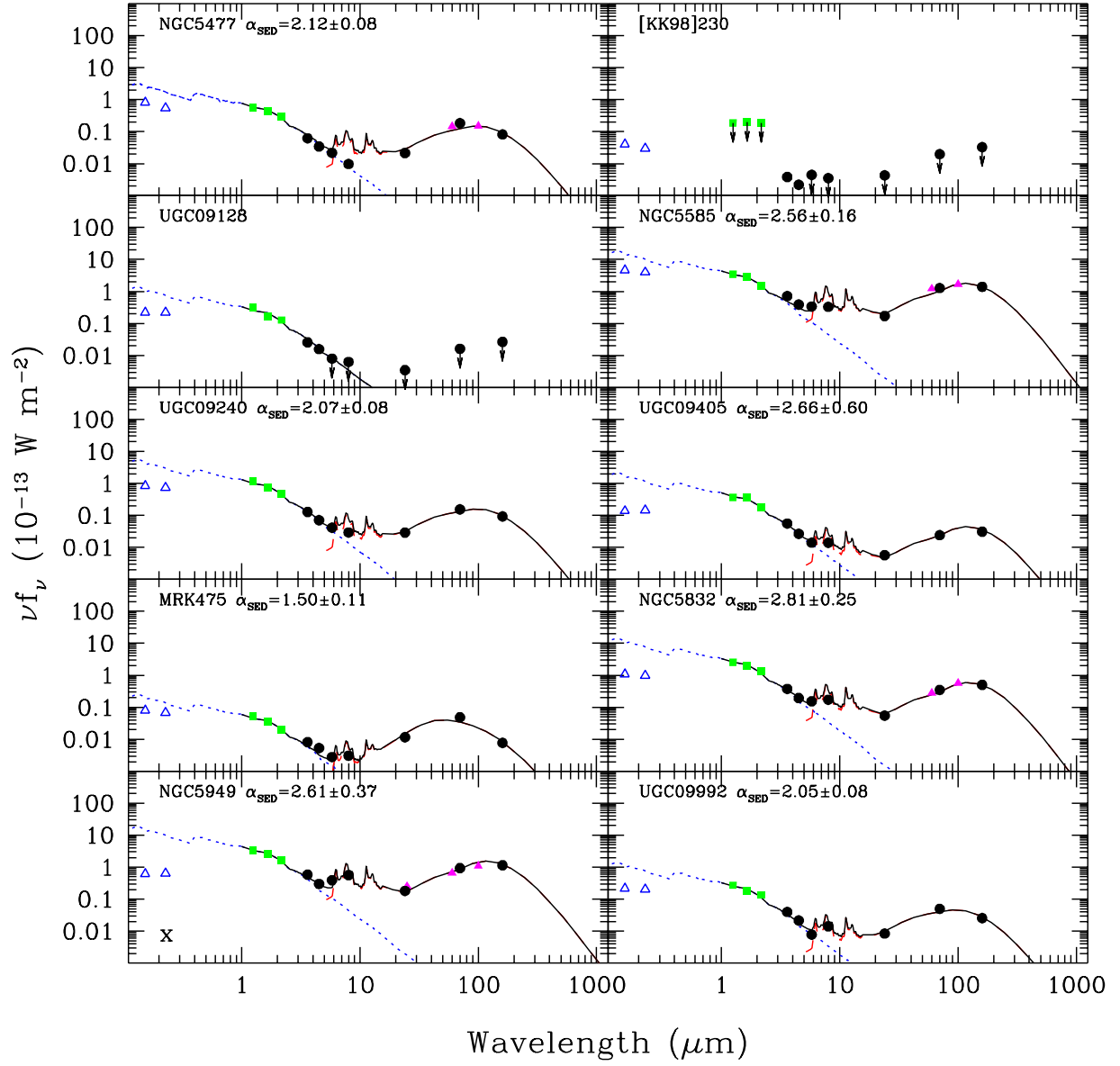


Fig. 30.— Globally-integrated 0.15-160  $\mu\text{m}$  spectral energy distributions for the LVL sample (continued).

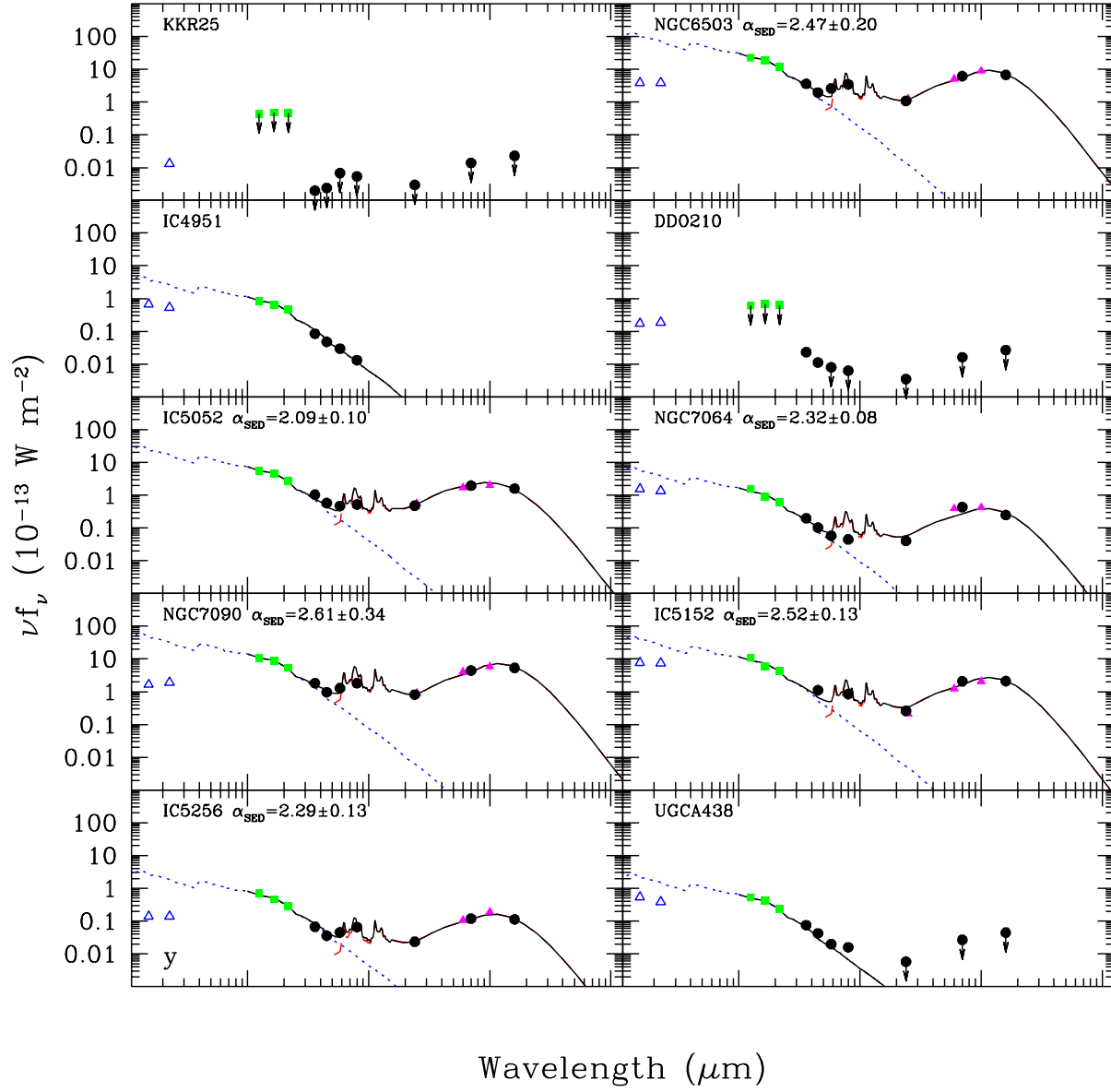


Fig. 31.— Globally-integrated 0.15-160  $\mu\text{m}$  spectral energy distributions for the LVL sample (continued).

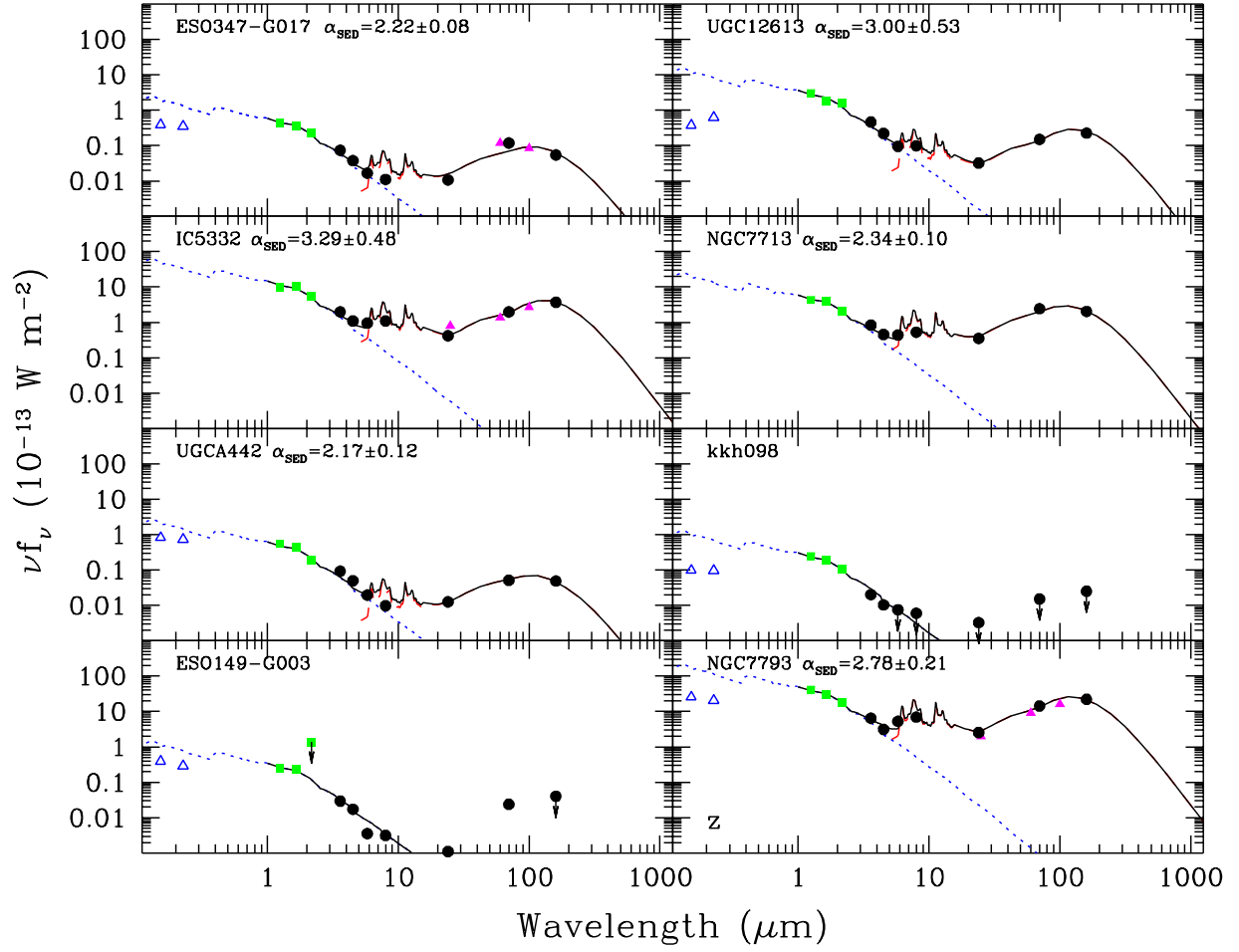


Fig. 32.— Globally-integrated 0.15-160  $\mu\text{m}$  spectral energy distributions for the LVL sample (continued).



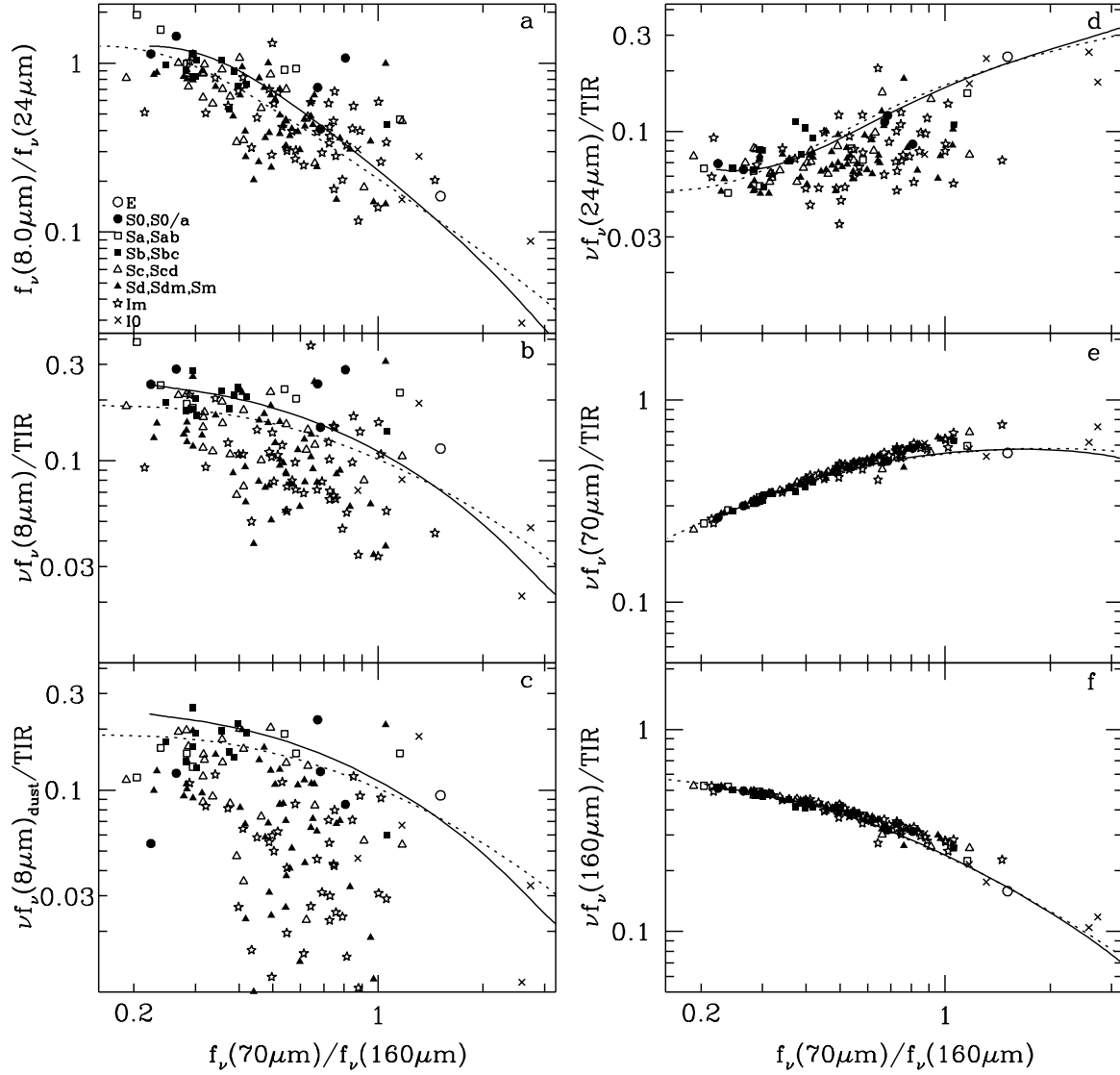


Fig. 33.— Top: The *Spitzer* infrared colors and monochromatic-to-bolometric infrared ratios for globally-integrated LVL data. The solid and dotted lines indicate the SED models of Dale & Helou (2002) and Dale et al. (2001), respectively, derived from the average global trends for a sample of normal star-forming galaxies observed by *ISO* and *IRAS*. The logarithmic ranges spanned by the  $x$ - and  $y$ -axes are the same for all panels, for ease of comparison.

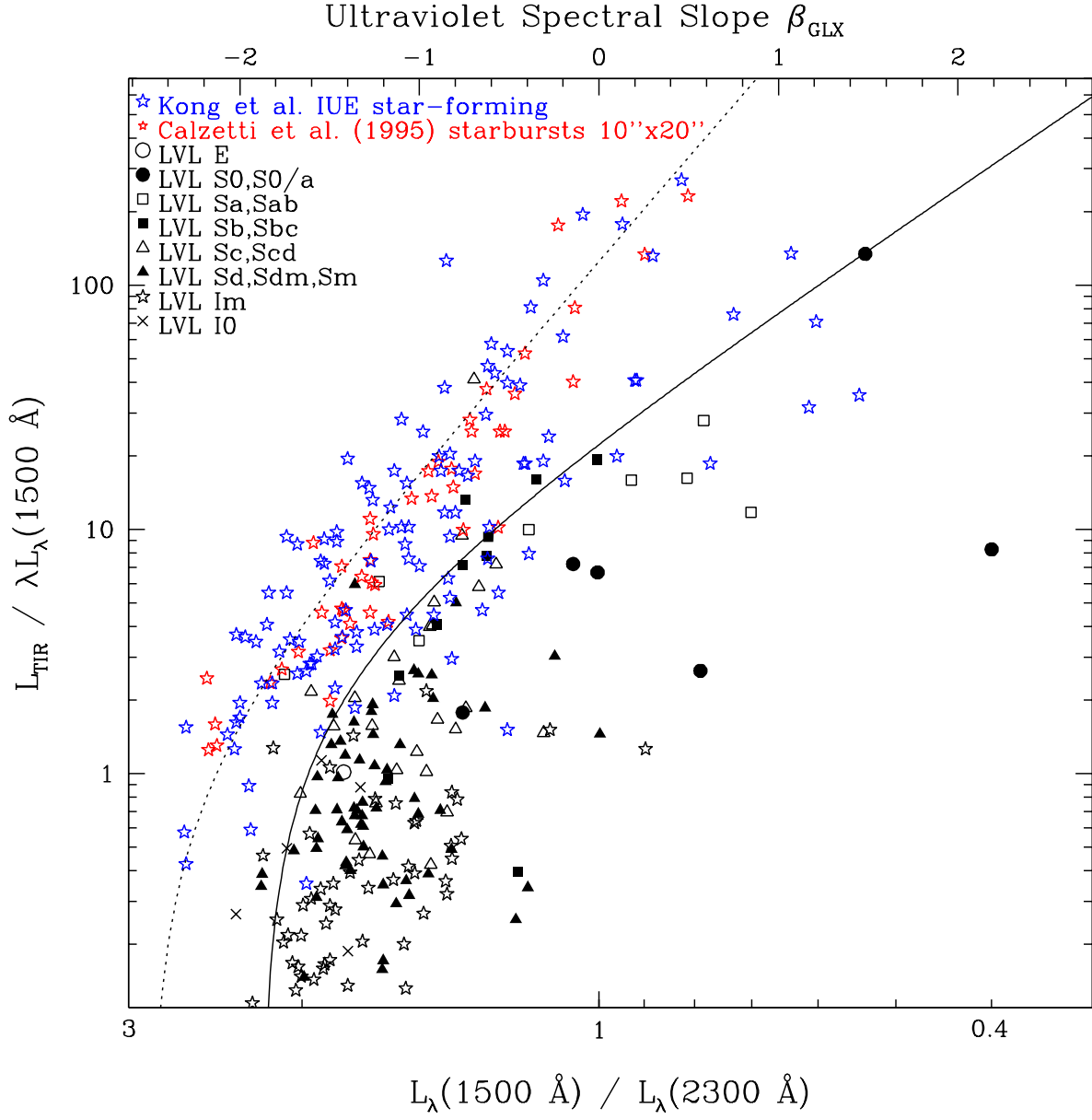


Fig. 34.— The infrared-to-far-ultraviolet ratio as a function of ultraviolet spectral slope. Normal star-forming and starbursting galaxies from Kong et al. (2004) and Calzetti et al. (1995) are plotted in addition to the LVL data points. The dotted curve is that for starbursting galaxies from Kong et al. (2004) and the solid curve is applicable to normal star-forming galaxies (Cortese et al. 2006).

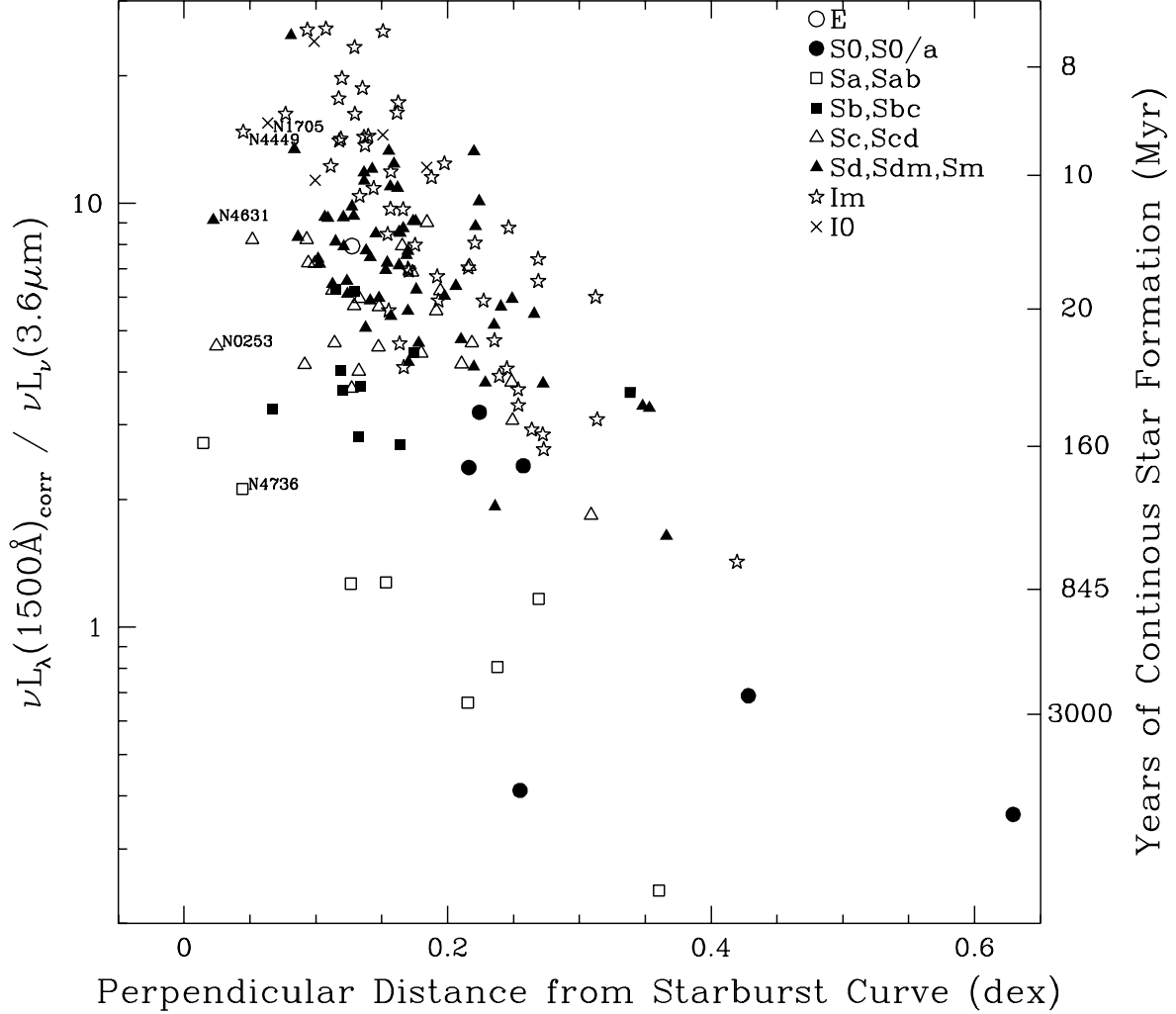


Fig. 35.— The dependence of galaxy star formation history as a function of distance from the starburst relation infrared-to-ultraviolet versus ultraviolet slope, as shown in Figure 34. The left-hand axis is an observable diagnostic of the birthrate parameter, the current star formation rate normalized to the average star formation rate. The righthand axis shows the number of years (continuous) star formation has been occurring, as measured from theoretical spectra. The theoretical spectra utilized are solar metallicity,  $1 M_{\odot} \text{ yr}^{-1}$  continuous star formation curves assuming a double power law initial mass function, with  $\alpha_{1,\text{IMF}} = 1.3$  for  $0.1 < m/M_{\odot} < 0.5$  and  $\alpha_{2,\text{IMF}} = 2.3$  for  $0.5 < m/M_{\odot} < 100$  (Vazquez & Leitherer 2005).

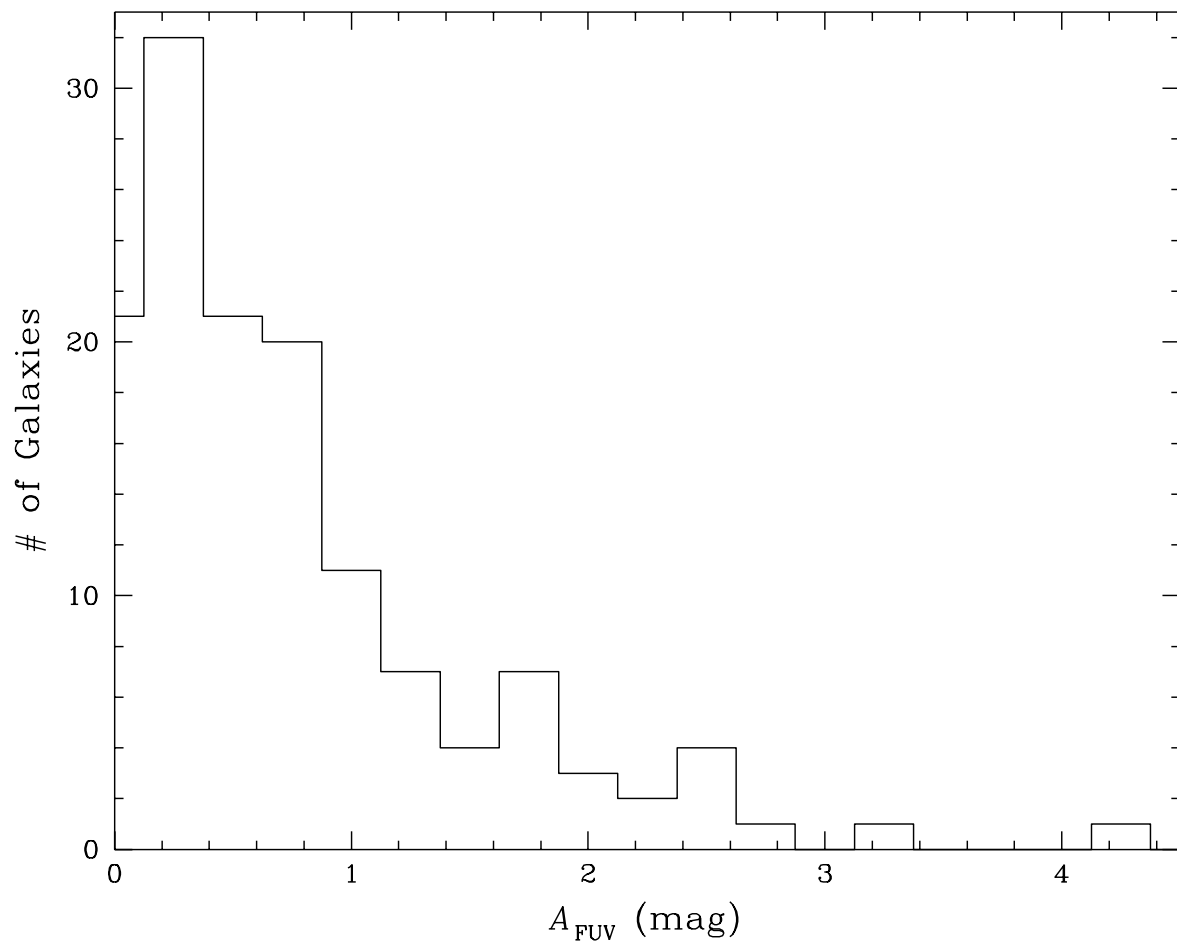


Fig. 36.— The distribution of far-ultraviolet extinctions, computed using the infrared-to-ultraviolet ratio and Equation 2 of Buat et al. (2005).